Department of Physics and Astronomy
University of Heidelberg

Master Thesis in Physics
submitted by

Valentina Salazar Silva

born in Bogotá (Colombia)

2023

The Accordion Lattice: Towards Trapping of Dysprosium Ultracold Gases in Two Dimensions

This Master Thesis has been carried out by Valentina Salazar Silva at the
Physikalisches Institut in Heidelberg
under the supervision of
Jr. Prof. Dr. Lauriane Chomaz

Abstract

Dipolar ultracold quantum gases have recently opened a door for probing new states of matter arising from unexpected stabilization mechanisms. The study of these and further new phenomena at low temperatures and low dimensions is of great interest for the understanding of few- and many-body physics, and for potential implementations in quantum engineering. At the DyLab in Heidelberg, a new experimental setup is being built to probe ultracold Bose gases of dysprosium atoms, the most magnetic element of the periodic table. A crucial part of future experimental applications is the realization of a red-detuned optical dipole trap with tunable periodicity that will allow us to enter the 2D regime, the so-called accordion lattice. We have successfully designed and implemented a first version of an accordion lattice for ^{164}Dy. Initial test results enable a better understanding of the experimental realization of an optical accordion and the instability sources that would eventually cause loss or heating of the dysprosium atoms. Based on the characterization we propose possible solutions and considerations for future implementations.

Kurzfassung

Dipolare ultrakalte Quantengase haben kürzlich eine Tür zur Erforschung neuer Materiezustände geöffnet, die sich aus unerwarteten Stabilisierungsmechanismen ergeben. Die Untersuchung dieser und weiterer neuer Phänomene bei niedrigen Temperaturen und geringen Dimensionen ist von großem Interesse für das Verständnis der Wenig- und Vielteilchenphysik und für mögliche Anwendungen in der Quantentechnik. Am DyLab in Heidelberg wird ein neuer Versuchsaufbau aufgebaut, um ultrakalte Bose-Gase aus Dysprosium, dem magnetischsten Element des Periodensystems, zu untersuchen. Ein entscheidender Teil zukünftiger experimenteller Anwendungen ist die Realisierung einer rotverstimmten optischen Dipolfalle mit abstimmbarer Periodizität, die es uns ermöglichen wird, in das 2D-Regime einzutreten, das sogenannte Akkordeongitter *(accordion lattice)*. Wir haben erfolgreich eine erste Version eines Akkordeongitters für ^{164}Dy entworfen und implementiert. Erste Testergebnisse ermöglichen ein besseres Verständnis der Entstehung eines optischen Akkordeons und der experimentellen Instabilitätsquellen, die schließlich zu einem Verlust oder einer Erwärmung der Dysprosiumatome führen würden. Basierend auf der Charakterisierung schlagen wir mögliche Lösungen und Überlegungen für zukünftige Implementierungen vor.

Aknowledgements

I would like to dedicate the following short paragraphs to all who have been part of this journey. First and foremost, I would like to express my deepest gratitude to Prof. Lauriane Chomaz, who not only offered me a place for a master project in her new group but who supervised my work with uppermost patience and joy. She has made the last year a tremendously fruitful one, full of interesting discussions, learning experiences, and delicious food. Under her supervision, I have rediscovered my passion for physics, and I hope to keep learning from her and the DyLab group, I am certain there are incredible things to come.

To all the group members: I am very glad I had the opportunity to work with you! Special thanks to Jianshun Gao, who has explained to me every little thing I did not know, and who (almost) never laughed at my silly mistakes. I am now an expert on fiber coupling, and I couldn't have done it without you. Thank you for all your support, for the interesting talks, for correcting my Chinese homework, and for being an overall great friend. To Shuwei and Karthik, thank you for helping me solve every problem we encountered and teaching me so much about the lab. It is safe to say this work wouldn't have been possible without you.

Ahora me faltaría, únicamente, agradecer a mi familia y amigos por su apoyo incondicional. A mis papás, gracias por no dudar de mí, por darme fuerzas cuando más me han faltado y por siempre haber tomado las mejores decisiones para que yo pueda darme el lujo de estar aquí, haciendo lo que más me gusta. A mis abuelos, gracias por la familia que nos han regalado, por el amor y la educación. Gracias por el amor a las ciencias, a la filosofía y a la vida. A cada paso que doy los guardo en el corazón. Finalmente, a mi esposa Alexandra Leguizamón. Gracias por ser mi compañera de vida, por motivarme todos los días y por cuidarme. Gracias por no solo tolerar las largas horas, sino por recibirme con tanto amor cada vez que llegue cansada y preocupada. Gracias por tu apoyo y cariño en cada proyecto, nada de esto hubiera resultado sin ti.

Contents

Chapter 1

Introduction

Physics has been, thorough history, a source of many answers but many more questions. At the end of the 19th century and the beginning of the 20th century, the classic model of the atom had emerged and established itself, where according to the Newtonian theory negative electrons could orbit the nucleus at any distance. However, predictions based on this and other models, such as a continuous spectrum of heated hydrogen atoms, to name a simple case, caused the emergence of many mysteries and contradictions, which preceded a theory of quantum mechanics that could explain the inconsistencies. Quantum physics is, in broad terms, an attempt to construct abstract and simplified- but not too simplified- models to describe the complex nature of the atomic and subatomic universe. In the 1920s, Albert Einstein, following Bose's first ideas, further developed the quantum theory that describes a mono-atomic gas with indistinguishable particles occupying the same energetic state. He could only conclude this conjunction to be a paradox and "as good as impossible". Only 70 years later, in July 1995, atom cooling and trapping technologies allowed scientists to reproduce the theorized macroscopic quantum state of bosonic particles. Ever since, Bose-Einstein Condensates (BECs) have increasingly proven to be an irreplaceable tool to exhibit unexpected and revolutionary physics. In contrast to Einsteins prediction, the production of BECs is not only possible, but has become standard practice, and every day more customized and specialized set-ups are brought to life.

At the Quantum Fluids group in Heidelberg, we are taking advantage of the experimental knowledge gained on BECs during the last 27 years, to dive into the emerging field of new orders of quantum gases. BECs realized with bosonic isotopes of highly magnetic elements, have opened the door to precisely tunable atomic interactions and, together with highly controlled trapping geometries,

have enabled the observation of self-bound quantum fluids, droplet crystals, and self-bound, globally coherent assemblies of quantum droplets, also known as superfluid solids.

A novel combination of 2-dimensional and 3-dimensional magneto-optical traps (3D and 2D MOT) for dysprosium atoms, complemented with optical trapping and 2-dimensional dynamical optical trapping techniques, the so-called Accordion Lattice, will allow us to probe new physical phenomena arising in low-temperature and low-dimensional quantum gases. Taking advantage of dysprosium's high magnetic moment, we can probe, with high-precision, the competing dipolar and contact interactions, and the stabilization through quantum fluctuations.

In order to prepare a reliable system to enter the low-dimension regime, it is necessary to find adequate engineering solutions for loading and trapping dysprosium atoms. Inspired by the achievements of various laboratories to create dynamical optical traps for different atomic species, we design and implement a customized Accordion Lattice for dysprosium. The aim of this work is to introduce the fundamental physical concepts, expectations and constraints taken into account for the final design, as well as to present the first realization of the system and its performance.

Outline

Chapter 2 The first chapter of this thesis will introduce the research area of ultracold quantum gases and the special effects of dipolar Bose quantum gases that have led to the discovery of new states of matter. As our experiment will center on bosonic isotopes of dysprosium, a brief introduction to the relevant properties of this highly magnetic element will be discussed. Finally, the present status of the general experimental setup will be introduced, emphasizing the mechanical constraints that determine the final design of an accordion lattice for ^{164}Dy.

Chapter 3 The second part of this work centers around the theoretical considerations that influence the main optical characteristics of an accordion lattice. A general overview of the most important concepts for realizing a red-detuned tunable optical dipole trap is given. In the end, the interference pattern calcu-

lations on which the accordion lattice design is based are summarized and the required trap geometry to enter the 2-dimensional regime is established.

Chapter 4 The fourth chapter will focus on the optical design necessary to achieve the expectations set in chapter 3. A thorough description of the optical elements and their quality as possible sources of instabilities of the optical accordion will be given. Ultimately, the opto-mechanical design for the individual optical components will be detailed.

Chapter 5 The last chapter will be based on the full characterization of the first application of the accordion setup with a low-power laser. Instabilities of the pattern itself and possible solutions will be presented. Special attention will be paid to the alignment of the optical setup and the range of trapping frequencies that can be achieved considering the mechanical limitations.

Accessibility The following document has been developed taking into account the potential accessibility for readers with color and general visual deficiencies. Accordingly, a custom high-contrast palette that considers trichromacy, anomalous trichromacy, dichromacy, and monochromacy has been used for most images. Furthermore, all figures count with a detailed caption that emphasizes the relevant data results.

Chapter 2

Motivation

2.1 Ultracold Quantum Gases

Ultracold quantum gases of bosonic and fermionic atomic species are robust and adaptable testing tools to explore new quantum phenomena. The implementation of artificial periodic potentials of light and highly controllable trapping geometries has enabled a significant development of quantum engineering possibilities [1]. To understand the importance of ultracold quantum gases as a platform to study so far unexplored phenomena, it is necessary to start with a basic definition and the advantages it represents as a research tool.

An ultracold quantum gas is an ensemble of atoms held at temperatures near absolute zero. Such systems enable the creation of exotic phenomena such as Bose-Einstein condensation (BEC), bosonic superfluidity, Efimov states, Bardeen-Cooper-Schrieffer (BCS) superfluidity and the BEC-BCS crossover, to name a few [2]. Overall, an ultracold quantum gas is a system made of indistinguishable particles, which brought to low temperatures or high densities, exhibits **macroscopic quantum behavior**. These systems can be described by either Bose-Einstein statistics or Fermi-Dirac statistics, depending on the spin of the particle or the wave function under particle exchange. The preparation of ultracold quantum gases as examples of strongly interacting matter, allows us to probe theoretical models in highly controllable environments. The characteristics of an ultracold quantum gas, such as shape, density, and excitation processes, are determined fundamentally by the interparticle interactions. In the case of atoms at temperatures below the order of microkelvin, the wavelength associated with each atom is large in comparison to the usual size of a

diatomic molecule, following the relation

$$\lambda_{dB} = \sqrt{\frac{2\pi\hbar^2}{mk_BT}} \quad , \tag{2.1}$$

where λ_{dB} is the De Broglie wavelength, m the atomic mass, T the temperature of the system, and k_B the Boltzmann constant. Furthermore, the delocalization of cold atoms due to Heisenberg inequality leads to a "smoothing" of the interaction potential and long-range interactions will be granted a central role. The following section serves as an introduction to the models describing the interactions relevant to the scope of this thesis. In the case of our experiment, the different isotopes of dysprosium can fall under the bosonic or fermionic category. However, in the scope of this work only the isotope ^{164}Dy, a bosonic variant, will be taken into consideration.

2.1.1 Bose-Einstein Condensates

Bose-Einstein Condensation is a phenomenon in which bosonic statistics allow an infinite part of bosons to occupy the ground state level of the system. The states of a Bose gas are not subject to any occupation restriction, and in theory, at a temperature $T = 0$ all particles could populate the lowest energy level. However, the populating process of the ground state has been observed at higher temperatures.

First, we introduce the quantitative description of an ideal Bose gas in an external potential based on the review by Fetter and Foot [3], to dive into the requirements for Bose-Einstein condensation. Assume an ideal Bose gas in equilibrium at temperature T and chemical potential μ in an external potential. The mean occupation number of a state j is given by

$$n_j = \frac{1}{\exp\left[\beta(\epsilon_j - \mu)\right] - 1} \equiv f(\epsilon_j) \tag{2.2}$$

where $\beta = k_BT^{-1}$ and $f(\epsilon)$ is the Bose-Einstein distribution function. The density of states defined as $g(\epsilon) = \sum_j \delta(\epsilon - \epsilon_j)$ is given by the sum over all distinct

single-particle states. The mean total particle number can then be written as

$$N(T,\mu) = \int d\epsilon g(\epsilon) f(\epsilon). \tag{2.3}$$

In the classical limit for a fixed number N, the chemical potential is large and negative. However, for lower temperatures, μ increases and approaches the lowest, single-particle energy ϵ_0 at the so called critical temperature. Below the critical temperature, the number of particles in the excited states saturates and reaches

$$N'(T) = \int_{(\epsilon_0)}^{\infty} d\epsilon \frac{g(\epsilon)}{\exp\left[\beta(\epsilon - \epsilon_0\right] - 1}, \tag{2.4}$$

which is finite for a vanishing density of states at ϵ_0. In this case, a macroscopic number of particles populate the lowest state with occupation number N_0 and $N = N_0(T) + N'(T)$. The occupation of the lowest state follows a temperature dependence to conserve the total particle number N. The critical temperature T_c at which Bose-Einstein Condensation can be observed for a 3-dimensional system, depends on the mass of the atomic species, the density and the volume as

$$T_c = 3.31 \frac{\hbar^2}{k_{Bm}} \left(\frac{N}{V}\right)^{2/3}. \tag{2.5}$$

In general, Bose-Einstein condensates exhibit unusual properties; due to coherence, microscopic quantum mechanical phenomena such as wave function interference, become apparent microscopically, allowing for better observation and control than in other cases, e.g electrons. A BEC can then be described by a unique wave function $\Psi(\mathbf{r})$. In some simple cases (ultracold temperatures), the well-known Gross-Pitaevskii equation (GPE), a non-linear Schrödinger equation, accurately describes the state of the particles.

$$i\hbar\partial_t\psi = \left[\frac{\hbar^2\nabla^2}{2m} + U_{\text{ext}}(\mathbf{r}) + \int dr V(|\mathbf{r} - \mathbf{r}'|)|\psi(\mathbf{r}')|^2\right]\psi. \tag{2.6}$$

where m is the mass of the bosons, $U_{\text{ext}}(\mathbf{r})$ an external potential, and $V(|\mathbf{r} - \mathbf{r}'|)$ represents the inter-particle interactions. The **contact interaction** and the **dipolar interaction** dominating the behavior of the bosons in our experiment will be

detailed in the following sections.

2.1.2 Contact Interactions

Atomic interactions in a weakly interacting quantum gas can be described by the short-range **van-der-Waals (vdW)** potential U_{vdW} that arises from induced electric dipoles

$$V_{\mathrm{vdW}} = -\frac{C_6}{r^6} \quad , \tag{2.7}$$

where r is the interatomic distance and C_6 is the van-der Waals coefficient. The coefficient C_6 is positive in most cases, meaning that the vdW interaction is attractive and predominant for long distances, i.e distances where the atoms don't overlap with each other. At short distances the repulsion between the atoms becomes dominant. The finite range of the vdW interaction is given by the vdW-radius r_{vdW}. In the case of two interacting dysprosium atoms $C_6 = 2275$a.u, where the atomic unit is defined by $9.55 \times 10^{-80}\mathrm{Jm}^6$.

In the ultracold limit, the vdW potential is well approximated by a simple contact pseudo potential

$$V_{\mathrm{cont}}(\mathbf{r}) = \frac{4\pi\hbar^2 a_s}{m}\delta(\mathbf{r}) = g\delta(\mathbf{r}) \quad , \tag{2.8}$$

where m is the mass of the atoms, g is the contact interaction strength, and a_s is the so-called s-wave scattering length, which corresponds to the first term in the partial wave expansion.

2.1.3 Feshbach resonances

The scattering length a_s can be tuned at will making use of the so-called **Feshbach resonances**. A Feshbach resonance occurs when the bound molecular state in the closed channel energetically approaches the scattering state in the open channel [4]. The energy difference can be tuned by a magnetic field when the corresponding magnetic moments are different. A resonance occurs if there is coupling between the channels, e.g hyperfine or anisotropic interactions. The dependence of the s-wave scattering on the external magnetic field can be de-

scribed by the simple expression

$$a_s = a_{\mathrm{Bg}}\Big(1 - \frac{\Delta}{B - B_0}\Big), \tag{2.9}$$

where a_{Bg} is the background scattering length, B_0 is the position of the Feshbach resonance and Δ the corresponding width. The zero crossing of the scattering length occurs at a magnetic field $B = B_0 + \Delta$.

In the case of ^{164}Dy, the value for the background scattering length was measured to be $a_{bg} = 92(8)a_0$ by Tang et al. in 2015 [5]. Here, the Bohr radius a_0 is defined as $a_0 = \frac{4\pi\epsilon_0\hbar^2}{e^2 m_e}$, yielding a value of approximately 5.29×10^{-11}m. Further measurements and theoretical calculations of Feshbach resonances in magnetic lanthanides have been commented on in more detail in [6].

In many atomic systems, the character and location of Feshbach resonances can be calculated with high precision. Nevertheless, the added complexity in lanthanides caused by the inter-level structure and coupling mechanisms increases the difficulty of accurately describing Feshbach resonances, thus thorough experimental surveys are necessary. Key measurements performed by various groups including Maier et al. [7] and Durastante et al. [8] by means of atomic-loss spectroscopy have enabled accurate identification of resonances for ^{164}Dy, and ^{161}Dy and ^{164}Dy, respectively. The spectrum shown in figure 2.1 demonstrates the high density of resonance positions, even for low magnetic fields. Additionally, broad Feshbach resonances decouple from the chaotic background and offer a large range of possibilities for tuning interactions for the study of few- and many-body physics [9].

2.2 Dysprosium Quantum Gases

The new experiment being built at Heidelberg by the name of DyLab aims to study ultracold quantum gases of **highly magnetic dysprosium atoms**. For highly magnetic elements, like dysprosium, the dipole-dipole interaction competes with the above-mentioned contact interaction. The following section gives an introduction to some key properties of Dy, and later on, focuses on the dipolar interaction and its effect on the behavior of ultracold quantum gases.

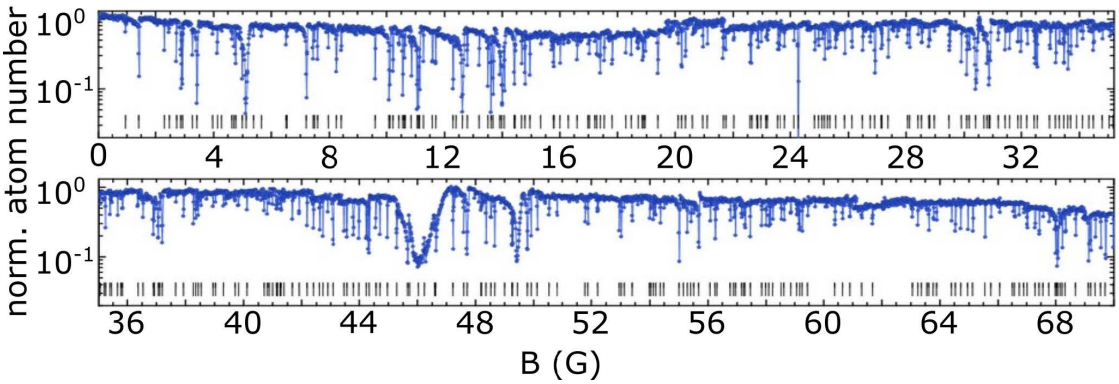

Figure 2.1: *Feshbach resonances for ^{164}Dy measured by atomic loss for a large range of magnetic fields. The measurements between no magnetic field (0 G) and large magnetic fields (68 G) demonstrate a high density of resonances that can be exploited for the tuning of contact interactions. Taken from [7].*

2.2.1 Dysprosium Properties

Dysprosium (Dy) is a rare-earth element with the atomic number 66. Identified first in 1886 by Paul Emile Lecoq de Boisbaudran, it was not isolated to its pure form until the 1950s, when ion exchange techniques became available. Dysprosium, along with holmium, has the highest magnetic strength on the periodic table [10]. Additionally, naturally occurring dysprosium is composed of seven stable isotopes, with ^{161}Dy , ^{162}Dy, ^{163}Dy, ^{164}Dy showing similar abundance. In the frame of this work, we focus on the ^{164}Dy isotope.

Isotope	^{161}Dy	^{162}Dy	^{163}Dy	^{164}Dy
Natural Abundance %	18.889	25.475	24.896	28.26
Atomic Mass	160.927	161.927	162.928	163.929
Neutron Number (N)	95	96	97	98
Nuclear Spin	$\frac{5}{2}$	0	$\frac{5}{2}$	0

Table 2.1: *Most abundant dysprosium isotopes and their properties. Two isotopes with no nuclear spin, ^{162}Dy and ^{164}Dy, are available for the study of bosonic quantum gases.*

Electronic configuration

The ground state electronic configuration for dysprosium is given by

$$[1s^2 2s^2 2p^6 3s^2 3p^6 3d^{10} 4s^2 4p^6 4d^{10} 5s^2 5p^6]_{Xe} 4f^{10} 6s^2 \tag{2.10}$$

As seen in figure 2.2, four electrons on the 4f-shell with angular momenta $l_i = 0,1,2,3$ remain unpaired. The ground state can therefore be described by the quantum numbers $L = 6$ and $S = 2$. The (LS)-coupling formalism yields a total angular momentum $J = 8$ so that the ground state can be written as ${}^5I_8$.

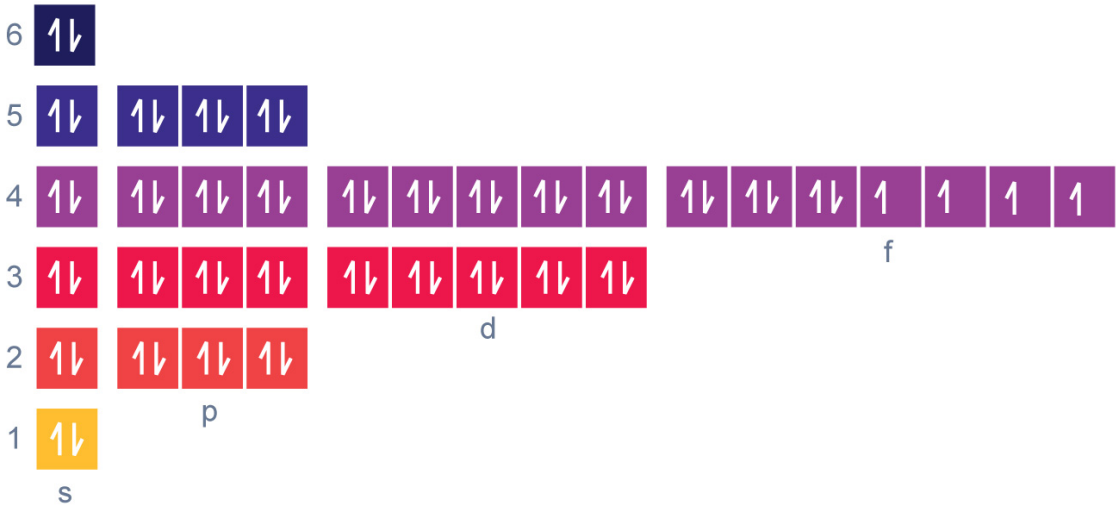

Figure 2.2: *Dysprosium orbital diagram. The principal quantum number n is shown on the left. For the ground state of Dy electrons partially fill up to $n = 6$ following Hund's rules. The azimuthal quantum number l, which determines the quantum state of the electrons, is shown in historical letters notation. The 12 valence electrons correspond to one pair of electrons on the 6s-shell, and 3 pairs and 4 unpaired electrons on the 4f-shell.*

Generally speaking, the excitation spectrum of dysprosium arising from its electronic structure is rather complex. However, it is dominated by the broadest transition line ($\Gamma/2\pi = 32.2$MHz) at 421 nm. This particular transition takes place between the initial state $4f^{10}6s^2({}^5I_8)$, $J = 8$ and the final state $4f^{10}6s6p({}^1P_1)$, $J = 9$.

Magnetic Moment

In the case of bosonic atoms with no hyperfine levels, one can define the magnetic moment as

$$\mu = m_J g_J \mu_B \tag{2.11}$$

where m_J is the total angular momentum of the electron projected onto the quantization axis, μ_B the Bohr magneton, and g_J the well known g-factor approximately given by

$$g_J = 1 + (g_s - 1)\frac{J(J+1) + S(S+1) - L(L+1)}{2J(J+1)}. \tag{2.12}$$

For the ground state of dysprosium with $m_J = -8$, the approximation for the g-factor yields $g_J = 1.25$. Dysprosium then has a total magnetic moment of $9.93\mu_B$ at its ground state. This value will strongly define the strength of the dipolar interaction described below.

2.2.2 Dipolar Interactions

An additional competing interaction, the dipole-dipole interaction arises from the fact that some atomic species, like Dy, present a permanent magnetic dipole moment even at zero fields. A general description of the dipolar potential between two dipoles at a distance **r** yields [6]

$$V_{\mathrm{dd}}(\mathbf{r}) = \frac{\mu_0}{4\pi r^3}\left[\mathbf{d_1}\cdot\mathbf{d_2} - 3\frac{(\mathbf{d_1}\cdot\mathbf{r})(\mathbf{d_2}\cdot\mathbf{r})}{r^2}\right] \tag{2.13}$$

where μ_0 is the vacuum permeability, r the distance between the dipoles, and d_1 the dipole moment of each particle. Figure 2.3 represents the governing parameters defining the DDI. The dipolar interaction is **long-range** and **anisotropic**, which greatly impacts the properties of dipolar gases. Altogether, the dipolar interaction is attractive in one direction and repulsive in the remaining two directions.

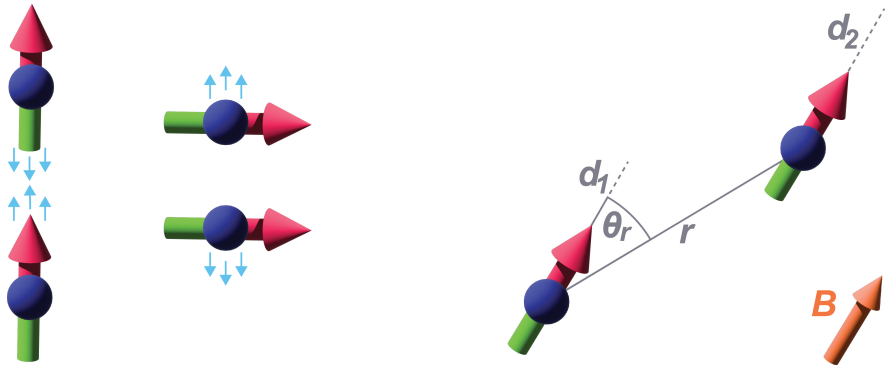

Figure 2.3: *Visual representation of the parameters governing the dipole-dipole interaction.* ***left:*** *The orientation of two dipoles relative two each other determines if the average force is attractive or repulsive. Two simple cases, $\theta_r = 0°$ and $\theta_r = 90°$, are demonstrated here.* ***right:*** *In more complex cases the force is determined by the potential defined in equation 2.14.*

In a fully polarized system, where $|\mathbf{d_1}| = |\mathbf{d_2}| = \mu$, where μ is defined in equation (2.11) for dysprosium, equation (2.2.2) becomes

$$V_{\mathrm{dd}}(\mathbf{r}) = \frac{C_{\mathrm{dd}}}{4\pi} \frac{1 - 3\cos^2(\theta)}{|r|^3}, \tag{2.14}$$

where θ is the angle between $\mathbf{r}$ and the polarization axis of the dipoles. The interaction strength C_{dd} is given by $C_{\mathrm{dd}} = \mu_0 \mu^2$, where μ_0 denotes the vacuum permeability.

Overall, the dipolar potential in (2.14) is described by the spherical harmonics Y_2^j [6]. Consequently, the integration over a 3D space averages zero, and the average interaction between particles depends strongly on the geometry of the atomic cloud. Figure 2.4 shows two examples of this effect on the average DDI of the system. On the left, a prolate trapped condensate displays an overall attractive force between the particle. In comparison, an oblate-trapped condensate shows a repulsive interaction of the particles.

Earlier, the GPE that describes the behavior of BECs has been introduced in equation (2.6). In the case of dBECs, the interaction term is the sum of the simple contact term in (2.8) and the dipolar interaction term (2.14). Properties

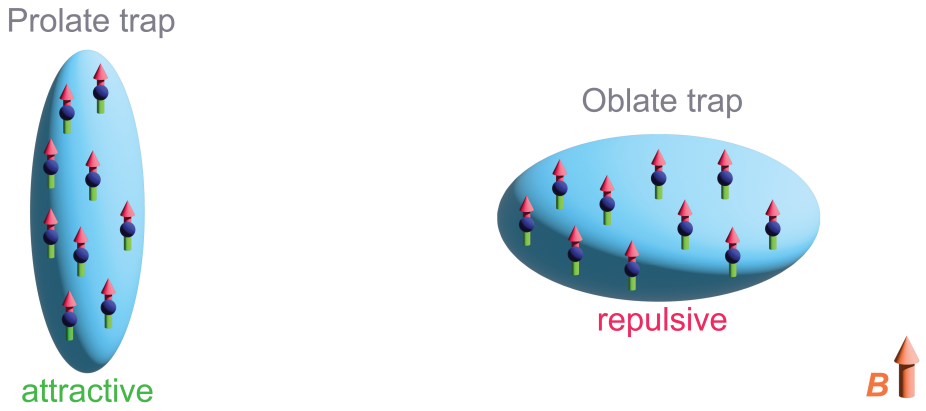

Figure 2.4: *Effect of trapping geometries on DDIs. The relative orientation of the dipoles, defined by an external magnetic field B, with respect to the interatomic axis, determines the nature of the average dipole-dipole interaction. A condensate in a prolate trap averages to an overall attractive interaction. In comparison, an oblate trap results in a overall repulsive interaction.*

of dilute dipolar quantum gases can then adequately be described by

$$i\hbar\partial_t\psi = \left[\frac{\hbar^2\nabla^2}{2m} + U_{\text{ext}}(r) + g|\psi|^2 + \Phi_{\text{dd}}(r,t)\right]\psi. \tag{2.15}$$

The mean field associated with the DDI $\Phi_{\text{dd}}(r,t)$ is given by

$$\Phi_{\text{dd}}(r,t) = \int dr'|\psi(\mathbf{r}',t)|^2 V_{\text{dd}}(\mathbf{r}-\mathbf{r}'). \tag{2.16}$$

Finally, the interaction strength of DDI with respect to the aforementioned contact interaction can be quantified by the dimensionless parameter ϵ_{dd}

$$\epsilon_{\text{dd}} = \frac{C_{\text{dd}}m}{3\hbar^2 a_s} = \frac{a_{\text{dd}}}{a_s} \tag{2.17}$$

The natural value for the dipolar length a_{dd} of ^{164}Dy is $130a_0$. Considering the natural value of the contact interaction strength for ^{164}Dy, it follows that $\epsilon_{\text{dd}} = 1.45$. As $\epsilon_{\text{dd}} \geq 1$, it is understood that under natural conditions the dipolar force dominates over the contact interaction.

2.3 Dipolar Quantum Gases in Two Dimensions

2.3.1 New States of Matter in Dipolar Quantum Gases

In the mean-field theory framework, instabilities in dBECs lead to singularities for infinite density for the many-body ground state, meaning that in general, this approach breaks down and the state becomes unstable [6]. In the case of dipolar gases, it was observed experimentally that instead of instability dynamics, an additional stabilization arises. These observations were later understood as the emergence of new ground states, which are stabilized beyond mean-field interactions [6]. The nature of this stabilization and the emerging **new states in dipolar quantum gases** are subject to this section

Taking into account quantum fluctuations by a local density approximation of the first order beyond mean field correction to the ground state energy of the system called the Lee-Huang-Yang correction, the behavior of the dipolar BECs can be suitably explained and these novel states arrived at even theoretically. This correction provides the necessary repulsion that counterbalances the mean field attraction at high densities.

In the case of no confinement, dipolar gases beyond mean field instability form droplets corresponding to self-bound states. A transition to even more exotic states can be expected once anisotropic trapping is introduced. In cases of strong confinement along the dipoles, self-density modulated states can occur beyond mean-field instability. It was further found that there is a narrow regime, which can be entered by a fine-tuning of the s-wave scattering length, that allows for both spatial modulation in density and global phase coherence, so-called supersolidity. This name is given as the state simultaneously displays properties of both crystals and superfluids; a consequence of the simultaneous breaking of both translational invariance and U(1) gauge symmetry. This variety of states has been observed in experiment on 3D gases of Er and Dy [6].

2.3.2 Two Dimensional Bose Gas: BKT Transition

As described in section 2.1.1, Bose-Einstein Condensation in a 3-dimensional, non-interacting bosonic system is expected in the thermodynamic limit ($N \to \infty$ and $\omega \to 0$). However, in 2-dimensional cases, the population in the excited states is not bounded (equation (2.4) diverges), which means that the system

does not undergo Bose-Einstein condensation. At finite temperature, at the thermodynamic limit, and for a system that is short-range interacting, the long-range order of the phase of the macroscopic wave function is broken by thermal fluctuations in 2D [11]. This is because in these low dimensions, at non-zero temperatures, thermal fluctuations have an enhanced role destroying long-range ordering.

In presence of interactions, another kind of phase transition is possible based on the Berezinskii–Kosterlitz–Thouless (BKT) mechanism. This transition occurs via the pairing of defects of topological nature below a certain critical temperature, such as vortices for superfluidity and dislocation for solid systems [3]. The microscopic mechanism of the BKT phase transition is usually described in terms of the energetics of the topological defects. The free energy of the vortices involves a competition between the interaction energy and entropy resulting in a logarithmic dependence on the system size scaled by the healing length. This competition results in the transition between an ordered and a disordered state – below the BKT critical temperature, there is the ordered state characterized by bound pairs of vortices with opposite circulations. Above the BKT critical temperature, there is an unbinding of the vortex pairs and proliferation of free vortices, resulting in a disordered state of phase defects. This mechanism has been observed in a variety of systems, in particular in contact interacting gases like BEC. The relevance of this mechanism however depends on the range of the inter-particle interaction. If there are long-range interactions on top like the dipole-dipole interactions, this quasi-long-range ordering may break, unless there is a screening effect of the bound vortex pairs which if present can restore the quasi-long-range ordering. There is also the possibility of some unconventional type of quasi-long-range ordering, especially in the novel, exotic phases.

In the DyLab in Heidelberg, we want to investigate the new kind of dipolar orders that can exist in 2D ultracold gases and the relevance of the BKT mechanism for the underlying phase transitions.

2.4 The Dylab

In the DyLab in Heidelberg, a new setup focused on ultracold quantum gases of dysprosium is being prepared for the study of new states of matter in dipo-

lar quantum gases, and of the overall effects of low temperatures and low-dimensionality on the competing interparticle interactions. This section consists of an overview of the process and experimental setup leading to the 2-dimensional trapping on which this thesis is based.

2.4.1 Overview

The dysprosium atoms used in the DyLab come from a high-temperature dual cell oven with a reservoir at 800° and 1100°C hot lip. The atomic jet is directed towards a 2D-MOT chamber, where the atoms are cooled down and trapped in two directions by four laser beams at 421 nm. The first steps for the vacuum design have been performed by Christian Gölzhäuser during his bachelor thesis [12]. The atoms captured in the 2D-MOT are then redirected by a push-Beam towards the main chamber, where the atoms are recaptured by a red 3D-MOT working on the 626 nm intercombination line of Dy. The atoms are later more tightly confined by a crossed optical dipole trap at 1064 nm and cooled by evaporative cooling. Afterwards, an accordion lattice formed by laser beams at 532 nm, an additional optical dipole trap with tunable periodicity, will be implemented to reach a two-dimensional probe of dysprosium atoms. The design of this trap is the subject of the present thesis. The main experimental setup can be observed in figure 2.5.

Note that our experimental design for the first time implements a 2D-MOT and excludes the use of a Zeeman slower to produce ultracold gases of dysprosium. The 2D-MOT and 3D-MOT designs have been carefully developed to account for this new approach. A better description of the designed chambers can be found in [13] and [12]. Additionally, up until now custom-designed magnetic coils and a crossed dipole trap have been successfully installed [14], [15], [16]. At the moment, a temperature of 300 nK for a cloud of 1×10^5 atoms has been achieved through evaporative cooling in the crossed dipole trap. The design of the accordion lattice, and characterization of the objective lens for imaging are currently being carried out and will be installed in the near future.

2.4.2 Science Chamber

The accordion lattice designed for the DyLab will be superimposed on the optical dipole trap in the main chamber of the experiment. Therefore, the dimensions of the main chamber also called the **science chamber**, and the optical access possibilities represent the main limiting factors for the design of the lattice

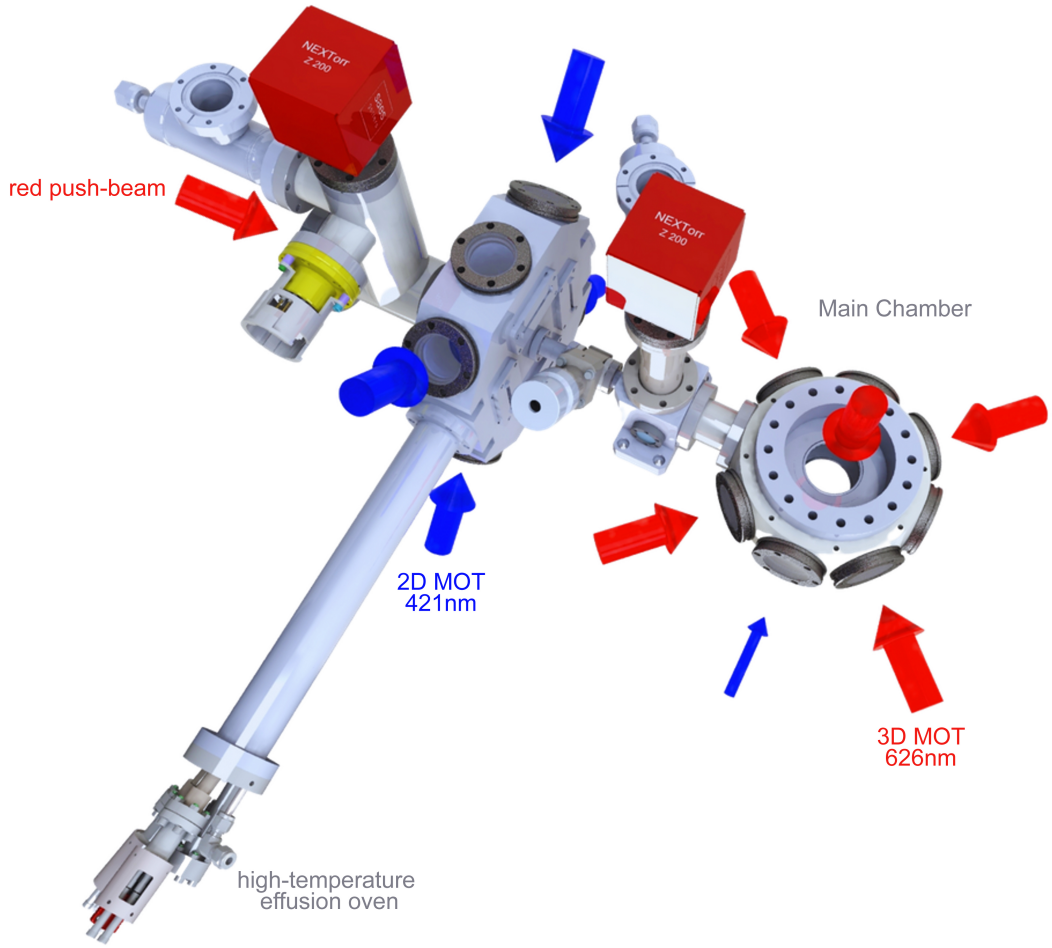

Figure 2.5: *Overview of the main experimental setup. An atomic jet of dysprosium atoms is created by a high-temperature effusion oven and captured by a 2D-MOT (*421 nm*). A push beam (*626 nm*) redirects the atoms towards a 3D-MOT (*626 nm*), where the atoms are recaptured, cooled down and compressed, reaching the BEC regime. The atom cloud is then more tightly confined by a crossed optical dipole trap (*1064 nm*), and finally a quasi- 2-dimensional probe is achieved by an accordion lattice (*532 nm*), which confines the atoms strongly in the vertical direction.*

itself.

The science chamber follows a standardized design with eight CF40 flanges on the side and two CF100 flanges at the top. On seven of the CF40 flanges, view-ports with optical-grade fused silica windows have been installed. The laser beams responsible for the formation of the accordion lattice will be entering the science chamber on one of the side viewports, see figure 2.5. The control setup for the optical accordion will be installed after the opposing window, i.e where the laser beams exit the chamber. Figure 2.6 shows a cut of the main

chamber, detailing the specific dimensions which will be defined for the accordion lattice setup: the distance from the viewport's window to the center of the main chamber (98.1 mm), the thickness of the window (3.2 mm), and its clear aperture (32 mm). In the vertical direction, the center of the scientific chamber

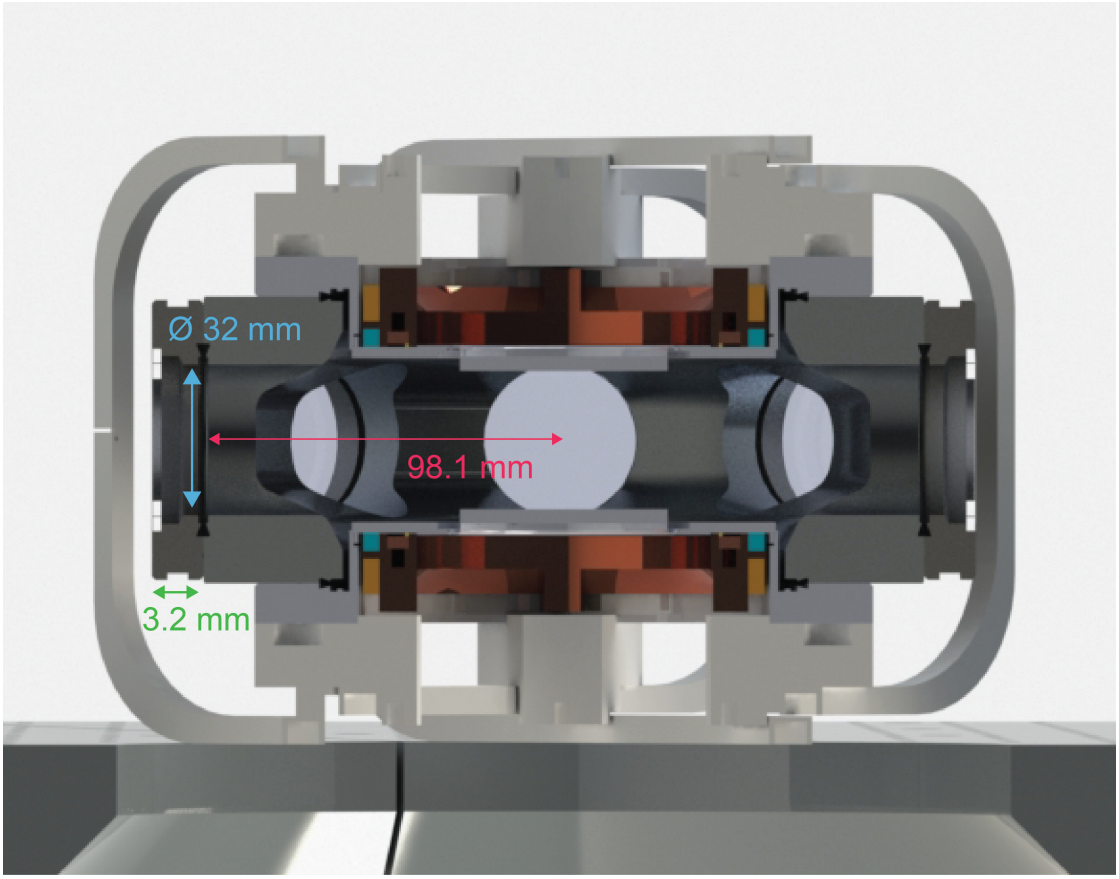

Figure 2.6: *Overview of science chamber's dimensions. The diameter and thickness of the view port's window and the distance from the view-port to the center of the chamber where the atoms will be placed, are the main limiting factors for the design of the accordion lattice.*

where the dBEC of dysprosium will be is placed at 75 mm from the optical table, which determines the height of the optical path. Furthermore, continuing with the general design concept of the whole experiment, the accordion lattice setup should be as compact as possible and optimized for stability.

Chapter 3

Theoretical Thoughts

The main goal of this work is to design and implement the first test setup of an optical dipole trap that allows entering the quasi-2D regime to probe bosonic quantum gases of dysprosium. The first section of this chapter will summarize the main theoretical concepts that enable the optical trapping of dysprosium and the different methods that have been used so far. The second section will discuss the existing experimental implementations that make it possible to tightly confine atomic clouds in one or two directions and their corresponding advantages and disadvantages. In the end, the method chosen to realize the 2D trap of dysprosium, the Accordion Lattice, and the most important concepts will be explained.

3.1 Optical trapping of Dysprosium

Optical dipole trapping is one of the main methods that can be exploited to produce ensembles of ultracold quantum gases of neutral atoms. This method relies on the electric dipole interaction of atoms with far-detuned light. The following section consists of a brief introduction to the theoretical description of Optical Dipole Traps (ODT) based on the 1999 Review by Grimm, Weidemüller, and Ovchinnikov [17]. Afterwards, the main requirements for trapping dysprosium atoms are summarized.

3.1.1 Trapping of neutral atoms: Atom-Light Interaction

Optical traps realized with far-detuned light are of great interest due to the low optical excitation and the negligible radiation force due to photon scattering. Furthermore, they provide a large range of trap geometries, including anisotropic or multi-well potentials. A simple semi-classical approach, in which a neutral atom is considered an oscillator in a classical radiation field, allows for the derivation of the most important equations for the description of the potential. The monochromatic laser light used for optical trapping can be described by its electric field **E**

$$\mathbf{E}(\mathbf{r},t) = \hat{\mathbf{e}}\tilde{E}(\mathbf{r})\exp(-i\omega t) + c.c \tag{3.1}$$

where $\hat{\mathbf{e}}$ is the unit polarization vector, $\tilde{E}$ the field amplitude, and ω the driving frequency. The light induces an atomic dipole moment on the atom

$$\mathbf{p}(\mathbf{r},t) = \hat{\mathbf{e}}\tilde{p}(\mathbf{r})\exp(-i\omega t) + c.c \tag{3.2}$$

where the amplitude $\tilde{p}$ relates to the electric field by the dynamical polarizability of the atom α

$$\tilde{p} = \alpha\tilde{E}. \tag{3.3}$$

The dipole force F_{dip} is given by the gradient of the interaction potential U_{dip}, where

$$U_{\text{dip}} = \frac{\langle \mathbf{pE} \rangle}{2} = \frac{\text{Re}(\alpha)I}{2\epsilon_0 c} \tag{3.4}$$

$$F_{\text{dip}}(\mathbf{r}) = -\nabla U_{\text{dip}(\mathbf{r})} = \frac{\text{Re}(\alpha)}{2\epsilon_0 c}\nabla I(\mathbf{r}). \tag{3.5}$$

The resulting force is conservative and can therefore only be used for trapping and not for cooling purposes.

Another key quantity is the scattering rate Γ_{sca}, which arises from the ratio between the power absorbed by the oscillator from the driving field P_{abs} and

the photon energy $\hbar\omega$

$$P_{\text{abs}} = \langle \dot{\mathbf{p}}\mathbf{E} \rangle = \frac{\omega \,\text{Im}(\alpha) I}{\epsilon_0 c} \tag{3.6}$$

$$\Gamma_{\text{sca}} = \frac{P_{\text{abs}}}{\hbar\omega} = \frac{\text{Im}(\alpha) I(\mathbf{r})}{\hbar\epsilon_0 c}. \tag{3.7}$$

The complex polarizability α can be computed by considering the atom in Lorentz's model of a classical oscillator. Hereby, the electron is considered to be bound elastically to the nucleus of the atom with an oscillating frequency ω_0, which corresponds to the frequency of the optical transition. According to Larmor's formula, the dipole radiation of the oscillating electron results in a classical damping rate Γ_ω. Integration of the equation of motion of the modeled driven oscillator, yields

$$\Gamma_\omega = \frac{e^2\omega^2}{6\pi\epsilon_0 m_e c^3} \tag{3.8}$$

$$\Gamma \equiv \Gamma_{\omega_0} = (\omega_0/\omega)^2 \Gamma_\omega \tag{3.9}$$

$$\alpha = \frac{e^2}{m_e} \frac{1}{\omega_0^2 - \omega^2 - i\omega\Gamma_\omega} = 6\pi\epsilon_0 c^3 \frac{\Gamma/\omega_0^2}{\omega_0^2 - \omega^2 - i(\omega^3/\omega_0^2)\Gamma}. \tag{3.10}$$

This description of the polarizability α is only valid for far-detuned light with very low scattering rates ($\Gamma_{\text{sca}} \gg \Gamma$). Following the rotating wave approximation, the main expressions for the dipole potential and the scattering rate can be written in terms of the detuning $\Delta \equiv \omega - \omega_0$, with

$$U_{\text{dip}}(\mathbf{r}) = \frac{3\pi c^2}{2\omega_0^3} \frac{\Gamma}{\Delta} I(\mathbf{r}) \tag{3.11}$$

$$\Gamma_{\text{sca}}(\mathbf{r}) = \frac{3\pi c^2}{2\omega_0^3} \left(\frac{\Gamma}{\Delta}\right)^2 I(\mathbf{r}). \tag{3.12}$$

The sign of the detuning determines if atoms are confined by a far-detuned source at points of maximal or minimal intensity. In the case of so-called **red detuning** ($\Delta \leq 0$) the dipole potential is negative and the interaction attracts the atoms into the electric field. On the other hand, so-called **blue detuning** ($\Delta \leq 0$) causes the atoms to be repelled by the light field and confines them at the minima of the dipole potential. Because atoms in reality have more than one excited

state, a full description considers the sum over all excited states.

3.1.2 Polarizability of Dysprosium

In the case of dysprosium, a more thorough calculation of the real and imaginary parts of polarizability is necessary, in which the anisotropy caused by the non-zero orbital momentum is considered. This means that not only the scalar polarizability coefficient α_s is taken into account, but also the vectorial α_v and tensorial α_t ones. A general formula for the polarizability is given by

$$\alpha(\omega) = \alpha_s(\omega) + i\frac{[\mathbf{u}^* \times \mathbf{u}] \cdot \mathbf{J}}{2J}\alpha_v(\omega) \tag{3.13}$$

$$+ \frac{J(J+1) - 3m_j^2}{J(2J-1)}\frac{1 - 3\cos^2(\theta_p)}{2}\alpha_t(\omega), \tag{3.14}$$

where $\mathbf{u}$ is the polarization vector of the laser field and θ_p the orientation of $\mathbf{u}$ with respect to an external magnetic field $\mathbf{B}$. The scalar polarizability coefficient accounts for the diagonal elements of the polarizability tensor. Additionally, the vectorial coefficient accounts for the anti-symmetric parts of the off-diagonal elements, while the tensorial coefficient introduces the symmetric parts of the off-diagonal elements. A simplified case can be found for linearly polarized light, where the middle term vanishes as $\mathbf{u}^* \times \mathbf{u} = 0$.

Altogether, the values for the polarizability of dysprosium for various wavelengths are based on theoretical calculations rather than experimental measurements. Some publications, like [18] and [19], have dealt in great depth with the computation of theoretical values for all coefficients of the polarizability of Dy, which are useful for numerical simulations of ODT (see figure 3.1.

Now it is necessary to find an appropriate wavelength that is far from any resonances with respect to the dynamic polarizability of dysprosium, and that is far detuned from any main transitions. Additionally, due to tight confinement that is expected, high-power laser sources show be readily available.

The main two options to realize the accordion lattice are either a 532 nm or a 1064 nm, both red detuned from Dy. Theoretical values for the polarizability at these wavelengths are found to be $\alpha(532\text{nm}) = 350\text{a.u}$ and $\alpha(1064\text{nm}) = 193\text{a.u}$.

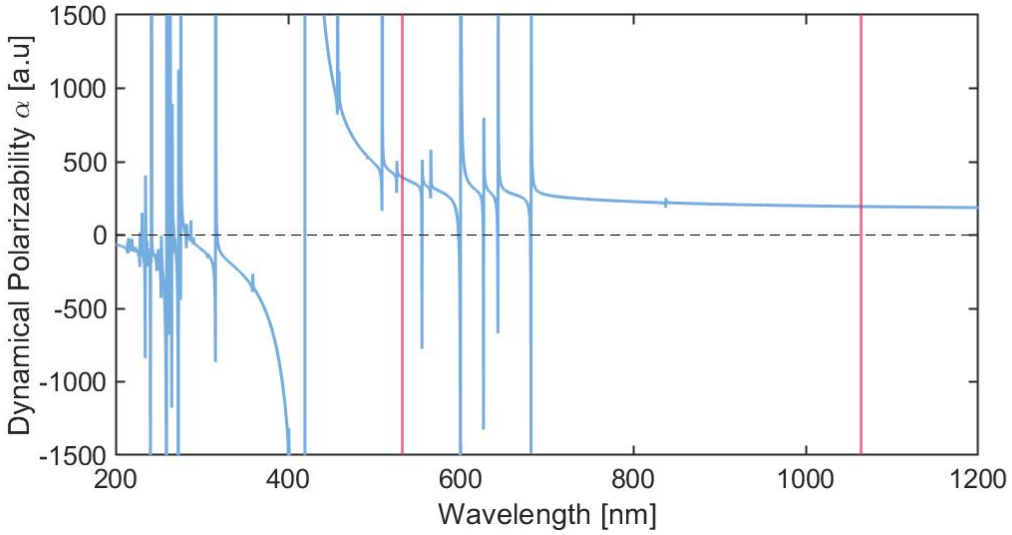

Figure 3.1: *Dynamical Polarizability of Dysprosium for linearly polarized ligth as a function of the wavelength. The two main candidates for the realization of a red-detuned optical trap* (532 nm *and* 1064 nm *are marked in red [18]. The polarizability for both wavelengths is positive and far away from resonances.*

As mentioned before, the wavelength will directly influence the trap's depth and shape. A more detailed look on the final choice of wavelength is given once the geometry of the trap, defined by the trapping frequencies ω_i, comes into play, in chapter 4.

3.1.3 Red-detuned Optical Dipole Traps

In cases where the light field is tuned below the atomic frequency, the dipole force points towards increasing intensity. In other words, in red-detuned optical dipole traps (see Section 3.1), the atoms are trapped in the region of maximum density. A considerable advantage of red-detuned traps is that the focus of a laser beam by itself constitutes a stable dipole trap for atoms. Overall, the trap's depth is determined by the laser´s power and the beam shape, and with available laser sources, common values for trap depths are in the range of the millikelvin. Although a simple single-beam trap can be easily realized, combinations of multiple lasers lead to a wider range of trap geometries and lattices adequate for the confinement of ultracold quantum gases. Overall, it is common to use a harmonic oscillator approximation near the maximal intensity to calculate the effective trapping frequency of a red-detuned trap. The general

formula for a harmonic trap in 3-dimensions is given by

$$U_{\mathrm{HO}} = U_0 + \frac{m}{2}\left(\omega_x^2 x^2 + \omega_y^2 y^2 + \omega_z^2 z^2\right), \tag{3.15}$$

where m is the mass of the atoms and ω_i are the angular trapping frequencies on the three main directions defined by x, y and z. In the next sections, we will refer to the trapping frequencies as ν_i, with $\nu_i = \frac{\omega_i}{2\pi}$.

3.2 Two-Dimensional Traps

The realization of two-dimensional systems is no trivial task, and different methods should be taken into account with no disregard for the difficulties that may appear during experimental implementations and the flexibility they may provide. In this section, the 3-dimensional harmonic trap will be discussed first, and the conditions for achieving reduced dimensionality will follow after.

The fundamental idea behind 2-dimensional trapping is to confine the atoms tightly in one direction so that the motion is effectively frozen in that direction and the atoms can only move in the **residual plane** defined by the remaining two axes. The potential is then highly asymmetric with $\omega_z \gg w_x, w_y$. In order to achieve a strong enough confinement, the trap potential must fulfill the condition

$$\hbar\omega_z \gg k_B T, \mu, \tag{3.16}$$

where T is the temperature of the trapped particles and μ the chemical potential. This condition implies that the atoms occupy only the lowest-energy harmonic oscillator state in the axial direction. For temperatures in the range of 100 nK, the trapping frequency ν_z must be well over 2000 Hz.

Generally speaking, a single-beam red-detuned ODT could be introduced to achieve the desired asymmetrical trapping frequencies. However, such a simple method results in strong limitations for the experimental implementation, such as little control over the geometry of the trap and constraints related to the availability of cylindrical lenses that can be adapted to our setup. A common method to achieve strong confinement in one direction, which furthermore, of-

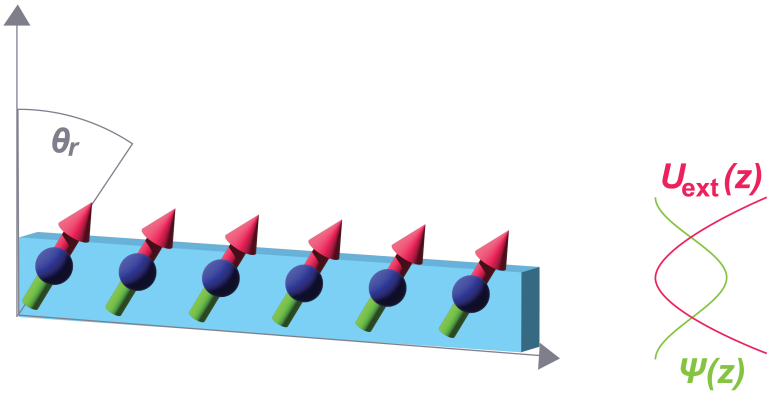

Figure 3.2: *Tight confinement of dipolar atoms in one direction. The strong trapping potential U_{ext} in one direction must fulfill the condition $\hbar\omega_z \gg k_B T, \mu$ to guarantee 2D confinement.*

fers high control over the trap geometry and tunability of the trap's size during measurements, as well as of the trapping frequencies, is the so-called **accordion lattice.**

3.3 Overview of an Accordion Lattice

The following section describes the working principle of the optical accordion, the main equations, and the considerations for its experimental realization.

Working principle

An accordion lattice is an optical trap that enables tight confinement of a cloud of atoms in one direction while providing real-time control of the trap's periodicity. First achieved by Li, Kelkar, Medellin, and Raizen in 2008 [20], the optical accordion demonstrates highly controllable spacing that enables continuous and stable trapping [21]. To date, multiple accordion lattices have been successfully designed and implemented [22], [23], [24].

The basic concept behind the design, depicted in figure 3.3, is that two laser beams interfere at a shallow angle 2θ and create a periodic trapping potential in one direction. For beams propagating in the x-direction, the half-angle θ between the beams is defined on the x-z plane and the periodic confinement arises in z-direction.

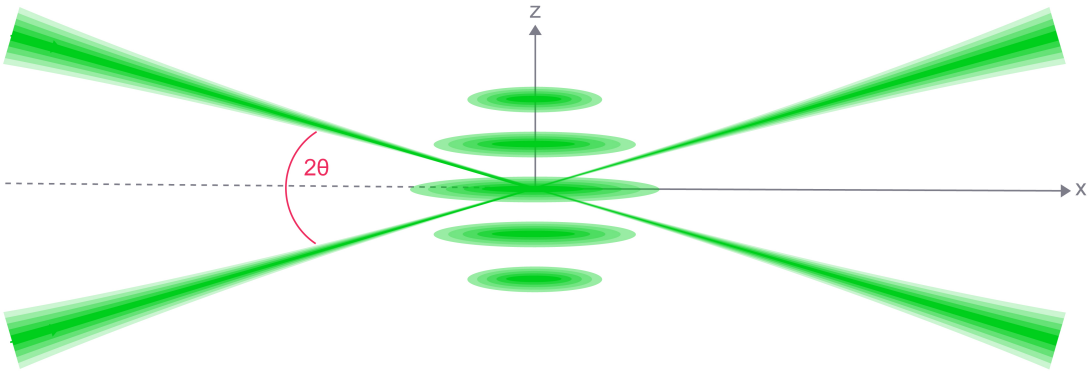

Figure 3.3: *Working principle of an accordion lattice. Two beams interfere at a shallow half-angle θ, producing a periodic potential in one direction.*

The laser beams used to realize the accordion lattice are assumed to follow an ideal Gaussian distribution. In general, an elliptical Gaussian beam propagating along the x-direction, as shown in figure 3.4, can be characterized by its electric field $\mathbf{E}$, such that

$$\mathbf{E} = \mathbf{E_0}\sqrt{\frac{w_{y_0}w_{z_0}}{w_y(x)w_z(x)}}\exp\left[-\left(\frac{z}{w_z(x)}\right)^2-\left(\frac{y}{w_y(x)}\right)^2\right]\exp[i(kx+\varphi(x,y,z))] \tag{3.17}$$

$$\tag{3.18}$$

$$k = \frac{2\pi}{\lambda} \tag{3.19}$$

$$w_i(x) = w_{i_0}\sqrt{1+\left(\frac{x}{x_{R_i}}\right)^2} \tag{3.20}$$

$$x_{R_i} = \frac{\pi w_{i_0}^2}{\lambda} \tag{3.21}$$

$$\varphi(x,y,z) = \frac{kz^2}{2R_z(x)}+\frac{ky^2}{2R_y(x)}-\Psi+\delta \tag{3.22}$$

$$\Psi = \arctan\left(\frac{\lambda x}{\pi w_{z_0}w_{y_0}}\right) \tag{3.23}$$

$$R_i(x) = x\left(1+\left(\frac{x_{R_i}}{x}\right)^2\right) \tag{3.24}$$

where k is the wave vector, w_{i_0} is the beam waist in i-direction with $i = y,z$, x_{R_i}

is the Rayleigh length, $R_i(x)$ is the radius of curvature, Ψ the Gouy phase at x, and δ the beam's phase.

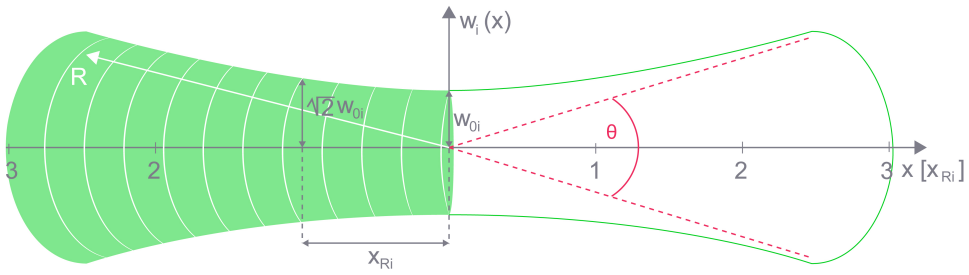

Figure 3.4: *Key properties of an ideal Gaussian beam propagating along the x-axis. The beam radius in i-direction $w_i(z)$, with $i = y,z$ expands from the initial beam waist w_{i0} according to eq. (3.20). At the Rayleigh length x_{Ri}, the beam radius equal $\sqrt{2}w_{i0}$.*

This expression can be applied to simulate an accordion lattice resulting from the interference of two beams at a half-angle θ by rotating the coordinates in equation (3.17) around the y-axis by θ and $-\theta$. The intensity of the interference pattern is then given by

$$I_{\text{tot}}(x,y,z) = |\mathbf{E}_\theta + \mathbf{E}_{-\theta}|^2 \tag{3.25}$$

$$= |\mathbf{E}_\theta|^2 + |\mathbf{E}_{-\theta}|^2 + \mathbf{E}_\theta^* \mathbf{E}_{-\theta} + \mathbf{E}_\theta \mathbf{E}_{-\theta}^* \tag{3.26}$$

where $\mathbf{E}_\theta$ and $\mathbf{E}_{-\theta}$ are the electrical fields for the rotated beams. Assuming both beams have equal linear polarization, the total intensity can be expressed in terms of the individual intensities as

$$I_{\text{tot}}(x,y,z) = I_\theta + I_{-\theta} + 2\sqrt{I_\theta}\sqrt{I_{-\theta}} \cdot \cos\left(\frac{4\pi}{\lambda} z \sin(\theta) + \Delta\varphi\right). \tag{3.27}$$

Here $\Delta\varphi = \varphi_\theta - \varphi_{-\theta}$. The intensities of the individual beams I_θ and $I_{-\theta}$ individually carry the Gaussian term given in equation (3.17). Consequently, the resulting interference pattern is wrapped as well in a Gaussian envelope dominating the intensity distribution. This distribution becomes evident once I_θ and $I_{-\theta}$ are explicitly written as a function of the beam waists w_z and w_y, and the

power P of each beam:

$$I_\theta(x,y,z) = \frac{2P}{\pi w_y(x_\theta) w_z(x_\theta)} \exp\left(-\frac{2y^2}{w_y^2(x_\theta)} - \frac{2(z\cos(\theta) + x\sin(\theta))^2}{w_z^2(x_\theta)}\right) \tag{3.28}$$

$$I_{-\theta}(x,y,z) = \frac{2P}{\pi w_y(x_{-\theta}) w_z(x_{-\theta})} \exp\left(-\frac{2y^2}{w_y^2(x_{-\theta})} - \frac{2(z\cos(\theta) - x\sin(\theta))^2}{w_z^2(x_{-\theta})}\right) \tag{3.29}$$

A very thorough explanation of the process to compute the interference pattern of an accordion lattice can be found in [25]. The cosinusoidal term in equation (3.27) is responsible for the characteristic periodicity of the accordion lattice observed in figure 3.5, i.e the spacing between the nodes resulting from constructive and destructive interference. The so-called fringe spacing d has the form

$$d = \frac{\lambda}{2\sin(\theta)}. \tag{3.30}$$

So that equation (3.27) can be rewritten as

$$I_{\text{tot}}(x,y,z) = I_\theta + I_{-\theta} + 2\sqrt{I_\theta}\sqrt{I_{-\theta}} \cdot \cos\left(\frac{2\pi}{d} z + \Delta\varphi\right). \tag{3.31}$$

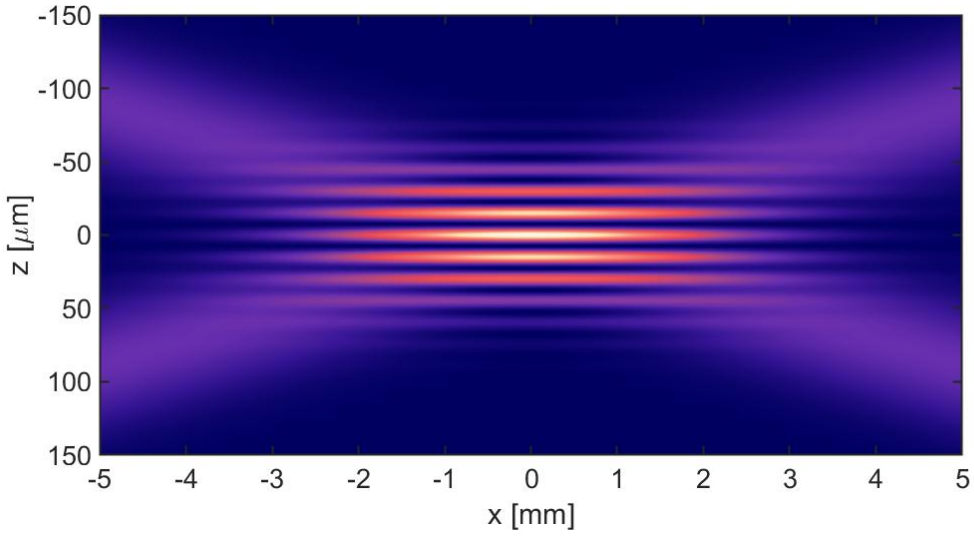

Figure 3.5: *Example of an optical accordion resulting from two interfering beams. The periodicity arising from the cosinusoidal term creates so-called fringes with high intensity where atoms can be trapped.*

Finally, the trapping potential in the z-direction can effectively be described by a convolution of a Gaussian curve- arising from the Gaussian nature of the individual beams- and a cosinusoidal function reflecting the periodicity.

In the case of a red-detuned light source, the atoms can be trapped at points of maximal intensity following the explanation given in section 3.1. The trap depth as well as the trapping frequencies can be extracted by approximating the final trapping potential to an harmonic oscillator.

$$U(x,y,z) = \frac{I_{\text{tot}}(x,y,z)\alpha}{2c\epsilon_0} \approx U_{\text{HO}} \tag{3.32}$$

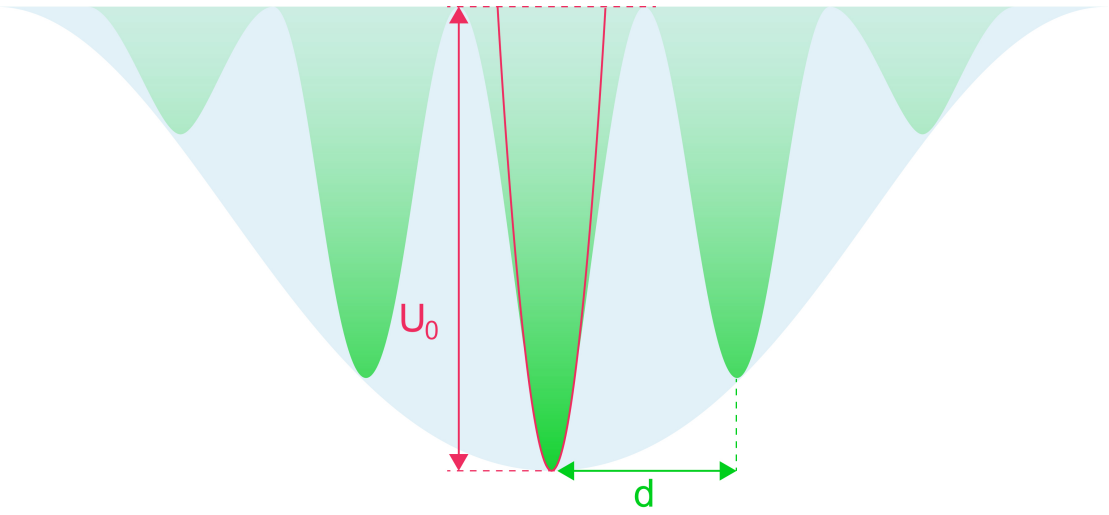

Figure 3.6: *Trapping potential of a red-detuned accordion lattice seen by atoms of along gravity. The Gaussian envelope dominating the intensity distribution is marked by the light blue area. The trapping potential in z-direction seen by the atoms is depicted by the light green area. The second-order polynomial fitted to find the trapping frequency for an individual fringe is marked in dark pink.*

The analytical expressions resulting from the approximation are given by

$$U_0 = -\frac{8\alpha P}{\pi w_{y0} w_{z0} c \epsilon_0} \tag{3.33}$$

$$\nu_x = \sqrt{\frac{16 P\alpha}{\pi m w_{y0} w_{z0} c \epsilon_0}\left[\frac{2\sin^2(\theta)}{w_{z0}^2} + \left(\frac{\lambda\cos(\theta)}{\pi}\right)^2\left(\frac{1}{w_{y0}} + \frac{1}{w_{z0}}\right)\right]} \tag{3.34}$$

$$\nu_y = \sqrt{\frac{32 P\alpha}{\pi m w_{y0} w_{z0} c \epsilon_0}} \tag{3.35}$$

$$\nu_z = \sqrt{\frac{16 P\alpha}{\pi m w_{y0} w_{z0} c \epsilon_0}\left[\frac{2\cos^2(\theta)}{w_{z0}^2} + \left(\frac{\lambda\sin(\theta)}{\pi}\right)^2\left(\frac{1}{w_{y0}} + \frac{1}{w_{z0}}\right) + \left(\frac{\pi}{d}\right)^2\right]} \tag{3.36}$$

Overall, it is useful to perform the strong trapping along gravity, defined by the z-axis.

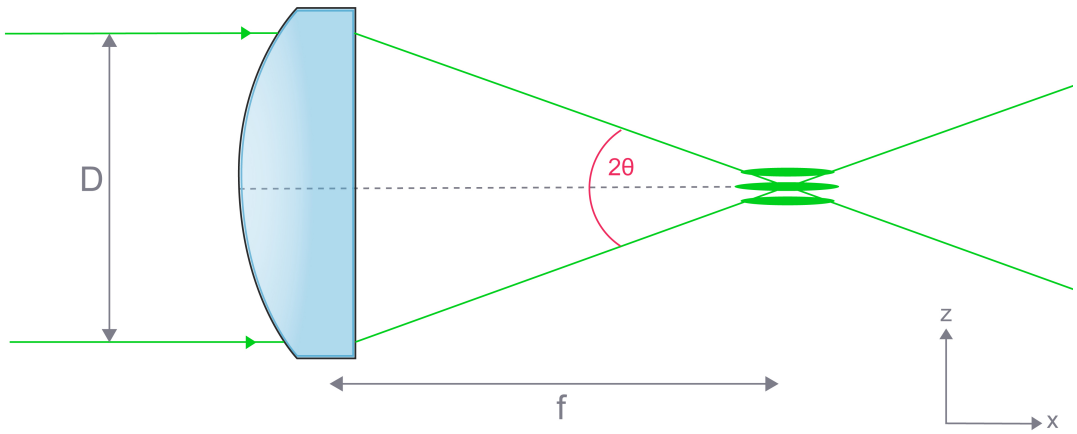

Figure 3.7: *Experimental realization of an optical accordion. A convex lens is implemented to focus two parallel beams that create the interference pattern.*

Experimentally, the interfering of the beams is achieved by focusing two parallel beams using a convex lens as depicted in figure 3.7. The angle is then determined by the distance between the parallel beams D and the focal length of the focusing lens f.

$$\theta = \operatorname{atan}\left(\frac{D}{2f}\right). \tag{3.37}$$

Consequently, the fringe distance can be approximated by

$$d = \frac{\lambda f}{D}. \tag{3.38}$$

Ideally, the position of the middle fringe should coincide with the center position of the Gaussian curve, and atoms should be loaded into the middle fringe, which has the highest intensity and therefore the deepest trapping potential. For alternative experimental applications, two or more fringes could be loaded simultaneously to observe interactions between the two quasi 2-dimensional atomic probes. In general, the position of the center peak can vary if the individual beams have a phase relative to each other. Consequently, the beams' phase should be stable in time, as to avoid spatial displacement of the trapping potential, which can cause significant heating and loss of atoms. Furthermore, the contrast between the nodes of the interfering pattern should be optimized, as to guarantee that the potential experienced by the atoms corresponds to the expected trapping potential. The contrast between the maxima and the minima of the interference pattern is affected by the individual polarization of the beams, the relative phase, and the relative power. Taking this factor into consideration, the individual beams were produced by the same laser source in [20], effectively reducing significantly experimental sources of instability. However, optical elements utilized to perform the **beam separation**, **the beam shaping**, and finally the **beam focusing** are also to be considered main contributors to any observed time- and space instabilities of the optical accordion.

The setup of an accordion lattice allows real-time tuning of the fringe distance by tuning the interfering angle. This additional advantage can be achieved by implementing a mechanical system that dynamically increases or decreases the beam distance D. In the case of [20], a mirror placed on a liner translation stage was responsible for the beam separation control. Once again, multiple instability sources should be considered at this point. The control over the trapping frequency is applicable for adiabatic compression of an atomic cloud with minimal atom loss, as long as high stability of the optical accordion is achieved.

3.4 Interference pattern calculations

Making use of the understanding gained by looking at the origin of the interference pattern, we can now proceed to choose parameters that fulfill the 2D conditions for our Dy probe. According to equation (3.2), for an atomic cloud at 50 nK, the vertical trapping should strongly surpass 1040 Hz. We aim to reach values around 15 kHz for the strong confinement while maintaining much weaker residual trapping below 100 Hz.

Vertical Trapping

In the case of our setup, the beam separation and the minimal focal length of the focusing lens, and consequently the half-angle θ, are limited by the dimensions of the chamber. The maximal beam separation at the view-port - which is at 101.3 mm from the chamber's center- can reach 32 mm, thus the maximal interference angle is given by

$$\theta_{\max} = \operatorname{atan}\left(\frac{D_{\max}}{2s_{\text{center}}}\right) = \operatorname{atan}\left(\frac{32}{2 \cdot 101.3}\right) = 8.976^{\circ}. \tag{3.39}$$

For the aimed strong trapping frequency (15 kHz), it can be assumed that an angle of at least 8.9° will be achieved experimentally.

According to (3.36), interference at larger angles provides a smaller fringe distance d, and thus a higher trapping frequency ν_z. In particular, in the limit $d \ll w_{y0}, w_{z0}$ the last term in the square root dominates and the expression for ν_z can be simplified to

$$\nu_z = \sqrt{\frac{16P}{\pi m w_{y0} w_{z0} c \epsilon_0} \cdot \left(\frac{\pi}{d}\right)^2}. \tag{3.40}$$

Furthermore, it is understood from equation (3.36) that smaller beam waists will provide higher trapping frequencies at the center of the trap, as the beam is more strongly focused. By carefully looking at the equations, it also becomes evident that this dependence is not directly on the individual values w_{y0} and w_{z0}, but rather on the geometric mean $\sqrt{w_{y0} w_{z0}}$. Accordingly, it results practical to define the so-called aspect ratio (AR) $w_{y0} : w_{z0}$. Overall, we opt to maintain a

rather small aspect ratio that does not surpass 10. A broad scan over different values of w_z and w_y, with $AR \leq 10$, for $\lambda = 532$nm and $\lambda = 1064$nm at typical laser power $P = 10$W, provides a better overview of the achievable trapping frequencies. The results of the numerical simulation show that vertical trapping frequencies well above 15 kHz can be achieved for $w_z \leq 60$ µm and $w_y \leq 600$ µm for both wavelength candidates at 8.9°. Nevertheless, we observe that to maintain both conditions, for vertical trapping as well as for residual trapping, the 532 nm laser offers better results. Therefore, it is decided to go ahead with this wavelength for the experimental implementation. The exact geometry of the beam will be chosen after the effect on the residual trapping is introduced in the next section.

In comparison to the maximal angle, the minimal interference angle we want to achieve is not motivated by the value of the trapping frequency but rather by the size of the fringes. Ideally, the atom cloud should be loaded entirely into a single fringe site, which means that the fringe dimensions should be comparable to those of the cloud. In our case, we aim for a maximal fringe size of 20 µm, which according to equation (3.30), corresponds to a half-angle $\theta_{\text{min}} = 0.76°$ for 532 nm, and to a minimal beam separation $D_{\text{min}} = 2.7$mm.

Residual Trapping in Plane

The geometry of the beams and the wavelength of the laser, which determine the fringe distance, play a crucial role to determine the trapping frequencies in all directions. At this point, the trapping frequencies in x and y and their ratio will be commented on in more depth.

Altogether, it cannot be assumed that the trapping in one direction is linked solely to the beam waist in the same direction. Rather, the specific combination of beam waist sizes yields the residual confinement in plane, as indicated in equations (3.34) to (3.36). According to scans over multiple combination possibilities of w_z and w_y, for a ratio $w_y : w_z = 6.4$, the resulting frequencies ν_x and ν_y are equal. Note that the scans were performed for the aforementioned parameters: $\theta = 8.9°$, $P = 10$W, and $\lambda = 532$nm. For equal trapping frequencies ν_x, ν_y the potential is symmetric, i.e circularly shaped. To achieve symmetry we would have to apply a strongly elliptical beam with an aspect ratio of 6.4, however, we consider that a slight asymmetry of the residual trapping could be compensated by other means. Therefore, we decide to limit the aspect ratio to 6. Figure 3.8 displays an example of three different geometries resulting

from different ratios $AR = 6.4, 3, 1$. Based on the simulation, it is decided that $w_z = 40 - 60\mu m$ $w_y = 240 - 260\mu m$, taking into account that $AR \leq 6$. A final consideration to reduce the range of the applicable beam waists is the ratio of the middle fringe and the side fringes at a maximal fringe size. In order to effectively load the atoms in the middle fringe, the trapping at the center should be significantly higher than on the side fringes. In general, we observe that a smaller beam waist w_z yields a larger fringe intensity ratio. Finally, we decide a good compromise is $w_z = 50\mu m$ and $w_y = 250\mu m$, with $AR = 5$.

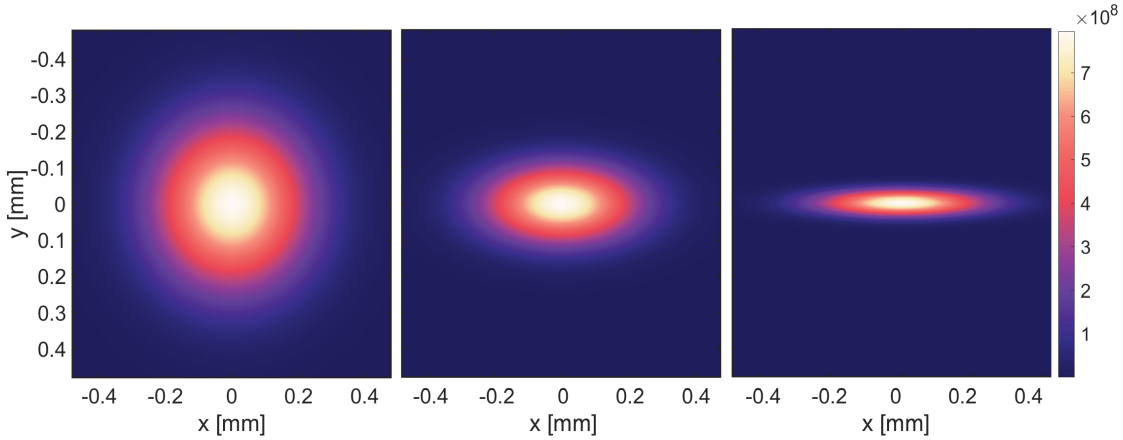

Figure 3.8: *Residual trapping of the atoms in plane.* ***left:*** *Symmetric trapping in plane resulting from beam geometry* $w_z = 50\mu m$ *and* $w_z = 320\mu m$, *i.e* $AR = 6.4$. ***center:*** *Cigar-shaped trap for* $w_z = 50\mu m$ *and* $w_z = 150\mu m$. *The trapping in y-direction is slightly above the desired trapping frequency at* 169 Hz. ***right:*** *Strongly elongated trap for* $w_z = 50\mu m$ *and* $w_z = 50\mu m$. *The trapping frequency along the y-axis is around* 880 Hz, *significantly surpassing the expected trapping frequency of* 100 Hz

3.4.1 Final Beam Properties

The final calculations for the desired trapping frequencies are performed with the parameters displayed in table 3.1. The experimental implementation described in chapter 4 will be based specifically on these values.

The resulting trapping frequencies, trap depth, and fringe distances for the maximal and minimal interference angle are summarized in table 3.2. The trap geometries for both cases are displayed in figure 3.9. The trapping potential in the x-z plane showcases the two incoming beams interfering at a shallow angle. The small fringes observed on the left, barely under 2 µm in size, reflect the high trapping frequency that provides the strong confinement needed to achieve a

Wavelength λ	**Power** P	**Polarizability** α	w_z	w_y	$\theta_{\mathbf{max}}$	$\theta_{\mathbf{min}}$
532 nm	10 W	350a.u	50 µm	250 µm	8.9°	0.76°

Table 3.1: *Final choice of parameters for the calculation of the interference pattern. It is decided to implement a high-power* 532 nm *laser, with an elliptical beam waist. The chosen beam waist ratio* $w_y : w_z = 5$ *is responsible for the slightly elongated shape of the trap in the residual trapping plane.*

quasi-2D regime. The larger dimensions of the fringes on the right (20 µm) will allow for the loading of atoms into one single fringe site.

Interference angle θ	**Trapping Frequencies** $\nu_z : \nu_x : \nu_y$	**Trap depth** U_0	**Fringe Size** d
$\theta_{\max} = 8.9°$	(25672 : 60.9 : 78.8) Hz	80.2 µK	1.7 µm
$\theta_{\min} = 0.76°$	(1478 : 3.4 : 79.65) Hz	80.2 µK	20 µm

Table 3.2: *Final calculation results for the desired accordion lattice for dysprosium atoms. The vertical trapping frequency for the maximal interference angle fulfills the requirements for quasi-2D trapping of the atoms. The fringe size for the minimal interference angle should allow for the clean loading of a single fringe. The ratio of the trapping frequencies on the residual plane* $\nu_y : \nu_x$ *for* θ_{max} *is roughly 1.3, reflecting the subtle cigar-shape geometry.*

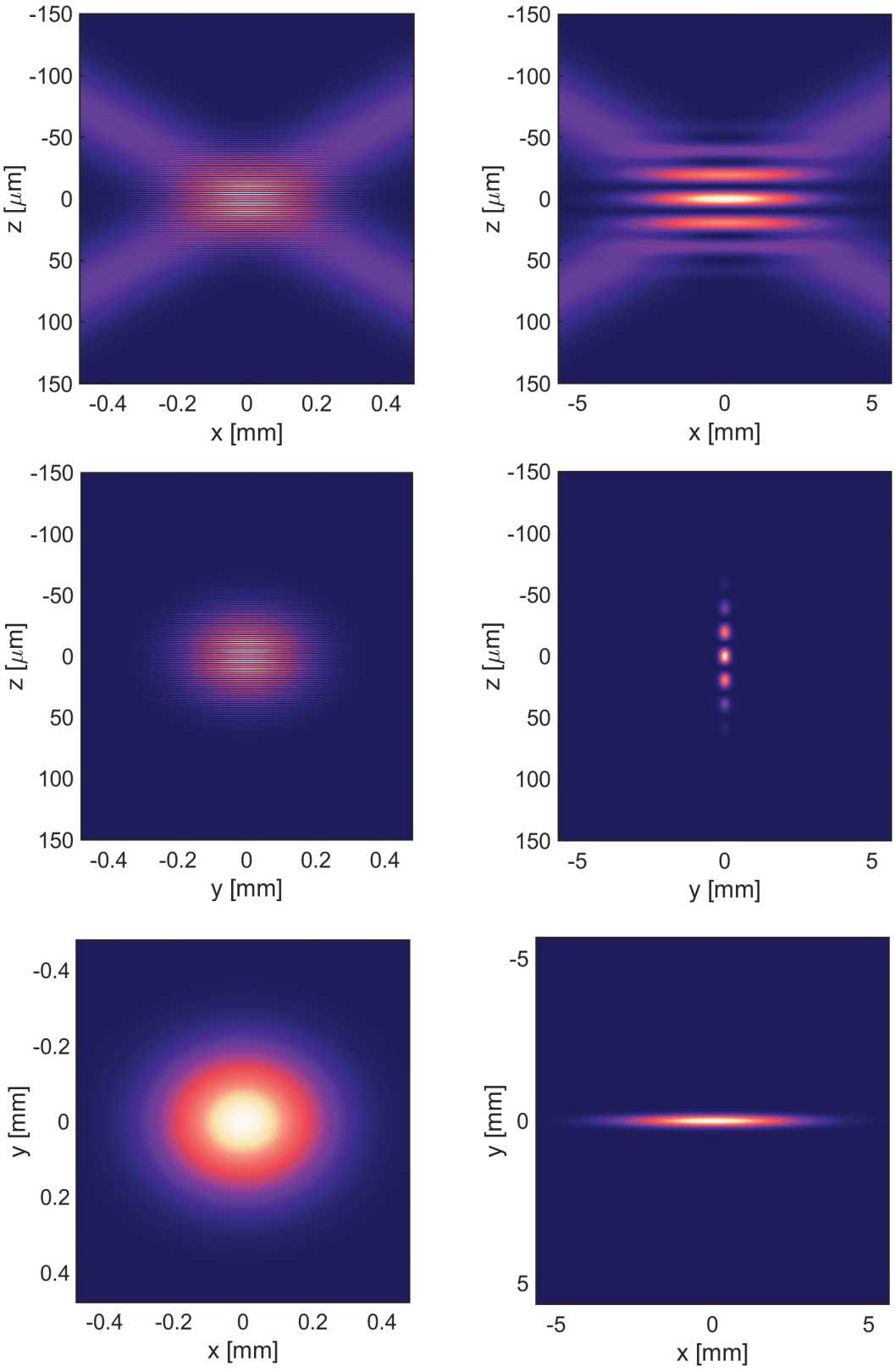

Figure 3.9: *Overview of the simulated trapping potentials for the expected maximal (right), and minimal (left) interference angles θ.*

Chapter 4

Experimental implementation

The following chapter will briefly summarize existing designs of optical accordions and the considerations and requirements for the accordion lattice for dysprosium atoms at the DyLab. Afterwards, the **optical design** based on these considerations and the parameters calculated in the previous chapter will be explained. Finally, the **opto-mechanical** solutions necessary to implement said optical design will be presented.

4.1 Accordion Lattices for Ultracold Quantum Gases

The convenient application of optical accordions to investigate ultracold atoms has promoted a large range of design variations that have been proposed to improve stability and control possibilities [21], [26], [27], [22]. Additionally, significant design variations are usually required to adapt the concept of the accordion lattice to each individual experimental setup and the trapping requirements for different atomic species, as well as the geometrical constraints of the apparatus. This section consists of a general overview of the different existing designs of an accordion lattice for ultracold atoms and considerations extracted for our design. The section will focus on two main points necessary for a successful design: separation of one laser beam into two parallel beams, and mechanical compression of the accordion lattice.

4.1.1 Beam separation

In the original paper [20] the method used to produce two nearly identical beams is to place two polarizing beam-splitters on top of each other, see figure 4.1. The single beam entering the first PBS is split into its s- and p-polarized components. The s-polarized beam is reflected away from the cube and towards a focusing lens. The second beam, corresponding to the p-polarized part, is transmitted through the first and second cube, and is then reflected by a mirror placed on top of the second PBS, passing two times through a quarter-wave plate. Finally, the second beam, now also s-polarized, is reflected by the second cube towards the focusing lens. This basic setup has been adapted to accommodate experiments with ultracold atoms, like in the case of Innsbruck (Er and Dy) [27], and Paris (Rb) [21].

Altogether, the principle of using polarizing beam splitters is common in many setups. However, in many cases, the second cube has been replaced by a mirror and the first cube has been flipped as seen in 4.1. In Hamburg this 1 PBS method has been implemented successfully for Lithium atoms [24]. In this setup, the reflected beam on the first - and only - cube is directed towards a back mirror and quarter-wave plate, and then is transmitted through the cube towards the focusing lens. On the other hand, the transmitted part reaches a second mirror placed at 45° on top of the cube and is reflected directly towards the focusing lens.

A third method that has been implemented at Harvard, is to separate the beam with a custom hexagonal beam-splitter, made of two dove prisms [23], as sketched on figure 4.1 along with the other two methods. Although all three methods seem similar, they represent significant variations for such a sensitive system as the optical accordion. Overall, the path difference between the beams should be minimized to avoid strong fluctuations of the beams with respect to each other. In the case of the 2 PBS method, the path difference is the longest, as one beam is directly send towards the lens, while the other has to travel through both PBS's and be reflected two times before heading towards the lens. In comparison, the axicon design provides the shortest path difference, as theoretically it should be equal to zero. Nonetheless, the axicon design is a single fixed mounted optical element, which means that any alignment precision is limited to the gluing procedure of the dove prisms. If the prisms are not perfectly parallel to each other, this can not be corrected later. Similarly, two PBS placed on top of each other may not lay perfectly parallel. In contrast, the 1 PBS

method introducing an additional mirror instead of the second PBS provides more control over the tilting and alignment of the two parallel beams produced by the setup. Therefore, for our design we have chosen to implement the 1 PBS setup with a few adaptations. The final design will be explained in the next section.

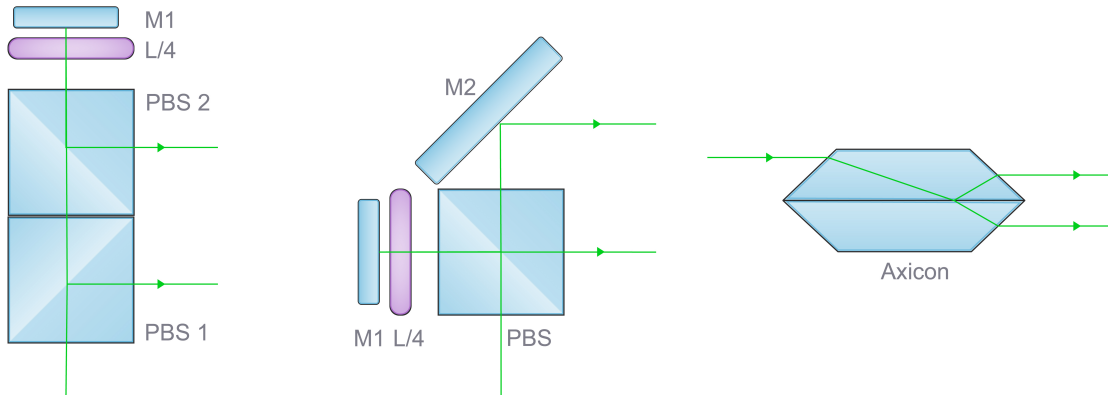

Figure 4.1: *Overview of the main beam splitting methods considered for our accordion lattice.* ***left:*** *The 2 PBS method uses two polarizing beam splitters, one mirror and a quarter-wave plate to produce the parallel beams. This setup causes the largest path difference between the beams out of the three designs.* ***center:*** *The 1 PBS method replaces the second beam splitter with a mirror mounted at* $45°$ *to shorten the path difference. Additionally, it provides more control over the alignment of the parallel beams.* ***right:*** *A customized axicon made of two dove prisms reduces the path difference the most. However, the fixed nature of the setup doesn't allow for corrections on the alignment once the prisms have been glued together. Adapted from [20], [27], [23]*

4.1.2 Mechanical compression and dynamic stability

Finally, we will consider the different possibilities to achieve the mechanical compression of the trap. Initially, it was proposed by Li et al [20]. to control the beam separation with a mirror mounted on a linear stage. Here, a smooth transition from $d = 0.81\,\mu m$ to $d = 11.2\,\mu m$ in $3\,s$ was achieved. The linear stage also showed relative dynamic stability, as it was observed that the central fringe shifted by less than $2.7\,\mu m$ along the vertical direction during the compression.

Alternatives to achieve a higher compression speed have been implemented: in [27] and [23] a rotational stage was used in combination with a specially designed periscope to control the beam spacing. This was done because commercial rotating stages usually achieve larger rotation velocities than commercial linear translation stages, which with the use of suitable mirror systems can

reach faster compression times. On the other hand, the use of Acousto-Optical-Deflectors (AOD) has also been considered, like in [26]. However, due to the large intensity loss caused by AODs, this was decided against. Considering that the compression of our optical accordion should happen in an adiabatic time scale, and after reviewing the offers for commercial linear stages, it has been decided to implement a simple linear translation stage for our first version of the accordion lattice for dysprosium. Further details about the chosen linear stage are given in the section about the mechanical design, where additional factors are taken into account. The vibration caused by the chosen linear stage will have to be accounted for and possible solutions to reduce the impact on the stability of the accordion will be presented later.

The following table summarizes some additional key points in the mentioned setups that are considered for the design of our accordion.

Reference	Beam Separation	Lattice spacing	Mechanical Compression	Time Scale
Li et al. [20]	2 PBS	0.96 - 11.2µm	Linear Stage	1s
Brandstetter [27] (Er / Dy)	2 PBS	2.66 - 22.2µm	Rotational Stage	0.1s
Saint-Jalm [22]/ Ville [21] (Rb)	2 PBS	1.2 - 11µm	Linear Stage	1s
Kerkmann [24] (Li)	1 PBS	2.1 - 45µm	Linear Stage	0.112 s
Hebert [23] (Er)	Axicon	2 - 20µm	Rotation Stage	0.015 s
Williams et al. [26]	1 PBS	1.8 - 18µm	AOD	0.1 s

Table 4.1: *Accordion lattice references for ultracold quantum gases. Implementations make use of different methods for the beam separation. The achieved ranges of lattice spacing tend to be in the same order of magnitude, and they overlap with the expected fringe distances for the DyLab. The adiabatic mechanical compression we expect has been proven to be achievable with motorized linear translation stages.*

4.2 Optical Design

In order to simplify the explanation of the design process, the following section will be divided into three main points :

- Beam focusing
- Beam separation
- Beam shaping

For each item, the selection process of the optical elements will be briefly discussed, and in the cases where customized design are necessary, the design process will be explained in detail. The design has been developed in reverse order with respect to the optical path, i.e starting from the focusing lens, as the main constrains arise from the science chamber and have to be worked on from there.

4.2.1 Beam focusing and crossing

The choice of the focusing lens applied to focus both beams to create the accordion directly impacts the stability of the central fringe during the compression procedure. This is because optical aberrations cause slight shifts of the real interfering point relative to the theoretical focus when the beams enter the surface of the lens at different places as shown in figure 4.2. An overall agreement is that a plano-convex lens doesn't provide the necessary stability for an accordion lattice. Following recommendations, we consider either an achromatic doublet lens or an aspherical lens.

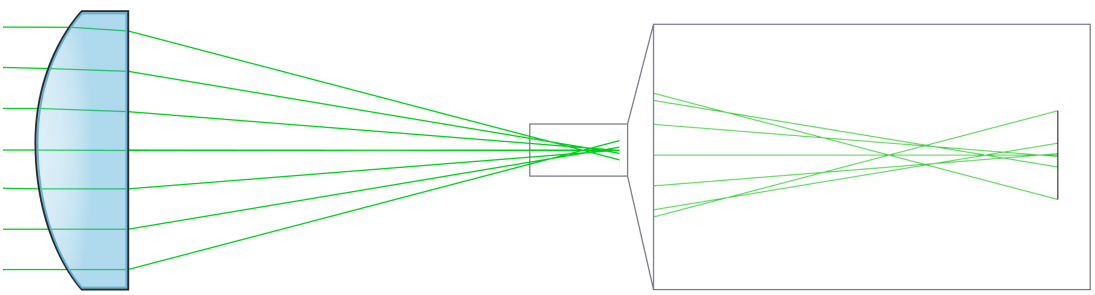

Figure 4.2: *Overview of performance of a standard plano-convex lens. The shift of the interfering point for parallel beams at different distances from each other will cause significant instabilities of the accordion lattice.*

Altogether, we decide to reduce all types of aberrations, especially spherical aberrations, by implementing a high-quality aspherical lens. The focusing lens used for the accordion lattice must also be suitable for high-power laser applications, therefore we opt for fused silica or similar material. Furthermore, the focal length of the lens should be larger than the distance between the viewport and the center of the science chamber. A convenient choice is found to be 150 mm. Now, since the lens is not going to be placed directly at the viewport, the diameter must be adapted to take advantage of the entire aperture of the chamber's window. At a distance of roughly 150 mm, the clear aperture of the lens should be at least 52 mm to achieve an interference half-angle $\theta = 8.9°$. The final requirements for the high-precision lens are summarized in table 4.2.

Effective Focal Length	Clear Aperture	Substrate	Coating Specifications	Surface Quality	RMSi
150 mm	$\leq$52 mm	Fused Silica	AR-Coating 532 nm R_{avg} <0.2%	10-5	<100 nm

Table 4.2: *Requirements for a high-quality aspherical lens to be implemented in the accordion lattice setup in the DyLab.*

Unfortunately, no commercial options that fulfill all specifications were available. However, the lack of commercial options opened the possibility to design the surface of the lens given by the aspherical equation specifically for our setup. The customized option was designed on Zemax and sent to be manufactured by *Trionplas* in Germany. Due to production possibilities that were discussed with different companies, we limited the order of corrections in the aspherical equation while optimizing the lens design. Additionally, we considered the thickness and diameter of raw material available, the thickness of the window and the vacuum of the science chamber. The overview of the final design is summarized in table 4.3.

Radius	Conic Constant	2nd-order	4th-order	6th-order
69.106 mm	-0.562	0	-2.700×10^{-9}	-1.793×10^{-12}

Table 4.3: *Final design of the customized high-precision aspherical lens. The radius is optimized for achieving an effective focal length (EFL) of* 150 mm *at* 532 nm*. The aspherical design was limited to the 6th-order correction term due to manufacturing possibilities.*

The expected wavefront error of the final lens was analyzed for an aperture of 1 mm and compared to a commercially available aspherical lens from *Edmund Optics* that most resembles our own design but that is unfortunately only available in N-BK7 and therefore not suitable for our high-power application. Due to the aforementioned custom production, the delivery of the lens was not achieved on time to perform the first test measurements. On that account, the aspherical lens from Edmund optics was used for the first setup of the accordion lattice. Accordingly, the test setup is a probe with a low-power laser.

Detailed information about the aberrations dominating the wavefront error can be gained from taking a look at the Zernike polynomial coefficients of the wavefront resulting from the Zemax analysis. The Zernike polynomials are a complete sequence of polynomials orthogonal to the unit disk described in polar coordinates. The so-called fringe convention yields 36 coefficients that directly represent classical aberrations such as spherical, tilt, coma, astigmatism, and defocus. For our custom lens analysis, we find that only coefficients 9, 16, 25, and 36 are non-zero. These all correspond to spherical aberrations of different orders as shown in table 4.2.1.

Zernike Fringe Coefficient	Aberration	Value
9	3rd-order spherical	0.00095768
16	4th-order spherical	0.0008764
25	5th-order spherical	0.00059867
36	6th-order spherical	0.00000728

Table 4.4: *Zernike fringe coefficients for the customized lens design. The only non-zero values correspond to spherical aberrations of higher orders.*

4.2.2 Beam separation

The design chosen for the beam separation and its control setup affects the achievable fringe distance, the time scale of the compression, the phase and polarization stability, and therefore the contrast between the interference pattern minima and maxima. In the first instance, we consider purely the optical design, i.e the optical elements.

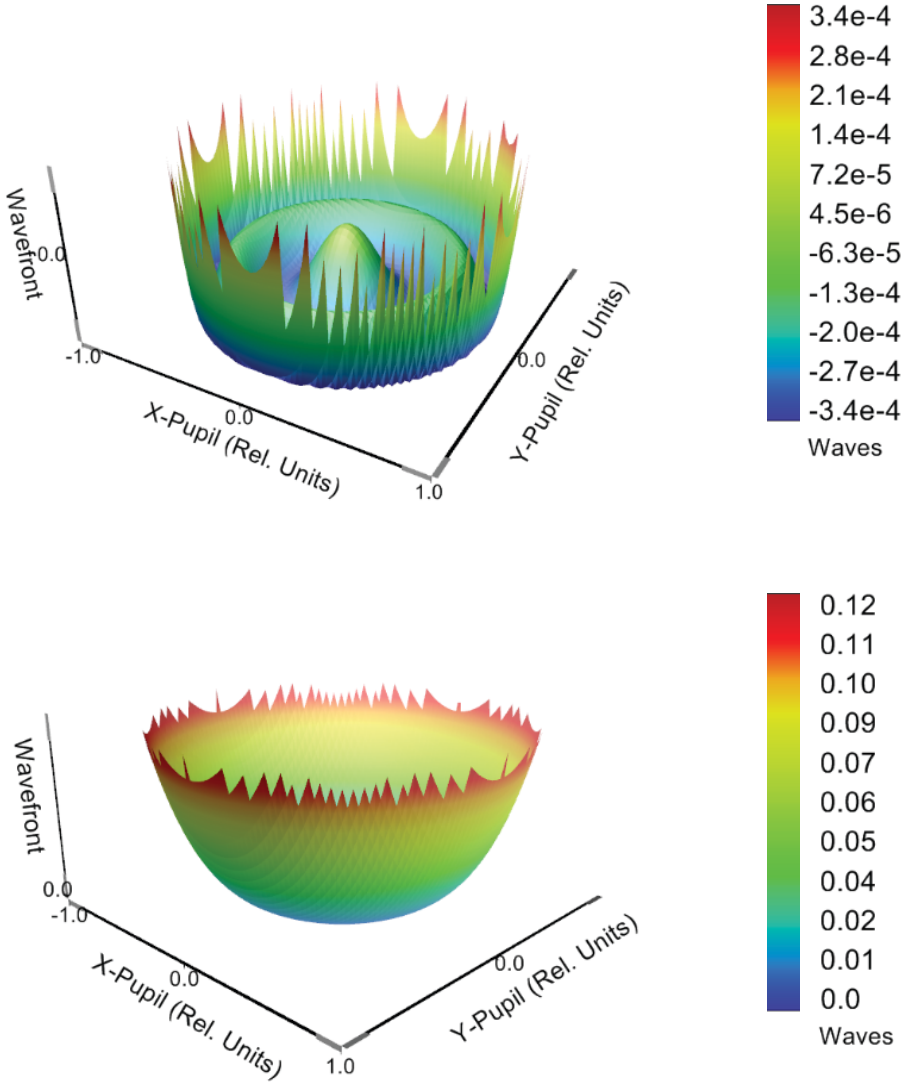

Figure 4.3: *Wavefront error analysis of the final lens design for an aperture of* 52 mm. ***top:*** *Wavefront error of the aspherical surface for our final design of the focusing lens.* ***bottom:*** *Wavefront error of a commercially available aspherical lens implemented for the first setup of the accordion. The performance of our design is expected to be better than the one of the stock lens used in the test setup.*

To minimize the path difference between the parallel beams without giving up control over the degrees of freedom of the elements, we have chosen the 1 PBS + Mirror method for the separation of the beam. The necessary optical elements include a **PBS**, a **mirror** mounted at 45°, a **quarter-wave** plate, and a **back mirror**. To reach the maximal interference angle $\theta = 8.9°$, the PBS and the 45° mirror must be at least half as high as the clear aperture of the focusing lens, i.e 26 mm. Since the desired height is slightly above the standard 1 inch for such optical elements, we decided to order custom-sized elements from

Lens-Optics in Germany. A sketch of the beam separation setup displaying the elements' dimensions is shown in figure 4.4. The customization furthermore allowed us to better fulfill the quality requirements for our setup. Some of the relevant specifications for the final elements responsible for the beam separation are summarized in table 4.5. Similarly to the lens choice, these optical elements responsible for the beam separation are required to be very high-quality to minimize any kind of aberrations and loss of power. Special attention is paid to the quality of the edges so that the beams will not be cut-off or deformed for the cases of maximal and minimal beam separation.

Description	Clear Aperture	Surface Quality	Coating
Optically-contacted PBS	90% / 27 mm	20-10	AR-Coating 532 nm R_{avg} <0.25%
Right-Angle Mirror	-	20-10	Dielectric Coating HR 532 nm / 45° R_{avg} >99.9%
Air-spaced Zero-order Quarter-Wave Plate	30 mm	20-10	AR-Coating 532 nm R_{avg} <0.25%

Table 4.5: *Quality requirements for the optical elements responsible for the beam separation.*

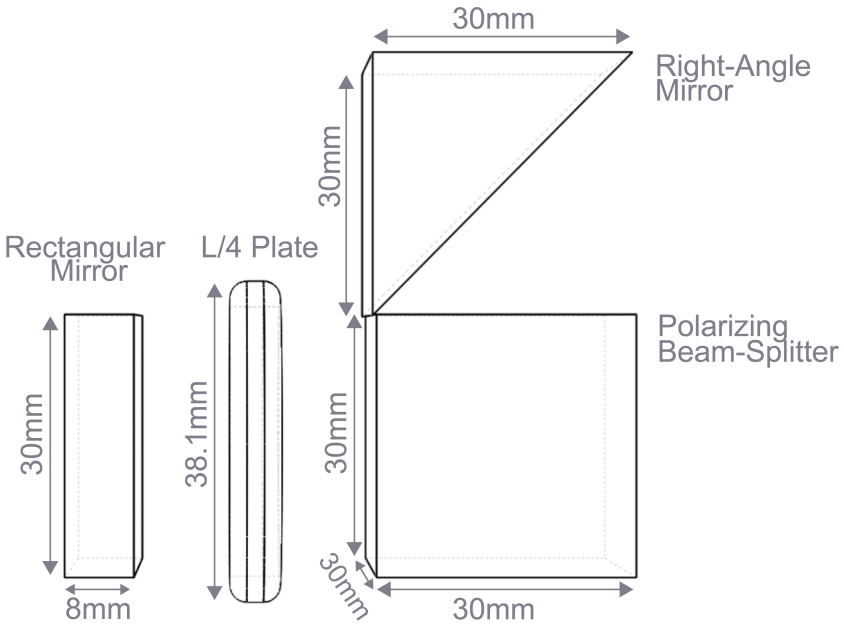

Figure 4.4: *Overview of elements' dimensions for the beam separation setup.*

4.2.3 Beam shaping

The expected beam characteristics discussed in the previous chapter can be experimentally realized by implementing a telescope setup before the focusing lens. The high-power laser planned for the real setup is a Continuous Wave Green Single-Frequency Fiber Laser with a maximum output power of 20 W and an estimated output beam size 0.9 mm $\times$ 0.9 mm. The laser output will be fiber-coupled as in the test setup using polarization-maintaining (PM) fiber and adequate outcoupler lenses. By these means, we can achieve an output beam size of roughly 1 mm. In the following, we will discuss the designing of the telescope setup for a collimated, theoretical output beam size of 1 mm, i.e a beam waist of 500 µm.

Due to the fact that the desired beam shape is elliptical, it is necessary to employ cylindrical lenses. First, we consider the expected final beam waist in z-direction $w_z = 50\mu m$. The beam waist of a beam after focusing can be computed by

$$w_0' = f\theta = f\frac{\lambda}{\pi w_0} \tag{4.1}$$

where θ is the divergence of the beam, f the focal length of the focusing lens, and w_0 the beam waist of the incoming beam. For an incoming beam with $w_0 = 500\mu m$ and a focusing lens with $f = 150mm$, the resulting beam waist is $w_0' = 50.8\mu m$, which is almost identical to the value we want to achieve. Therefore, in the z-direction we do not need to implement additional telescope lenses.

Furthermore, we again apply equation (4.1) to find out the beam waist of an incoming beam, which focused by our aspherical lens will yield a beam size of w_y =250 µm. The result is a beam waist of 101.6 µm. In general, a broad combination of cylindrical lenses can be convenient to produce this beam. However, we take into account, that the combination of the telescope lenses and the focusing lens, must be suitable for the long path that the beam will travel. This rules out lenses with very short focal lengths. Finally, we choose two cylindrical lenses with $f_1 = 200mm$ and $f_1 = 150mm$, which we plan to place at a distance of 442 mm of each other. The final setup for the beam shaping can be observed in figure 4.5.

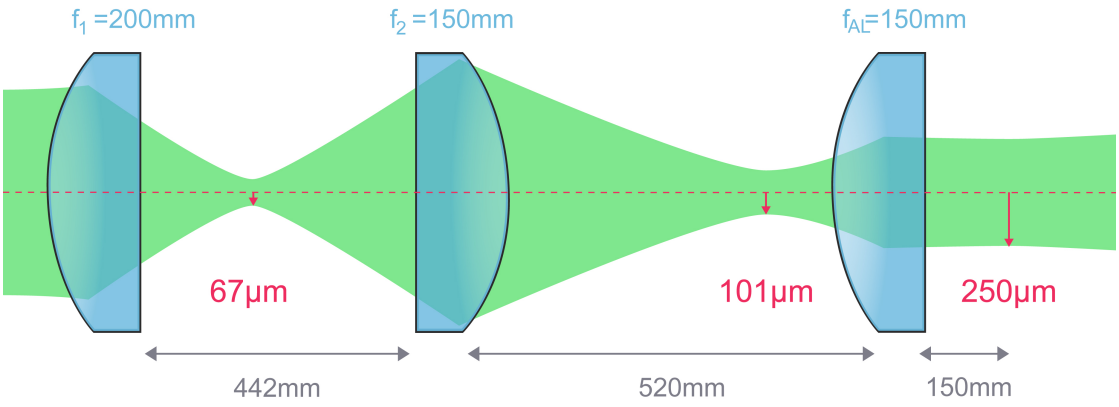

Figure 4.5: *Beam shaping setup for* $w_y = 250\mu m$. *Two cylindrical lenses with* $f_1 = 200mm$ *and* $f_2 = 150mm$ *are placed at* $442\,mm$ *from each other before the aspherical lens with* $f_{AL} = 150mm$ *to produced the desired beam waist.*

4.3 Opto-mechanical Design

After having decided on the optical elements that will be implemented to realize the accordion lattice experimentally, we now focus on suitable mechanical options to mount them, and on the mechanical system to achieve the compression of the lattice. During this design process, the priorities are the stability of the system, the implementation of only enough degrees of freedom for alignment, and maintaining the compact nature of the whole experimental setup. In the first part of this section, the design of the mounts for all optics will be briefly described, emphasizing the design process of a vertical structure where the elements responsible for the beam separation will be mounted, the so-called **tower mount**. In the end, the choice for the linear translation stage will be introduced.

4.3.1 Aspherical Lens Holder

The aspherical lens ordered for our setup provides a large enough clear aperture ($\approx 54\,mm$) to achieve the maximal beam separation ($52\,mm$) and thus the maximal interference half-angle ($8.9°$). However, the extension of the lens in the y-z plane blocks the whole optical access to the viewport, which limits further applications that could be introduced in the future. Therefore, we have decided to cut the lens around the center to have a thin rectangular shape with $15\,mm \times 60\,mm$. Accordingly, we design a simple holder for the lens that suits these dimensions and that secures the lens properly with two screws. Figure 4.6 provides an overview of the cut and the holder.

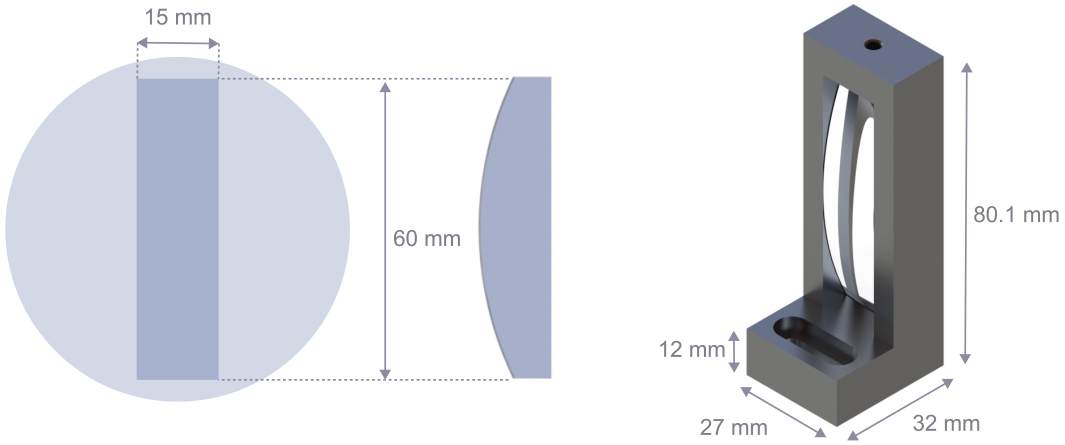

Figure 4.6: *Cut and mounting of the custom lens. To avoid the lens from blocking the complete optical access in one direction, we decide to cut a rectangle around the center of the lens. Accordingly, a custom holder is designed to hold the rectangular version of the aspherical lens.*

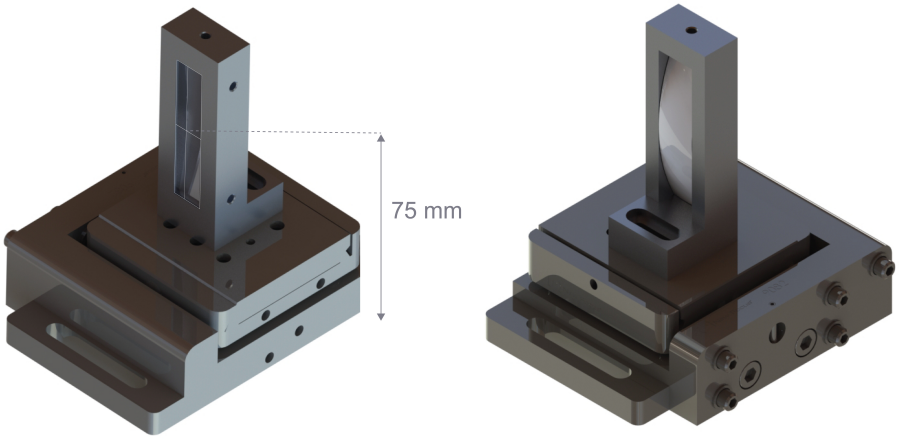

Figure 4.7: *Overview of the lens holder on the 5-Axis mount. The combined height of the 5-axis stage and the holder ensure that the center of the lens is at* 75 mm *from the breadboard.*

As stated before, the alignment of the lens, i.e the stability of the interference point of the beams at different separations, is crucial for the stability of the accordion. We conclude that at least 5 degrees of freedom will be necessary: translation along y and z, as well as tilt around these axes, will be used to align the parallel beams to the lens and guarantee that they enter the surface orthogonal to the optical axis, while translation along the x-direction will be necessary to accurately place the optical accordion at the position of the atoms in the science chamber. Finally, we decide to order a 5-axis mount from *Newport*. Due to the fact that the center of the science chamber lies 75 mm over the breadboard,

the combined height of the holder and the mount must ensure that the center of the lens is also perfectly positioned at this height. Figure 4.7 shows the final design of the mounted lens on the 5-axis mount.

4.3.2 Tower Mount

The following part will focus on the mounts and holders designed for the optical elements for the beam separation, namely the PBS, the right-angle mirror, the quarter-plate, and the back-mirror. All of these elements will be mounted inside of a robust vertical structure made of aluminum, shown in figure 4.8, called the tower. At first, the mounting requirements for each individual component will be described to explain the internal structure of the tower mount. At the end, an overview of the final design of the fully mounted tower setup will be presented.

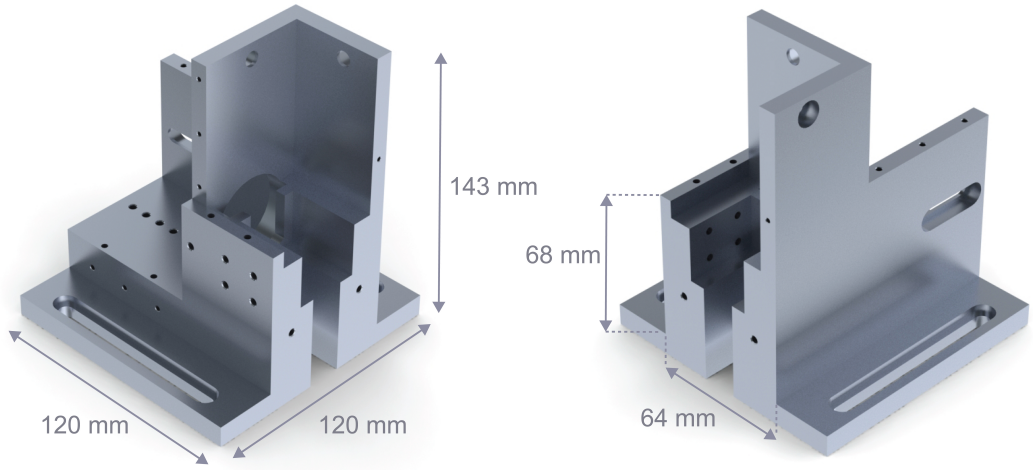

Figure 4.8: *Overview of the tower mount. All optical components for the beam separation are mounted inside a robust aluminum structure.*

Polarizing Beam Splitter

One of the key considerations for the design of the vertical mount is the placement and securing of the polarizing beam splitter. Due to the fact that the optical setup for the beam separation implements two mirrors that can be used for

the alignment of the parallel beams, we conclude that the PBS does not need to have any degrees of freedom, as the alignment can be performed with respect to it. The cube will be fixed in space and the tower must only provide passive orthogonal alignment along gravity. Furthermore, we consider the fact that four surfaces of the cube are going to be needed for the realization of the parallel beams, including the bottom surface. Therefore, the cube must be mounted on a platform which provides at least partial optical access from the bottom. A high degree of parallelism to the ground can be achieved by fine polishing the surface of the flat platform. An additional consideration for the design of the mount, is the optical height of the main experimental setup which must align with the upper surface of the cube. The center of the chamber is at 75 mm over the bread board , meaning that the 30 mm PBS has to be elevated by 45 mm. The placement of the cube inside the tower can be observed on the left in figure 4.9. For stability, the PBS is fixed by three M2 screws from one side

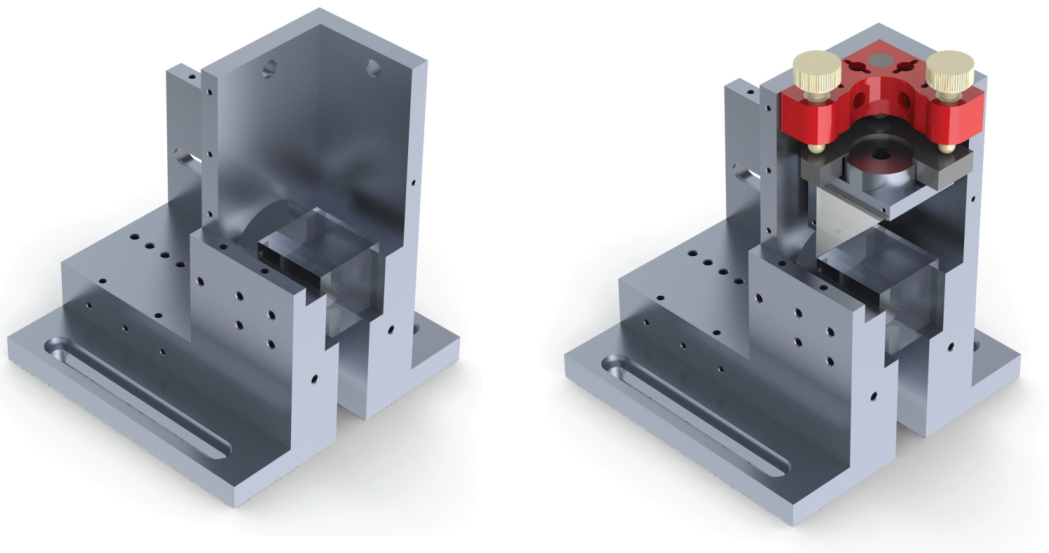

Figure 4.9: *Polarizing beam splitter and right-angle mirror mounted inside the tower.* ***left:*** *The PBS is mounted at the lower part of the tower at* 45 mm *from the breadboard and secured by three M4 screws. The aperture on the bottom provides access to the vertical incoming beam. Fine polishing of the flat surface ensures that the cube is parallel to the ground.* ***right:*** *The right-angle mirror inside the custom holder is mounted on top of the cube by securing the commercial mirror mount on two sides to the tower.*

Right-Angle Mirror

Due to the custom size and shape of the right-angle mirror, no commercial mount can be used directly. However, a special holder with an adapter was designed and a standard commercial 1 inch mirror mount available at *Radian Dyes* was implemented. The design of the right-angle mirror holder attached to the commercial mirror mount and a picture of the finalized product can be seen in figure 4.10.

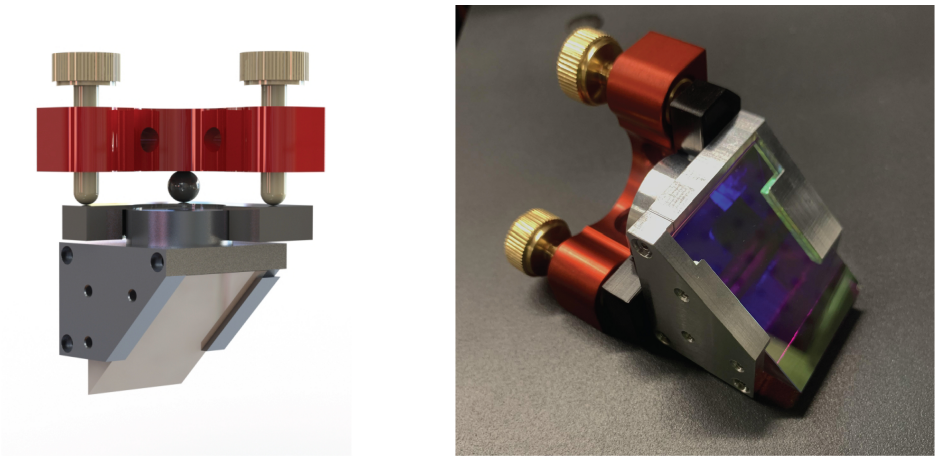

Figure 4.10: *Right-angle mirror holder on commercial 1 inch mirror mount.* ***left:*** *Final design of the RAM holder with a special adapter to be attached to a commercial mirror mount with two tilt degrees of freedom.* ***right:*** *The finalized product was produced in-house by the mechanical workshop. The custom RAM can be secured inside the holder by three M2 screws going through the cap of the holder.*

The chosen mirror mount provides two tilt degrees of freedom, which are necessary for the final alignment of the parallel beams. The right-angle mirror is to be mounted on top of the PBS, therefore the top of the tower mount is design to fit the standard 1 inch mirror mount. The mount is fixed with M4 screws on two sides to the tower to guarantee stability as shown in figure 4.9.

Quarter-Wave Plate

In order to reduce the optical path difference between the beams, we aim to place the PBS, the quarter-wave plate, and the back mirror as close to each other as possible. Accordingly, the quarter-wave plate is mounted on an aperture right behind the cube. The implementation of a special holder which resembles common rotational mounts allows for manual rotation of the wave plate inside the tower. The air-mounted wave plate is fixed inside the holder with a metal

ring. One side of the holder fits inside the aperture on the tower, while the other side of the holder slightly extrudes from the tower to allow alignment of the wave plate's axes. A screw on the outside can be tightened to secure the holder once the plate is in its final position.

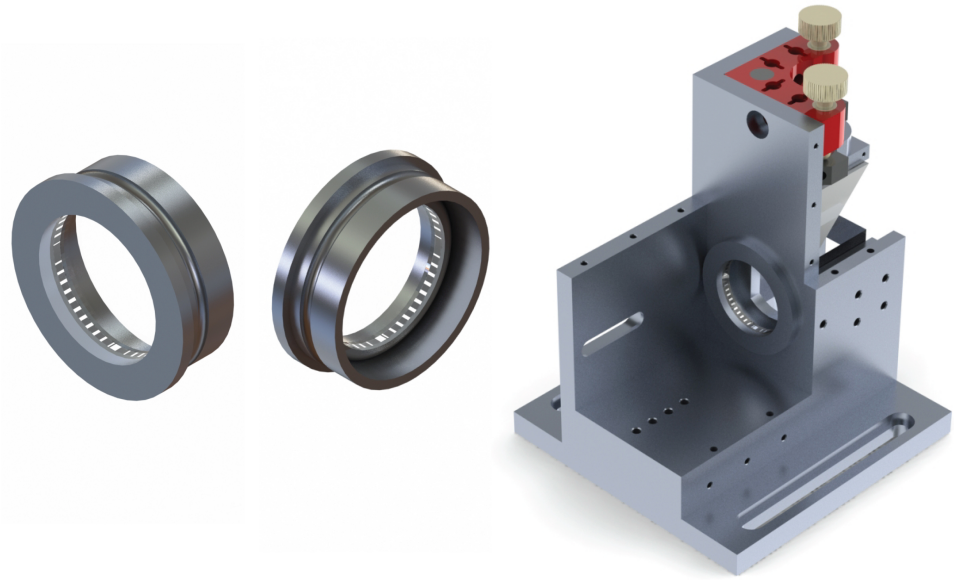

Figure 4.11: *Custom holder for quarter-wave plate.* ***left:*** *Design of the holder for the quarter-wave plate. The holder allows for a seamless manual rotation of the plate to its final position.* ***right:*** *Mounting of the holder inside of the tower. The aperture for the plate is designed to be as close as possible to the PBS. The holder can be secured in place by a screw on the side of the tower.*

Back-Mirror

Similarly to the quarter-wave plate, the back mirror should be placed as close as possible to the PBS to shorten the optical path. However, any path difference in the order of the laser's wavelength (532 nm) will cause a phase difference of the beams, affecting the contrast and stability of the accordion lattice. Therefore, the back-mirror must be attached to a piezo-ring that allows control of the path difference in the range of a few nanometers. To avoid any mechanical noise from the translation caused by the piezo during measurements, we implement an additional adapter based on the design by Magnan et al. [28]. The asymmetry and large mass of the adapter, see figure 4.12, should help drive the mechanical noise to a high enough frequency that it doesn't affect the optical accordion. In an effort to find the best option for our implementation, we design and manufacture

two different-sized adapters that will be probed together with the piezo-ring. The piezo will be glued between the small end of the adapter and the back-side of the back-mirror. Additionally, the piezo adapter can be attached to a commercial *Radiant-Dyes* mirror mount, similarly to the RAM holder. To allow for different adapters' sizes we drill four holes in the back of the tower mount, where the mirror mount will be secured. On the side of the tower, an elongated tap hole for the second screw to attach the mirror mount is drilled.

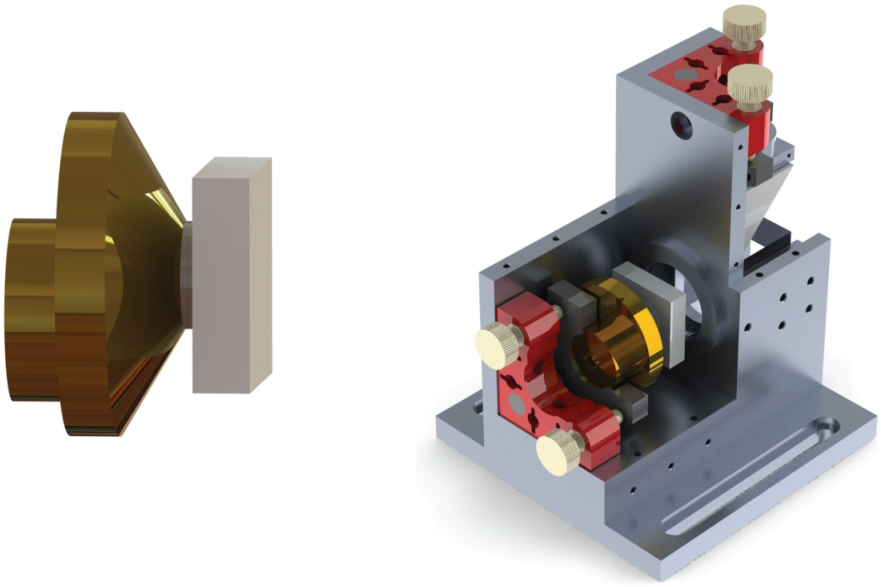

Figure 4.12: *Overview of the adapter for the back-mirror.* ***left:*** *Example of one of the designed adapters attached to a small piezo ring and the rectangular back-mirror.* ***right:*** *Mounting of the back-mirror inside the tower with a commercial mirror mount.*

It is important to mention that the final design of the adapter and the piezo control are not implemented in the time frame of this work. The test results in chapter 5 are acquired by mounting a simple 1-inch mirror on the back of the tower, therefore limiting the minimal beam distance that can be achieved.

Final Design

The described holders and the tower mount are polished and anodized before being installed in the test setup. Additionally, a series of plates are designed to cover the tower and avoid any damage to the optics. The side view of the final tower and the covered version are shown in figure 4.13.

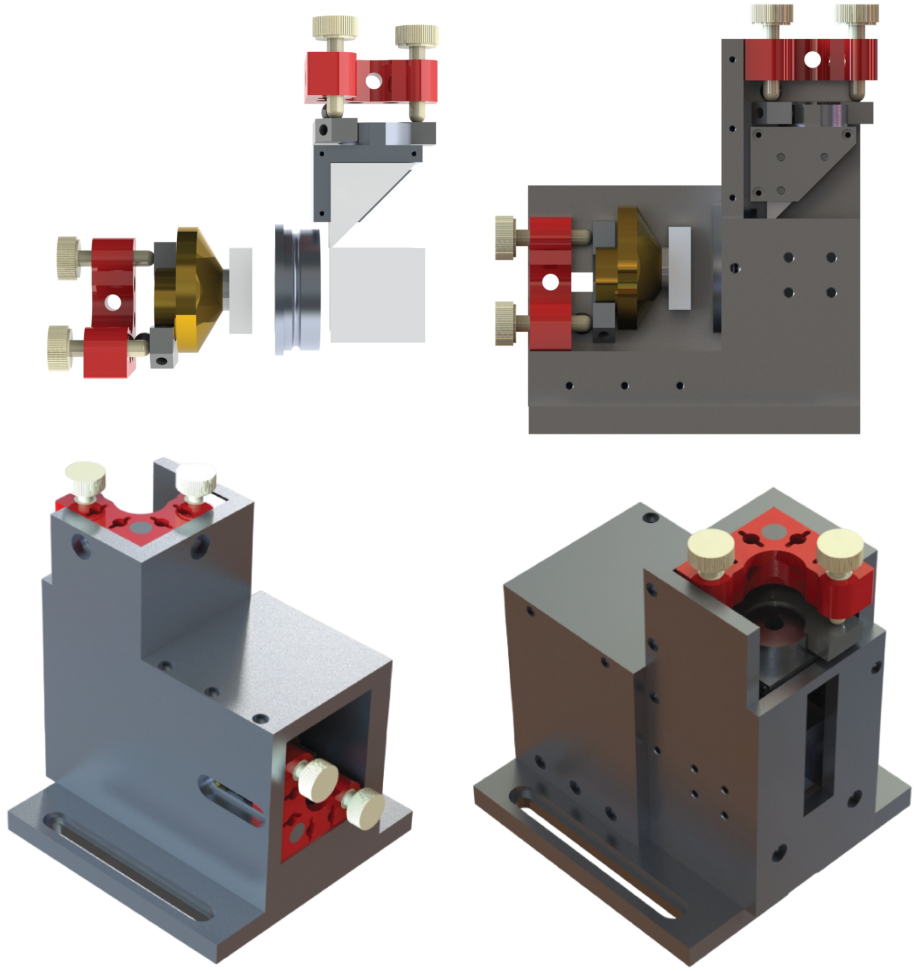

Figure 4.13: *Final design of the tower mount.* ***top left:*** *Side view of the beam separation setup and the custom mounts/ holders for each element.* ***top right:*** *Side view of the fully mounted uncovered tower.****bottom*** *View of the covered tower from two different angles.*

4.3.3 Linear translation Stage

The linear stage chosen for the accordion lattice has to be non-magnetic, so as to not affect the dysprosium atoms with its magnetic field. Additionally, it must have a travel range $\geq$26 mm and a speed $\geq$300 mm/s to achieve a compression time below 0.1 s.

A good option was found to be the **V-408 PIMag** Linear stage from *Physik Instrumente* with a travel range of 50 mm and a velocity of 700 mm/s. The maximal translation speed will allow a minimal compression time of approximately

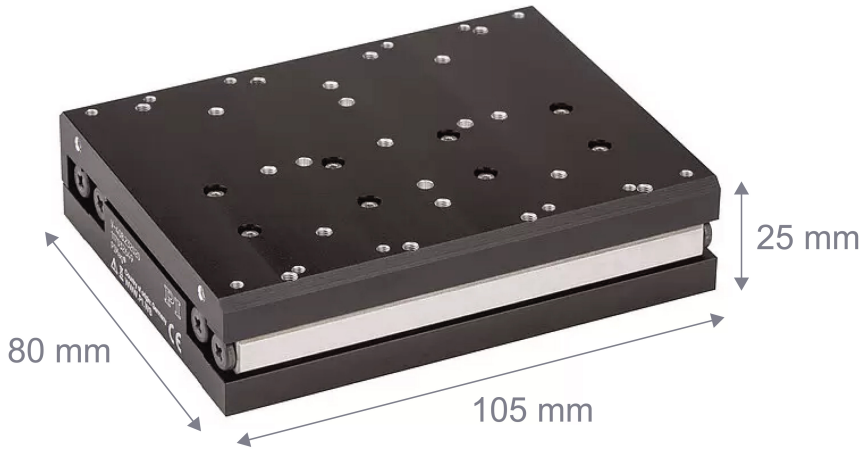

Figure 4.14: *Linear stage for adiabatic compression of the accordion lattice. The maximal translation velocity will allow for compression from the smallest interference angle* $\theta = 0.76°$ *to the largest* $\theta = 0.89°$ *in approximately* 40 ms.

0.04 s. This time scale is still considered adiabatic with respect to the trapping frequencies summarized in table 3.2. This linear stage is made of black anodized aluminum instead of steel which is more common for similar applications but which is unfortunately magnetic. Our application further requires highly precise bidirectionality repeatability in order to ensure that the beam separation remains within the expected values, and so the whole clear aperture of the viewport's window is utilized properly. The chosen stage offers a precision of roughly 0.1 µm. Once the linear stage is implemented, a right-angle mirror with the reflective surface at 45° will be mounted on top of the linear stage to translate the horizontal displacement into the vertical displacement responsible for the control of the beam separation.

Chapter 5

Experimental Characterization

The main goal of this chapter is to determine the stability of the interference pattern, especially of the middle fringe, at the focal point of the aspherical lens and in dependence on the linear stage translation. The alignment procedure and the final deviations from the ideal accordion are thoroughly analyzed to determine the optimal alignment sequence to be followed once the accordion setup is finalized and ready to be mounted around the main chamber. This performance analysis will also help define any improvements that may have to be implemented in the future.

The first setup for the Accordion lattice is probed with a 532 nm laser diode at low power. Some of the custom-designed optics could not be implemented in the time frame of this work, therefore temporary solutions that differ from the design described in Chapter 4.2 are used. The characterization described in this chapter is limited by the test elements.

5.1 Test Setup

The test setup is divided into two main parts, the lower setup, and the upper setup. On the lower optical table, we have placed the beam source and the optical elements responsible for the beam shaping and collimation. Afterwards, the beam is redirected to a breadboard mounted 275 mm over the optical table, where the upper setup has been mounted. The designed tower mount, responsible for the creation of two parallel beams, as well as the focusing aspherical lens and the imaging system are part of the upper setup. The propagation direction of the beam defines the x-axis and the vertical direction is the z-axis.

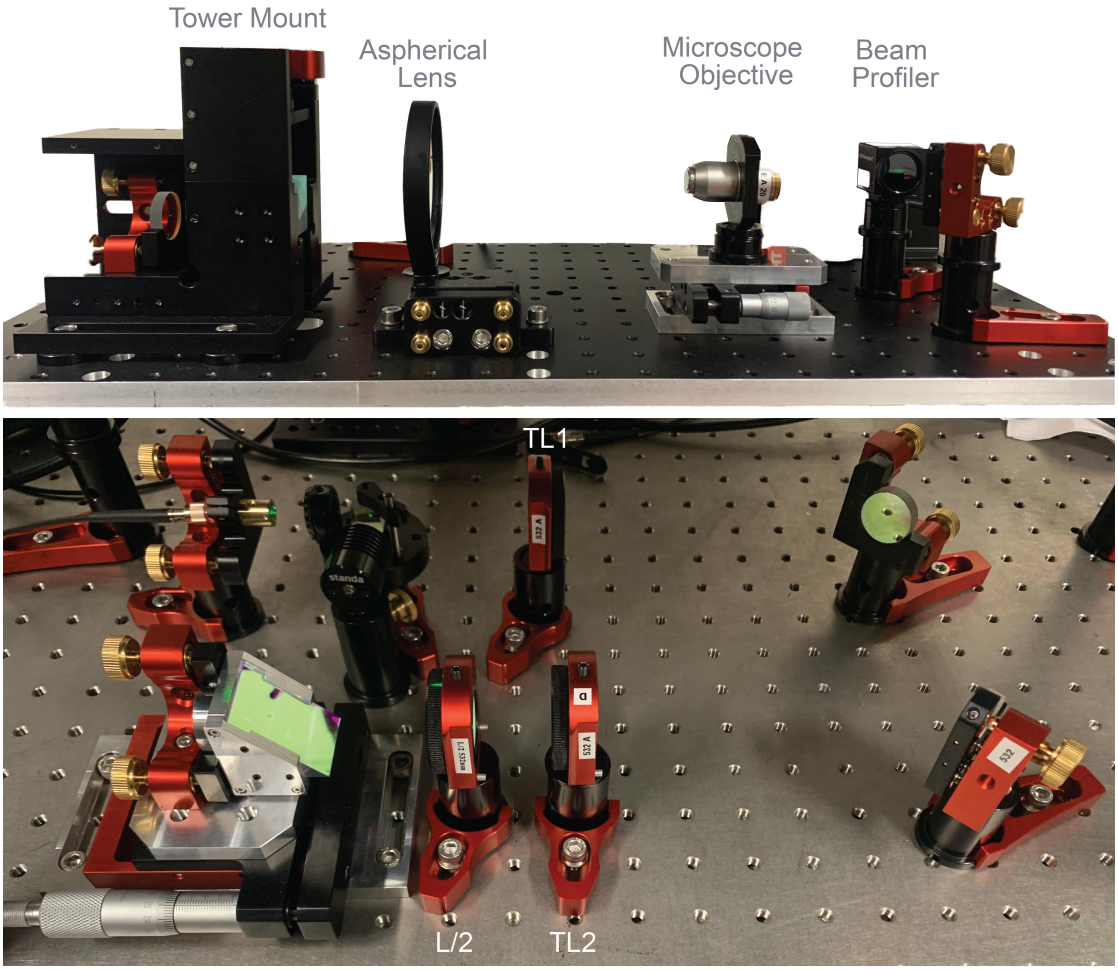

Figure 5.1: *Overview of the first test setup of an accordion lattice for dysprosium atoms.* ***bottom:*** *Lower setup responsible for beam shaping, contrast control and accordion compression.* ***top:*** *Upper setup responsible for beam separation, focusing and imaging.*

Lower Setup

The beam source available for the test measurements is a CW532-005 Compact size fix collimated diode pumped solid state Nd:YVO4+KTP laser-module from Roithner LaserTechnik, which produces a beam with a maximum power of 4 mW at a wavelength of 532 nm. The output is coupled to a Schäfter-Kirchhoff high-power, polarizing maintaining fiber. The numerical aperture of the fiber is 0.066 at 532 nm and the Mode Field Diameter (MFD) equals to 5.1 µm. A theoretical beam radius of 521.05 µm can be achieved by an outcoupler lens with a focal length of 8 mm.

Directly after the outcoupler, the polarization of the beam is cleaned by a one-inch half-wave plate and a PBS. The half-wave plate is used to do the PM alignment of the fiber. After the PBS, two cylindrical lenses for the telescope ($f_1 = 200$mm and $f_2 = 150$mm) are placed with a distance of $442(2)$ mm from each other. In between the telescope, two one-inch mirrors are placed to maintain the beam path within the dimensions of the breadboard. Right behind the second lens of the telescope, a one-inch half-wave plate is placed to control the polarization of the beam, which will later determine the intensity ratio of the two parallel beams produced at the tower. The last element in the lower breadboard, the Right-Angle Mirror (RAM1) that is responsible for redirecting the beam upwards, is mounted on a linear stage with a travel range of 25 mm.

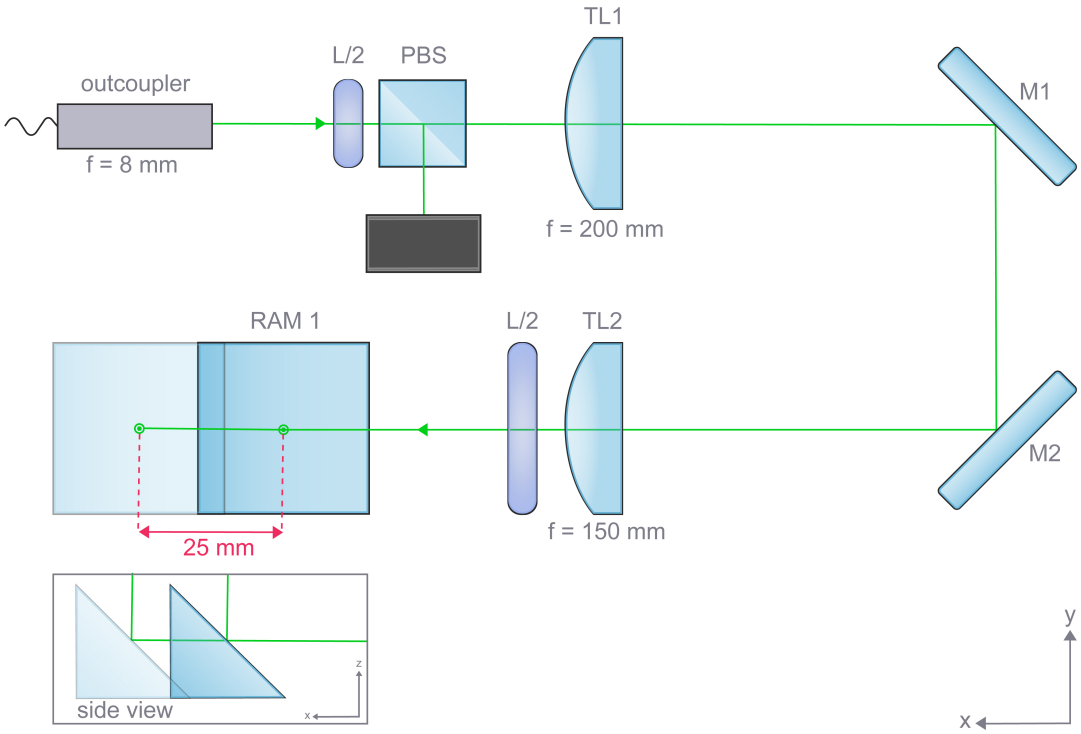

Figure 5.2: *Optical path on the* ***lower setup****. The polarization of the low-power beam (3.3 mW) coming from the outcoupler is cleaned by a half-inch half-wave plate (L/2) and Polarizing beam splitter (PBS). The desired beam shape is achieved by a telescope consisting of two cylindrical lenses ($f_{TL1} = 200mm$ and $f_{TL2} = 150mm$). An additional half-wave plate is added afterwards to control the intensity ration between the s- and p- polarized components of the beam. Finally, the beam is redirected upwards by a Right-Angle Mirror (RAM 1) mounted on a translation stage with a travel range of* 25 mm.

Upper Setup

The vertical beam goes through a hole in the upper breadboard and through the custom-designed PBS, and is separated by the cube into its s- and p-polarized components. The s-polarized beam is reflected by the cube towards a one-inch mirror placed at the back of the tower, which reflects it back through the cube and away from the tower, the so-called Back-Mirror (BM), passing two times through a quarter-wave plate secured between the cube and the BM. Note that the BM used for the test setup differs from the custom 30 mm square mirror which will be used in the final setup, limiting the minimal separation of the beams at which the accordion can be observed. In this case, the minimal separation achievable is 19.33 mm.

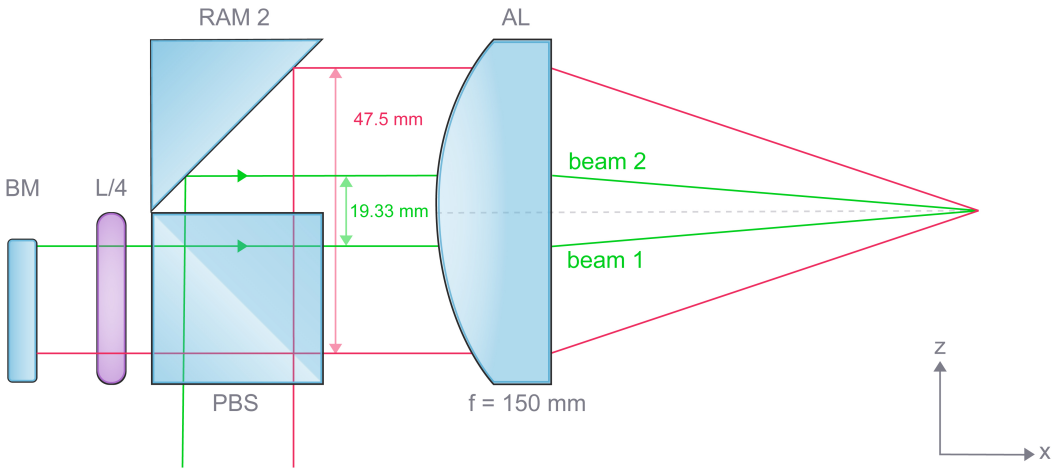

Figure 5.3: *Optical path on the upper breadboard. The setup, mainly mounted inside the designed mount tower, produces two parallel beams (beam 1 and beam 2) with tunable separation. The Aspherical Lens (AL), with a focal length of* 150 mm*, then focuses them at a shallow angle and produces the desired interference pattern. The separation of the beams is achieved by a PBS and a combination of a Back-Mirror (BM), a second Right-Angle Mirror (RAM 2), and a quarter-wave plate. Due to the small size of the test Back-Mirror, the minimal separation of the beams that can be reached is* 19.33 mm*. The maximal separation planned for the real setup is achieved at* 47.5 mm*.*

On the other hand, the p-polarized component is transmitted by the PBS and reflected by the upper Right-Angle Mirror (RAM 2) away from the tower. The resulting parallel beams, both p-polarized, are focused by an aspherical lens from Edmund Optics with a diameter of 75 mm and an effective focal length of 150 mm.

At the time of this thesis, the final custom lens, designed for the real setup,

has not been delivered, thus the use of the temporary solution available in stock at Edmund optics.

Imaging Setup

The resulting interference pattern is imaged with a Newport Beam Profiler from the LBP2 series with a pixel size of 4.4 µm. The camera can be placed on a linear stage at the estimated focal point of the lens, or alternatively, a microscope objective can be used to magnify the pattern and better observed the small fringes at a maximal beam separation.

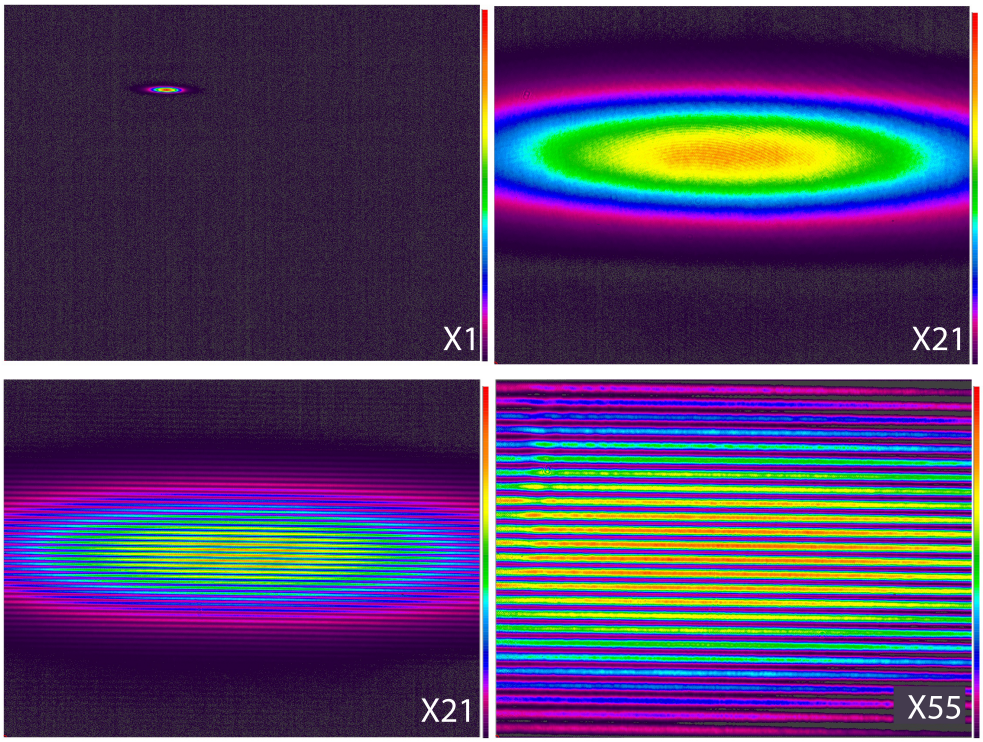

Figure 5.4: *Raw data recorded with the Newport Beam Profiler.* ***top left:*** *Individual beam measured directly at the focus of the lens with no magnification.* ***top right:*** *Individual beam measured with the microscope objective with a magnification of* $\times 21$*. Note that the beam waist in the horizontal and vertical direction is measurable and will be use for analysis purposes.* ***bottom left:*** *Accordion lattice for a beam separation of* 19.33 mm *recorded with* $\times 21$ *magnification.* ***bottom right:*** *Accordion lattice for a beam separation of* 19.33 mm *with the maximal magnification of* $\times 55$*.*

For precise measurements of the fringe distance, a $\times 20$ DIN Achromatic finite conjugate objective from Edmund Optics is placed on the translation stage.

The distance between the objective and the camera will determine the final magnification. Throughout this chapter, three setups are implemented. First, no magnification is used, which allows determining the real size of the beams at different points of the optical path. A second magnification of $\times 21$ is used to precisely look at the beams' vertical and horizontal displacement, and the larger fringes, while also being able to observe the beam profile. Finally, the largest magnification of around $\times 55$ is used to analyze the fringes for the whole beam separation range. Figure 5.4 depicts examples for all three cases after the alignment procedure has been performed.

A rough alignment of the described test system, as shown in figures 5.2 and 5.3 allowed to obtain the first images of the Accordion Lattice, however a thorough alignment procedure is imperative to guarantee the best performance.

5.2 Alignment procedure

The most important step to assure the dynamic stability of the accordion lattice is the proper alignment of all the optical elements. Even a small misalignment can be the source of significant aberrations. As mentioned before, the passive alignment of some elements is one of the main purposes of the opto-mechanical design, however, many degrees of freedom have to be optimized actively and with respect to each other.
Firstly, the lower setup is aligned paying special attention to the elements which will most strongly influence the final interference pattern. Afterwards, the elements in the tower are adjusted carefully with respect to the lower setup, i.e the vertical incoming beam. Finally, the aspherical lens, which is the most sensitive element, is aligned by different methods to achieve the highest precision possible. In the following sections, the exact steps are thoroughly described and commented on with recommendations for future alignment procedures.

The last step of the beam shaping is recording the beam profile at the focal point of the lens to make sure that it agrees with the expected values of $w_y = 250\,\mu\text{m} - 260\,\mu\text{m}$ and $w_z = 40\,\mu\text{m} - 50\,\mu\text{m}$. After the beam has been pictured with the camera, the data is run through a fitting procedure to find the width of the corresponding Gaussian curve. Figure 5.5 depicts one of the individual beams at the expected focal point of the lens, as well as the fitting curve and corresponding beam waists. The beam shows an inclination of 1.1° caused

by the misalignment of the aspherical lens, which is corrected during the more precise alignment procedure. This inclination was considered for the measurement of the beam waists and a correction was performed.

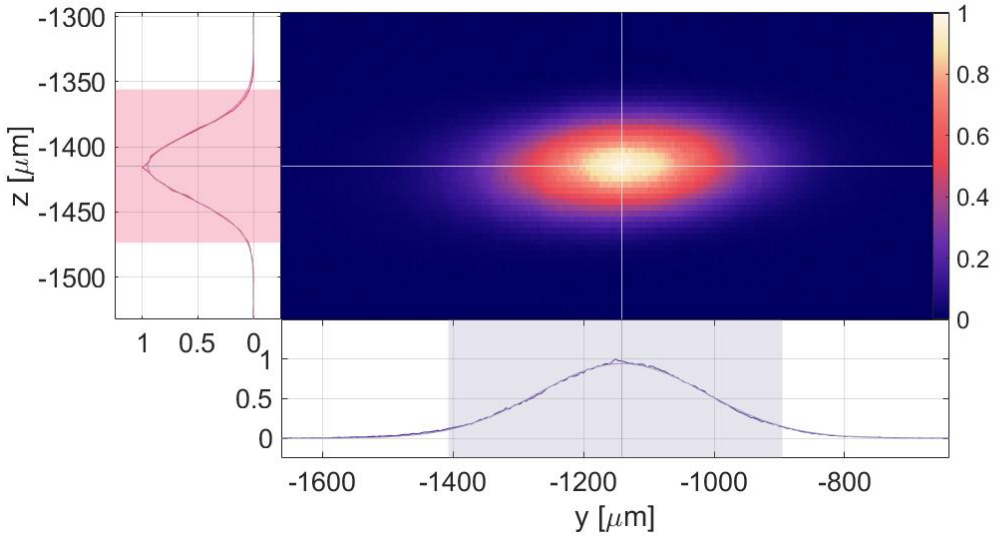

Figure 5.5: *Measurement of the beam profile at the focus of the aspherical lens. The shaded areas represent the fitted beam diameters for w_y (purple) and w_z (pink). After performing a correction to account for the inclination, the beam waist in y-direction is measured to be* $255.98(1)$ µm *and the beam waist in z-direction is* $48.268(8)$ µm. *The crossing of the horizontal and vertical white lines represent the calculated position of the peak.*

The measurement of the focused beam is used later on to determine the magnification of the system once the objective lens is applied.

5.2.1 Lower Setup

Beam Collimation

The first step, before going forward with the optical alignment procedure, is to optimize the collimation and shape of the outgoing beam by adjusting the position of the outcoupler lens. The beam profile is measured over a range on the order of the expected Rayleigh length (1.6 m) with a Newport Beam Profiler.

Before the lens was properly adjusted, measurements of the beam profile showed an unexpected behavior. On the one hand, the beam didn't show a symmetric Gaussian shape near the outcoupler. The intensity profile seemed to be shifted towards one side. Altogether, the strongest shape distortion appears

between 0 mm and 700 mm

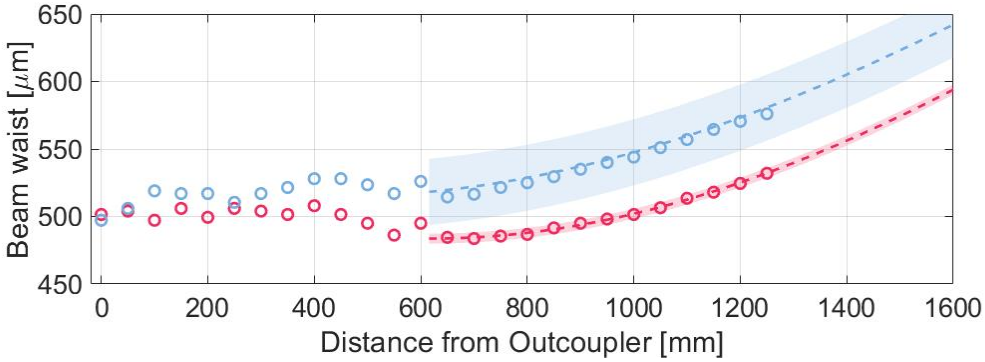

Figure 5.6: *Measurement of the beam collimation within the expected Rayleigh length. A fit function of the data after the* 600 mm *mark (dashed lines) provides the beam waist and its position. The shaded area represents the* 3σ *uncertainty for the fit on the beam waists. The beam waist in the y-direction (dark pink) is found to be* $483.6(12)$ µm *and is positioned at* $615(11)$ mm *from the outcoupler. The beam waist in the z-direction (light blue) is* $514.7(81)$ µm *at* $432(58)$ mm. *The measurement and fitting of the beam waists in both directions show strong astigmatism. Once the high-power laser for the real accordion is installed, a much better collimation with less aberrations should be achieved.*

On the other hand, the beam profile seems to be affected by the unexpected beam shape at different distances. At close distances from the outcoupler, 0 mm to 400 mm, the beam seems to diverge , but suddenly starts to focus between 500 mm and 600 mm, reaching minimum values below the expected beam waist in both directions. While the expected value is 521 µm, the beam waist in y-direction reaches approximately 480 µm, and 515 in z-direction. The large difference between the beam waists also demonstrates large astigmatism caused by the outcoupler lens. The divergence and then focusing of the beam gives the impression of a "hill" that goes up and down in the mentioned range. At larger distances, the beam diverges slowly, following the expected scaling for a Gaussian beam. The collimation achieved after various attempts, shown in figure 5.6, minimizes the observation of the small "hill" at small distances, as well as the divergence of the beam within the Rayleigh length. To estimate the precise divergence, a fit to determine the beam waist and its position is performed.

Taking into account the dimensions of the setup, the achieved collimation is considered to be sufficient. The positions of the telescope lenses are chosen to be close to the outcoupler to minimize the overall length of the optical path in the aim of avoiding the beam's divergence from affecting the waist in the y-direction at the lens's focus.

Beam Shaping

The two cylindrical lenses for the telescope setup are installed on rotational mounts in order to precisely adjust the major and minor axes to be orthogonal and parallel to the optical table respectively. The profile of the beam is measured after the two cylindrical lenses (before the aspherical lens) with the Newport beam profiler at large distances, which represent the expected length of the optical path through the tower and the focusing lens.

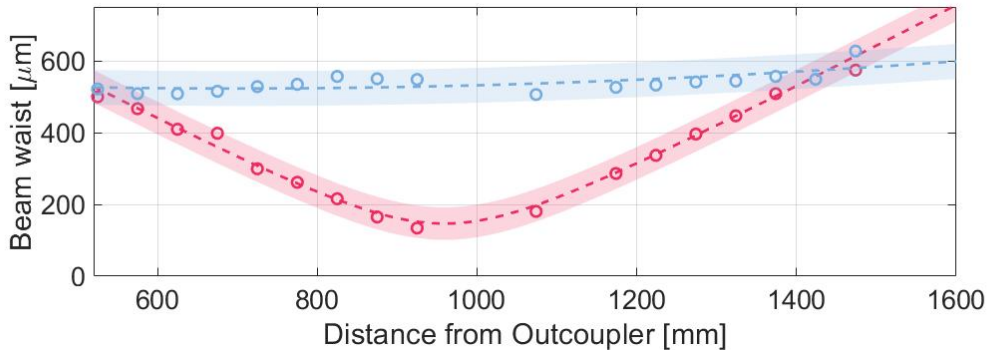

Figure 5.7: *Measurement of the beam profile after the telescope. A fit function of the data (dashed lines) provides the beam waist and its position. The shaded area represents the* 3σ *uncertainty for the fit on the beam waists. The beam waist in the* y*-direction (dark pink) is approximately* $146.4(2)$ µm *and is positioned at* $959(27)$ mm *from the outcoupler. The beam waist in the* z*-direction (light blue) is* $522.8(2)$ µm*, which is within the expected value of* 521.05 µm*, and looks sufficiently collimated.*

Right-Angle Mirror and Translation Stage

Once the collimation procedure and beam shaping are done, the alignment of the lower optical path can be performed, especially of the Right-Angle Mirror mounted on the linear stage, which is directing the beam upwards. One part of the vertical beam is reflected by the PBS towards the back mirror, while the other is transmitted in direction of the second Right-Angle Mirror. Due to the fact that neither the position nor the tilt of the PBS can be adjusted in any direction, the RAM1 tilt must be aligned in order to assure that the beam is orthogonal to the PBS bottom surface. Blocking the back-mirror and observing the reflection on the PBS surface allows for a relatively precise alignment of the RAM1's tilt around the y- and z-axes. Once this part is done, the RAM1 should not be read-

justed any further. A sketch for the alignment of the RAM 1 is depicted in figure 5.8 a. .

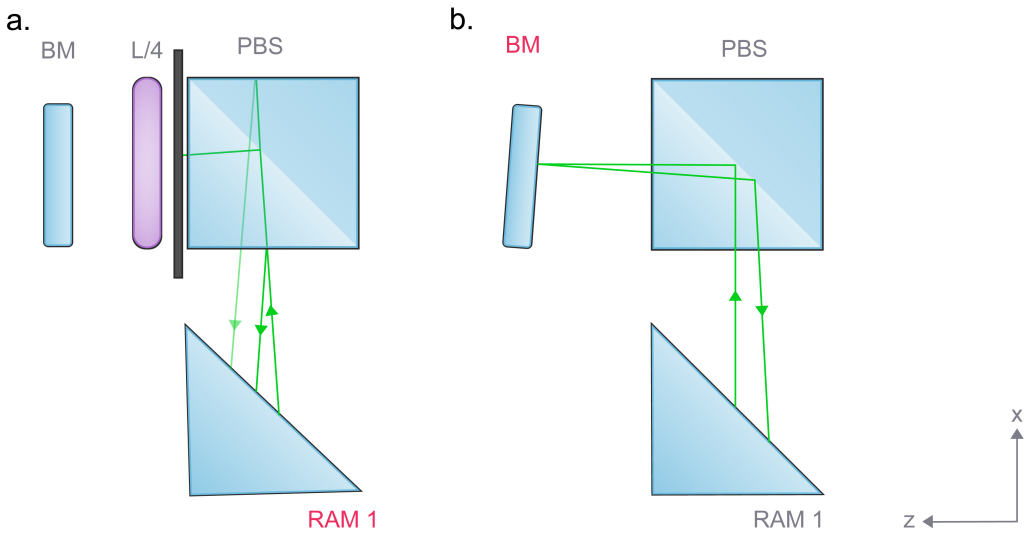

Figure 5.8: *Alignment procedure of the RAM1 and the back-mirror.**a.** Alignment procedure of the lower right-angle mirror on the translation stage (RAM 1). All retro-reflections on the bottom and upper surface of the cube should overlap with the incoming beam. The alignment should be checked for various positions of the translation stage.* ***b.*** *Alignment of the back-mirror is done with respect to the RAM 1. The tilt of the BM should not be readjusted afterwards.*

5.2.2 Upper Setup

Alignment of the Parallel Beams

The parallel beams result from the separation of the incoming beam at the tower. Through this chapter, the beam coming from the reflection on the PBS and the back-mirror, will be referred to as the lower beam, while the parallel beam coming from the reflection at the RAM 2 will be the upper beam.

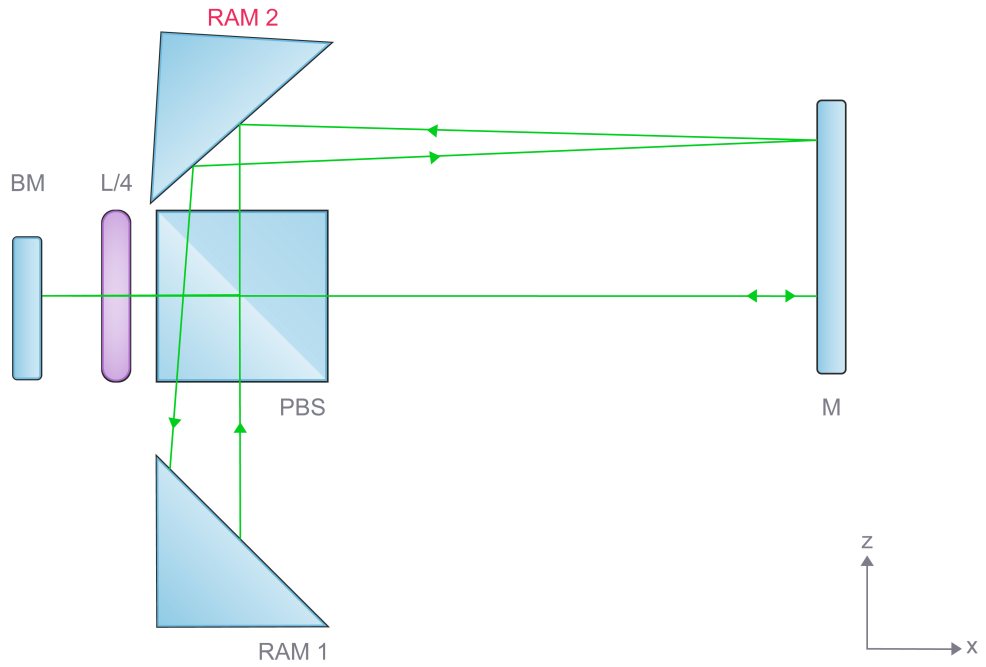

Figure 5.9: *Alignment procedure of the upper Right-Angle Mirror (RAM 2). An additional 2-inch mirror is placed as far as possible from the tower and aligned orthogonal to the lower beam. The mirror is then used to overlap the upper beam and its reflection.*

The proper alignment of the lower parallel beam with respect to the vertical beam is determined exclusively by the two degrees of freedom of the back-mirror in the tower. Removing the quarter-wave plate means that the polarization of the incoming beam remains unchanged, thus it is reflected back downwards by the PBS. One can make use of this reflection to adjust the back-mirror: once the incoming and the reflected beam overlap on the RAM1, one has achieved a good alignment. By adding the quarter-wave plate one can observe the path of the parallel beam relative to the upper setup. In case the beam is not following a straight path towards the expected position of the focusing lens, either the orientation of the whole tower or of the breadboard can be adjusted. However, the tilt of the back mirror should not be altered after its reflection downwards has been aligned. The adjustment of the RAM1 and the back-mirror is tested for various positions of the translation stage.

The second parallel beam is aligned with respect to the first beam by adjusting the tilt of the RAM 2. In this case, an additional two-inch mirror can be placed at a large distance in front of the tower. The two-inch mirror has to be aligned relative to the first parallel beam, and only afterwards it can be used to proceed with the alignment of the second beam.

Alignment of the Aspherical Lens

The main advantages of an aspherical lens, are the reduced focal shift caused by spherical aberrations, the improved resolution, and overall better system performance. However, one main disadvantage is the heightened sensitivity to the position and alignment of the lens relative to the incoming beams. An optimally aligned lens would mean that for all separations of the parallel beams, the beams meet at the same position in the x-direction. The relative shift on the x-axis caused by a misalignment will be referred to as shift of the focal point, or focal shift for short. For this particular lens, two alignment procedures were implemented to test the precision that can be achieved in terms of the resulting focal shift.

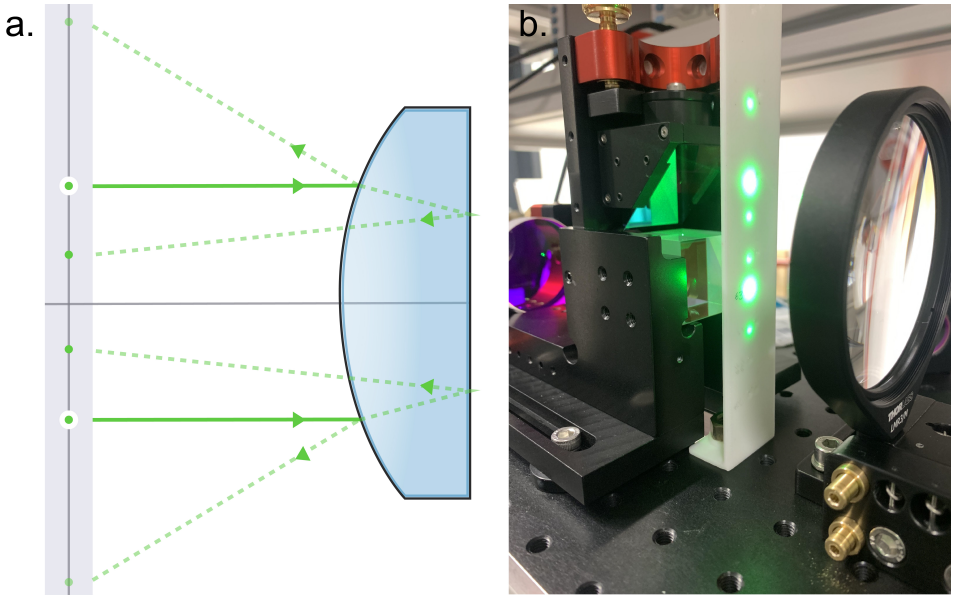

Figure 5.10: *First method for the alignment of the aspherical lens.* ***a.*** *Sketch of the working principle of the alignment procedure. The two parallel beams first meet the curved surface of the aspherical lens and are partially reflected outwards. The beams are reflected a second time on the planar back surface of the lens and are redirected inwards with an angle. Once the reflected pattern is symmetrical on the z-axis and perfectly aligned along the y-axis, the aspherical lens should be on the right position and orientation in respect to the incoming parallel beams.* ***b.*** *Example of a misaligned lens showing an asymmetrical pattern of the four reflections. The brightest points represent the entering point of the parallel beams. Between them, the reflections on the planar face of the lens can be observed. Finally going towards the edges, it is possible to see the reflections on the curved surface.*

The first method relies on using the reflections of the two beams on the two surfaces of the aspherical lens. For a perfect alignment, the four reflected beams should be symmetrical around the y-axis and centered along the z-axis, as shown in figure 5.10a. . The fine adjustment of the lens is possible thanks to the fact that it is mounted on a 4-axis stage, however, for this stage, it is not possible to decouple the lens position and its tilt. Therefore, it becomes increasingly harder to adjust the lens the closer one gets to the optimal alignment. One way to decouple the adjustment of the height and the tilt is to turn the lens around to have the flat surface directly after the tower. The alignment of the incoming and reflected beams allows to find the point at which the beam and the lens's surface are perfectly orthogonal. Once this has been done, one can turn the lens back around and try to achieve the best symmetry of the four reflections by rotating the screws equally. A careful iteration of this process should help align the lens to a high degree. The maximal focal shift observed at different positions of the lower linear stage after this alignment procedure was of 1.9 mm, therefore, the second alignment procedure was performed in an attempt to reduce this value.

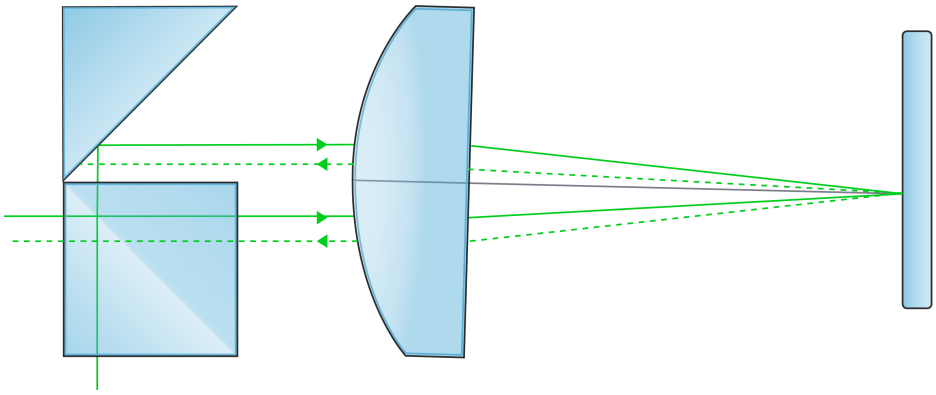

Figure 5.11: *Second method for the alignment of the aspherical lens. The incoming (continuous line) and outgoing (doted line) beams do not overlap, which reflects a misalignment of the focusing lens. The accuracy achieved by eye is sufficient to continue with the fine alignment procedure with a beam profiler.*

For the second method, a mirror is placed on a linear stage near the expected focal point of the lens. Firstly, this mirror is aligned by removing the lens and overlapping the retro-reflection to the incoming beams, similarly to the alignment of the second parallel beam described before. Afterwards, the lens is mounted back and the linear stage with the mirror is moved until one finds the focal point. Finally, the 4-axis stage is adjusted until once again the

reflected beams overlap with the incoming beams. This procedure doesn't require the lens to be flipped back and forth and seems to allow for a more precise alignment, with a resulting focal shift of $0.96(5)$ mm.

In addition to the aforementioned procedures, fine-tuning of the lens alignment can be performed by placing a camera at the expected focal point of the lens. The focal shift is mainly caused by a vertical and/or horizontal displacement of the individual beams for different positions of the lower translation stage. For this measurement, the second beam is blocked and the position of the first parallel beam is recorded for a fixed position of the upper translation stage. This position is chosen to be at the focal point observed for a constant beam separation, even though this will be varied in the last step. The lens is then adjusted until the overall displacement of the first beam is minimized. Directly afterwards, the procedure is repeated for the second beam. Nevertheless, in this case, the Right-Angle Mirror is adjusted instead of the lens. Once the displacement has been minimized, the blocking of the first parallel beam is removed and the focal shift is measured. At this point, a more precise focal point should be chosen and the procedure repeated until the displacement of both beams is minimized and the real focal point of the lens has been determined. If both beams are perfectly centered on the lens axis, any remaining displacement of the beams should be symmetrical.

Once this alignment was finished, no displacement of the beams could be observed for translation stage positions between 10 mm and 20 mm, as well as no focal shift. This measurement was done without any type of magnification, limiting the precision of the procedure. For the real setup and to avoid any misalignment below 100 µm, the alignment procedure can be repeated with a microscope objective between the lens and the camera. The following measurements of the beams' displacement as well as the final focal shift were recorded with a magnification of roughly $\times 21$.

Furthermore, the distance between the back of the lens and the objective was found to be approximately $141(1)$ mm. Taking into consideration the working distance of the objective (0.8 mm), we estimate the focal point of the aspherical lens to be at $140.2(10)$ mm. The uncertainty here is roughly estimated by the precision we can achieve with a standard rule.

5.3 Test Results

5.3.1 Individual Beam Characterization

Before characterizing the stability of the optical accordion, we first measure the stability and control of the individual beams, which will be the source of any instability of the accordion lattice.

In the first part of this section, the control of the beam separation is determined by the relation between the lower translation stage position and the measured beam separation. A good alignment of the system will yield a perfect linear dependence, with the beam separation augmenting twice the shift of the translation stage. Afterwards, the spatial stability of each beam is studied by observing its vertical and horizontal displacement at the estimated focal point of the lens. In theory, the position of both beams at the focus should be the same for all beam separations. In reality, this is not the case, which means that the **interfering point** of the beams is shifting back and forth along the propagation direction for different positions of the lower translation stage. Since the atoms will be trapped exactly at the interfering point, if it shifts strongly, the atoms will be heated or could escape the trap. Additionally, for a significant displacement of the beams relative to each other at one position, the intensity of the middle fringe will be reduced compared to the maximal overlap of the beams, reducing the trap depth seen by the atoms.

Beam separation

The final beam separation D was determined by measuring the beam separation for multiple lower translation stage positions and then fitting a linear function as shown in figure 5.12. The slope of the fitted line is $2.01(19)$, which means that for every increase of 1 mm on the linear stage, the beam separation will increase by 2.01 mm, matching the expectations.

Vertical Displacement of the Individual Beams

The vertical displacement of the individual beams at the focal point, i.e the movement along the z-axis, will later reflect as a shift of the interference pattern along the x-axis, which is the propagation direction. A significant shift of the interfering point will be detrimental to the experimental application, due to the fact that a reduced trap depth of the central fringe may cause heating or

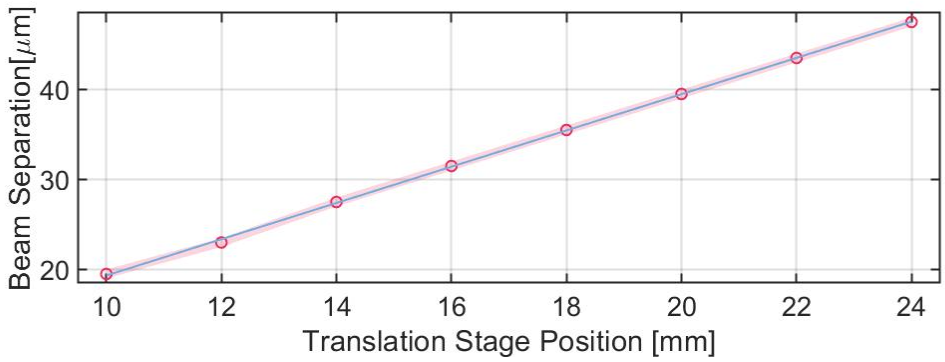

Figure 5.12: *Measurement of the beam separation as a function of the lower manual translation stage position.*

significant, if not total loss, of the trapped atoms. The use of the microscope objective allowed us to observe the vertical displacement more clearly than during the alignment procedures. Figure 5.13 depicts the vertical shift of the individual beams as a function of the lower translation stage position.

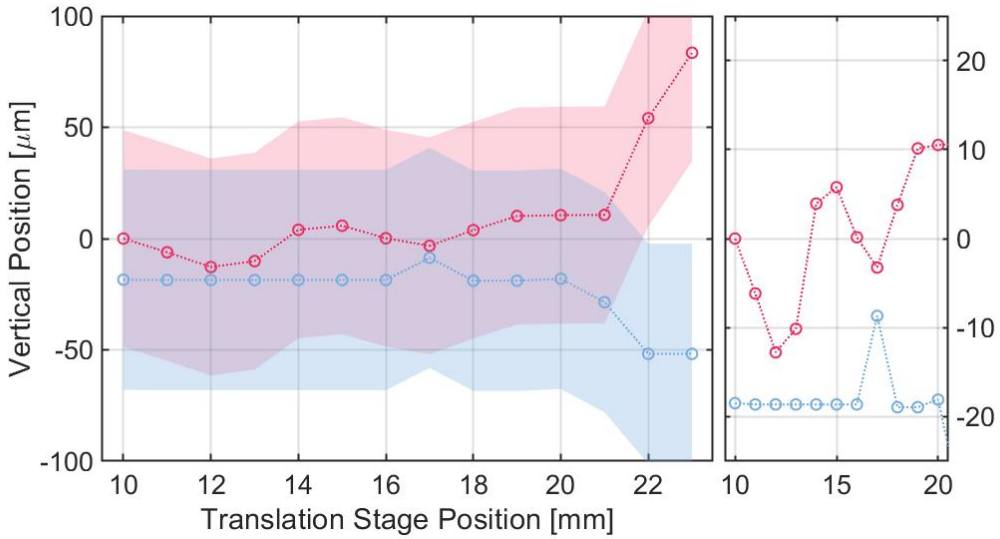

Figure 5.13: *Vertical Displacement of the individual beams.* ***left:*** *Vertical displacement of the individual beams measured on the beam profiler with* $\times 21$ *magnification. The lower and upper beam, in dark pink and light blue respectively, show an asymmetric displacement around the center, with unexpected high values after* 20 mm. *The shaded areas around the data points represent the beam waist of the beams for every measured point, and should serve as a reference to observe the overlap of the beams.* ***right:*** *Zoom on the most stable area* 10 mm *to* 20 mm. *The beams show a maximal displacement of* 22 µm, *with the upper beam showing a higher stability than the lower beam. Large vertical displacements will cause a significant loss of intensity of the middle fringe of the Accordion. For the measured beams, we expect the loss to be below 3%.*

The shaded area represents the beam waist and should help reference the overlap of both beams. Altogether, we observe constant overlap for the majority of the measured data points. The upper beam shows less vertical displacement between 10 mm and 20 mm than the lower beam, with a maximal shift below 11 µm. On the other hand, the lower beam shows two times the deviation of the upper beam, with a maximal shift of around 22 µm. After the 20 mm mark, the vertical displacement seems to increase significantly, and at 22 mm the beams do not overlap anymore. The large separation between the beams between 21 mm and 25 mm could not be reduced after multiple alignment attempts, and due to the observation of a strange jump at 20.5 mm while moving the lower translation stage, we concluded that the focal shift is caused by spherical aberrations of the lens. This issue may be resolved once the custom-designed lens is implemented. A maximal beam separation of 20 µm, observed between 10 mm and 19 mm, represents around 42% of the beam waist and reduces the trapping frequency by nearly 2.85% according to simulations. Similar values have been observed in [22] and [27]. The minimal beam separation for positions after 19 mm is 30 µm, around 63% of the beam waist. The trapping frequency is reduced by around 6.3%. Assuming a trapping frequency in z-direction of nearly 20 kHz, the loss will represent over 1250 Hz. For the final setup, 20 µm should be considered the upper limit, especially since higher-quality optics, like the custom-designed lens, will be implemented.

Additionally, we observe a significant asymmetry in the beams' movement. As mentioned before, for an ideal lens we expect a symmetric displacement for a perfectly aligned lens. A better alignment and a higher-quality lens will improve the measured displacement and reduce the variation of the trap depth for the dynamic application of Accordion.

Horizontal Displacement of the Individual Beams

Analogously to the vertical displacement, the horizontal displacement is measured thoroughly. The plotted data demonstrates a good overlap of the horizontal beams for all translation stage positions. However, a closer look shows a shift in the order of 20 µm for beam 2, and of roughly 30 µm for beam 1. This means that the contribution of the horizontal movement of the beams to the shift of the interfering point is in the same order as the vertical displacement. Nevertheless, due to the larger beam waist, the intensity variation caused by this is expected to be much smaller. Once again, a jump after the 21.5 mm mark

suggests spherical aberrations caused by the lens. The upper beam seems to be better aligned with respect to the lens, with a total deviation below 10 µm for linear stage positions between 10 mm and 18 mm.

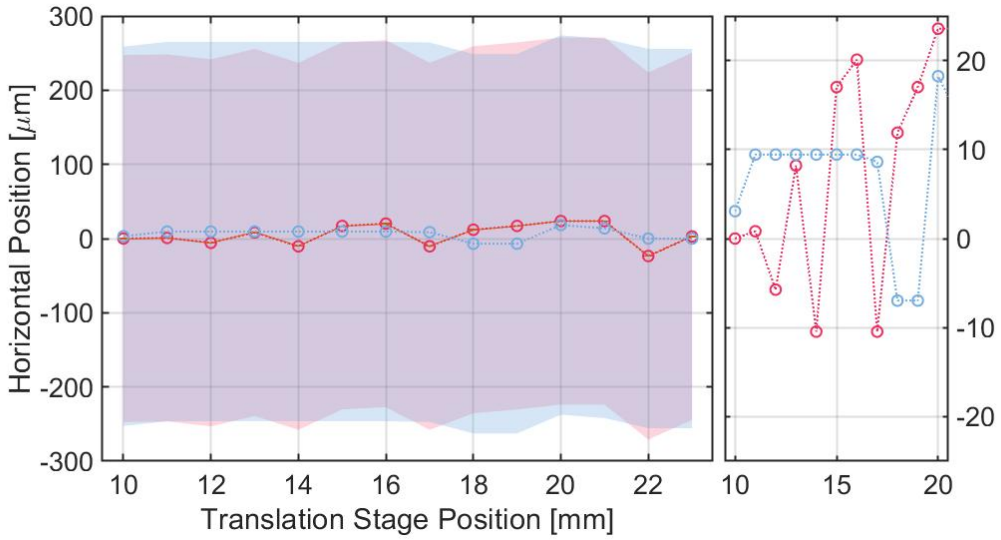

Figure 5.14: *Horizontal Displacement of the individual beams.* ***left:*** *Horizontal displacement of the individual beams as a function of the lower translation stage position. The stable overlapping of the beams, depicted as the purple shaded area, means a rather stable intensity and trapping frequency of the interference pattern for different beam separation.* ***right:*** *A more detailed look to the stable area, i.e the position range which is not strongly affected by spherical aberrations,* 10 mm *to* 20 mm*, reveals that the contribution of the horizontal displacement to the focal shift is in the order of the contribution of the vertical displacement discussed before.*

5.3.2 Characterization of the Interference Pattern

The following section consists of the analysis of a carefully recorded set of data measured with the test setup. After the measurements to determine the stability of the individual beams, we continue with a detailed characterization of the optical accordion itself. Taking the vertical and horizontal displacement of the beams at the expected focal point into account, we expect to observe a certain spatial instability of the fringe pattern as well. The first part of this section will present the measured shift of the interfering point of the beams.

Afterwards, the range of achieved fringe distances will be discussed, as well as the dynamic stability of the middle fringe. Finally, additional deviations from the ideal simulated patterns, regarding the orientation, the phase shift,

and the contrast of the accordion, will be explained and exploited to trace back issues with the experimental setup. Possible solutions and recommendations to achieve the best stability and performance for the final setup will be discussed.

Shift of the Beams' Interfering Point

The displacement of the interference point is measured by finding the strongest overlap of both beams while looking at the interference pattern on the camera with a magnification of approximately $\times 21$. The effects of the vertical and horizontal displacement discussed previously are reflected in the measurement, as shown in figure 5.15. For the stable range mentioned above, 10 mm to 20 mm, the interfering point's shift doesn't exceed 100 µm, while after that, it increases linearly to almost 500 µm. This shift is equivalent to the displacement that the deepest point of the trap will experience along the x-direction, causing heating and significant loss of atoms. A fine-tuning of the alignment procedure is imperative to reduce the shift of the interfering point as much as possible, and the values recorded with this setup should be considered the upper limit to the achievable precision.

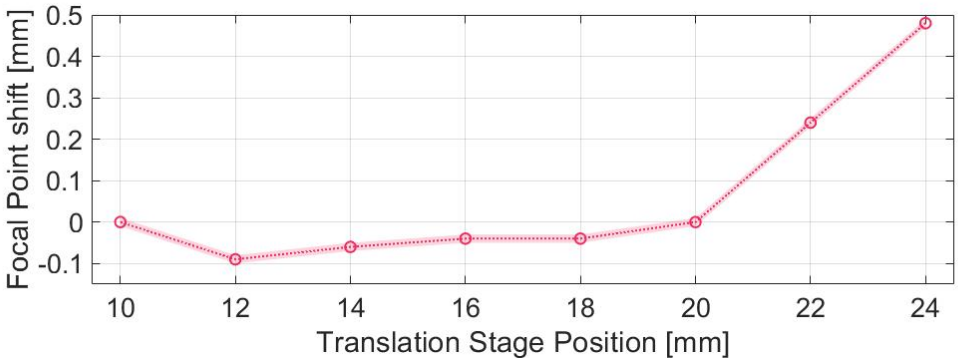

Figure 5.15: *Shift of the beams' interfering point measured with a magnification of $\times 21$ for a large range of linear sage positions. The alignment procedure helped reduce the variation of the focal point to less than* 100 µm *for the majority of the beam separations. However, sudden jumps and loss of the interference pattern at larger beam separations, indicate strong spherical aberrations far from the center of the aspherical lens.*

Fringe Distance

The fringe distance, together with the intensity, determines the trapping frequency that can be achieved by the interference pattern. In fact, the overall concept of an accordion lattice relies on the possibility to dynamically control and adjust the fringe spacing. If a convolution of a cosinusoidal and Gaussian function is fitted on the data recorded on the beam profiler, the fringe separation can be extracted directly from the period of the cosine term. However, in order to decouple the error of the fit of the Gaussian function from the calculation of the fringe distance, a Fourier Transform is performed instead. Figure 5.17 illustrates the recorded data at a beam separation of 19.33 mm and the corresponding z-Potential slice at the center. The computed fringe distance d is depicted by the blue lines as the distance between two fringes near the center. Figure 5.16 displays the performed Fourier Transform with a peak at the inverse of the fringe distance.

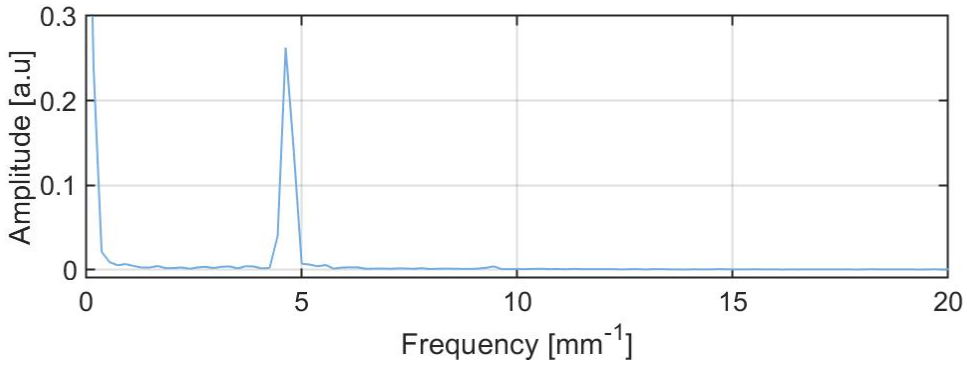

Figure 5.16: *Example of the Fourier transform performed to abstract the period of the Accordion Lattice.*

Note that for this set of measurements, the interference pattern with a magnification of $\times 21$, which has been used above to characterize the individual beams, doesn't provide a high enough resolution to observe the smallest fringes. Therefore, the camera is moved further away from the objective to a distance of $442(2)$ mm, which according to calculations represents a magnification of $\times 55.25(25)$. The real magnification can be found by measuring large fringe distances with the first magnification and comparing them to the size resulting from the second magnification, see 5.4. The real magnification is measured to be $\times 55.89(30)$, which is well within the 3σ margin of the expected value. The peak signal away from the zero-point in figure 5.16 represents the inverse of

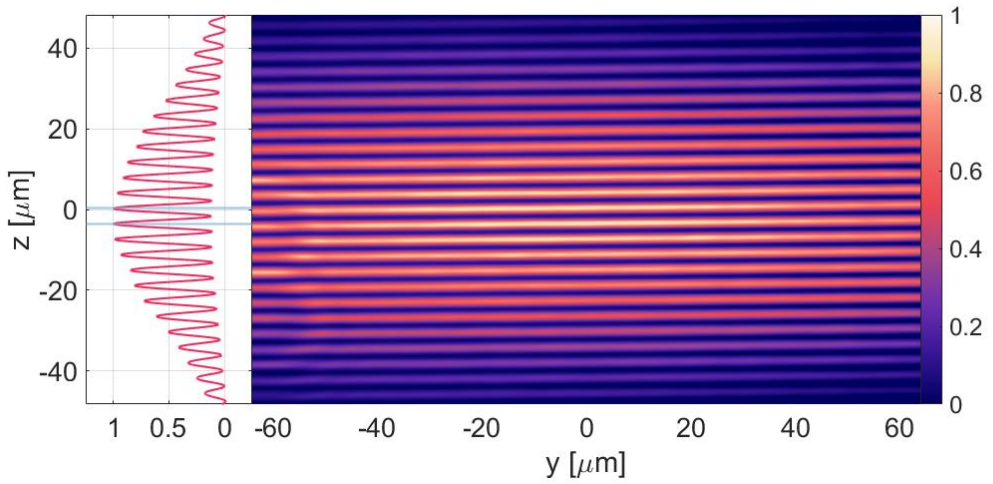

Figure 5.17: *Processed image of the interference pattern at* 19.33 mm*. One of the analyzed slices along the y-direction, which represents the potential along z-direction, is plotted on the left in dark pink. The calculated fringe distance is represented by the distance between the two light blue lines.*

the period of the lattice, which yields a fringe distance of 215.58 µm for the raw data, which equals 3.85 µm once the magnification correction is done.

This process is repeated for beam separations between 19.33 mm and 41.49 mm in roughly 1 mm steps. The fringe distances are plotted as a function of the beam separation in figure 5.18. The focal length of the aspherical lens can be precisely calculated by applying the approximation

$$d = \frac{\lambda f_{AL}}{D}. \tag{5.1}$$

The fitting yields f_{AL} =139.5(5) mm, which is within the 1σ of the measured focal length of 140.2(10) mm (see section 5.2.2). The fit also provides a better overview of the achievable fringe distances for our setup. The minimal beam separation, which yields the maximal fringe distance, is expected to be around 3 mm. This corresponds to the distance between the RAM 2 and the PBS (1.5 mm), plus a margin of three times the beam waist for each beam ($2 \times 3 \times 255$ µm), which guarantees that the beam is not cut off by the optical element. The expected maximal fringe distance is computed to be 24.74 µm. For the maximal beam separation of 47.5 mm we expect a fringe distance of 1.56 µm.

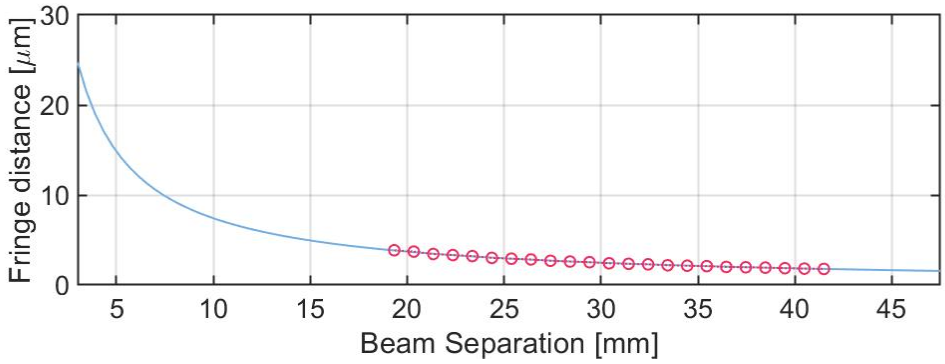

Figure 5.18: *Fringe distance d as a function of the beam separation D. The data points (dark pink) are fitted to find the focal point of the aspherical lens (light blue).*

Dynamic Stability of the Central Fringe

The central fringe of the optical accordion is where the atoms will be loaded and trapped. It is imperative that its position shifts as less as possible during the compression of the trap, as has been mentioned before. In order to determine the dynamic stability of the central fringe, it must first be identified. Ideally, the position of the central fringe would coincide with the center of the Gaussian packet defining the intensity of the potential. Due to factors discussed later, this is not always the case for the experimentally realized interference patterns. In case the intensity distribution is well defined by a single Gaussian curve, one could assume that the fringe positioned closest to the center of the fitted Gaussian packet is the central fringe. However, if the beams are not at the same position, and instead show a large enough separation that two Gaussian curves can be identified, the position of the middle fringe should be confirmed manually by considering the evolution of the interference pattern in dependence of the beam separation. The measurement of the vertical position of the central fringe is performed for different positions of the lower linear stage, i.e for different beam separations. Note that for the test setup, only a manual linear stage is available, so the measurements have been taken over a longer time period and fluctuations in the environment that could affect the accordion cannot quantitatively be accounted for. The results are plotted in figure 5.19.

The vertical position shifts by around 5 µm in total from the smallest to the largest beam separation. The variation seems to be stronger at the beginning, with jumps in the order of 2 µm, while it seems to be more stable at larger beam distances. We note that in the case of the first data point at 19.33 mm, the Gaussian center appears to be in the middle of two fringes with similar intensity,

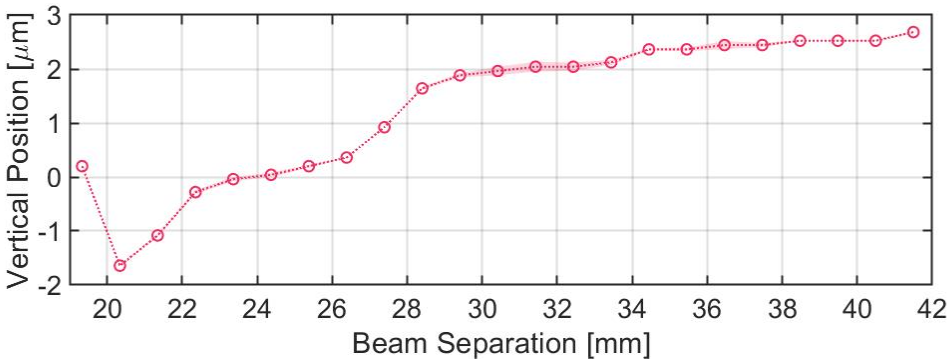

Figure 5.19: *Vertical position of the central fringe as a function of the beam separation D.*

making the choice of the middle fringe more difficult. Observing the tendency of the movement of the central fringe from that point onwards, it could be argued that the "real" middle fringe is the next fringe in the negative z-direction. A more detailed discussion regarding the shift of the middle fringe in respect to the Gaussian packet follows at the end of this section. In contrast, between 28 mm and 41.5 mm the central fringe does not shift by more than 2 µm. In [22] and in [27], a displacement below 1.5 µm and 2 µm for much larger d ranges has been achieved, which warrants a more precise alignment of the present setup.

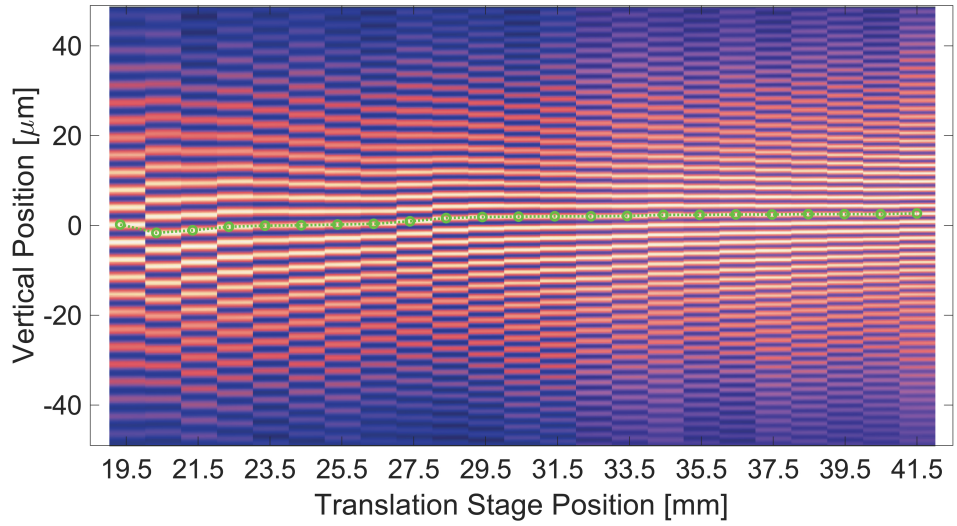

Figure 5.20: *Vertical position of the central fringe as a function of the beam separation D for the full camera range in z-direction (-45 to 45*µm*). In the background, superimposed to the vertical shift diagram, are the corresponding intensity slices of the fringe patterns.*

Inclination of the fringes

During the initial imaging of the Accordion lattice, two key observations were made. On the one hand, a significant inclination of the fringes relative to the horizontal axis was identified. On the other hand, an unexpected bending of the individual fringes was observed. During the real application, the lattice fringes should be as flat and parallel to the ground as possible to avoid gravitational effects from affecting the in-plane potential seen by the atoms. After the careful alignment procedure, the inclination for different stage positions was considerably reduced but still measurable with the largest magnification. Interestingly enough, the previously observed bending completely seems to disappear. To begin with, the tilt of the fringes present after the alignment will be discussed. At the end of the section, an additional example of the initially observed bending will be displayed and discussed.

The final tilt for a fixed D is determined by slicing the data along the y-axis and finding the peaks corresponding to the fringes in z-direction. Afterwards, the y-profile for a single fringe is reconstructed and fitted with a linear equation. In order to avoid large errors caused by the uncertainty of broader, smaller peaks' positions, the fitting was performed only for the fringes within the beam waist. The final orientation of the interference pattern results from the averaging of the slopes for all fringes in the selected range.

Figure 5.22 shows the same potential as in figure 5.17 with an additional green line following the middle fringe to reference the calculated final tilt of $0.0124(6)$ rad.

The inclination of the lattice is measured for all data files and plotted against the beam separation D, as shown in figure 5.23. In order to correct the tilt experimentally, we now search for its cause. From the geometry of the setup leading to the interference pattern, it can be deduced that the observed tilt of the fringes on the y-z-plane is caused by a rotation of the ideal system around the x-axis by ψ. In practice, this means that the axis defined by the middle points of the individual beams is not orthogonal along gravity because the central points of both beams are shifted in respect to each other on the y-axis by Δy.

This shift is attributed to a misalignment of the parallel beams before entering the aspherical lens. The relative position difference at the lens, Δy in figure 5.23, is found to be approximately $0.93(6)$ mm. The effect of the horizontal shift

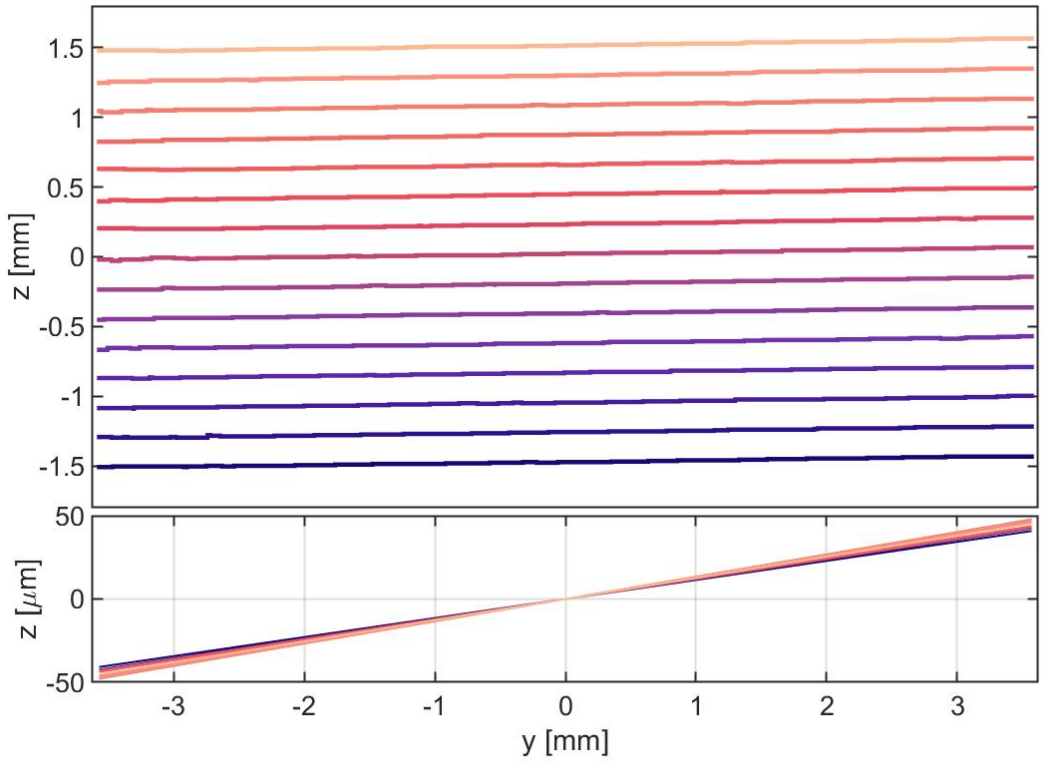

Figure 5.21: *Measurement of the fringes' inclination.* ***top:*** *Reconstruction of the fringe positions on the y-z plane. Points corresponding to the same fringe are marked by the same color. Only the fringes within the beam diameter are used for the tilt analysis.* ***bottom:*** *Linear fits corresponding to the individual fringes above. The final inclination is given by the average of all slopes.*

of the beams can be simulated by determining the corresponding angle φ, where

$$\varphi = \text{atan}\,\frac{\tan\psi D}{f_{AL}}. \tag{5.2}$$

The calculation of the relative displacement, together with the information gathered in section 5.3.1, can help us deduce how the observed misalignment can be corrected. In this case, it has become clear that the lower beam has to be readjusted slightly, as its measurement of the horizontal displacement shows a stronger variation, which indicates that it is not centered on the lens. However, it has been explained during the alignment procedure, that any readjustment of the lower beam should be avoided. For this reason, one could consider the alternative of adjusting the aspherical lens position and tilt to better align with

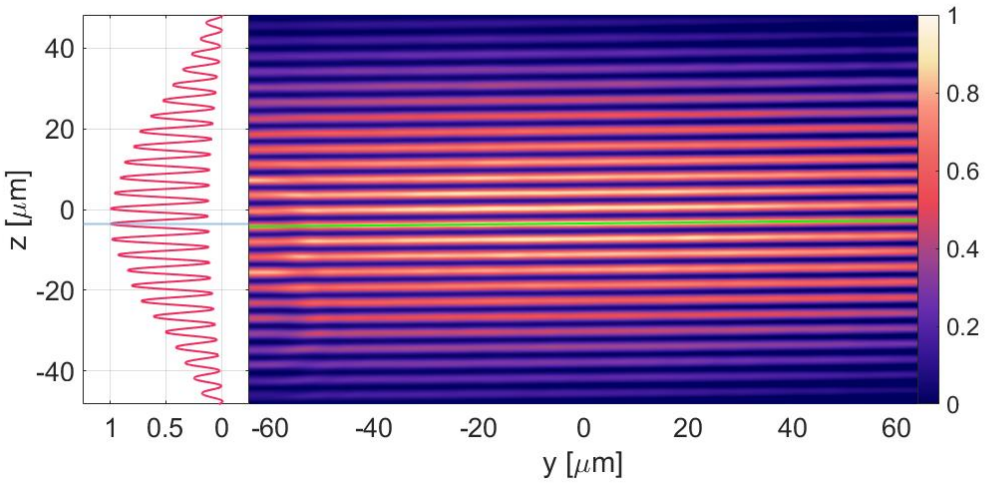

Figure 5.22: *Processed image of the interference pattern for D =19.33 mm and d =3.86 µm. The position of the central peak is marked by the light blue line on the left graph. The measured inclination of the central fringe is shown by the green line.*

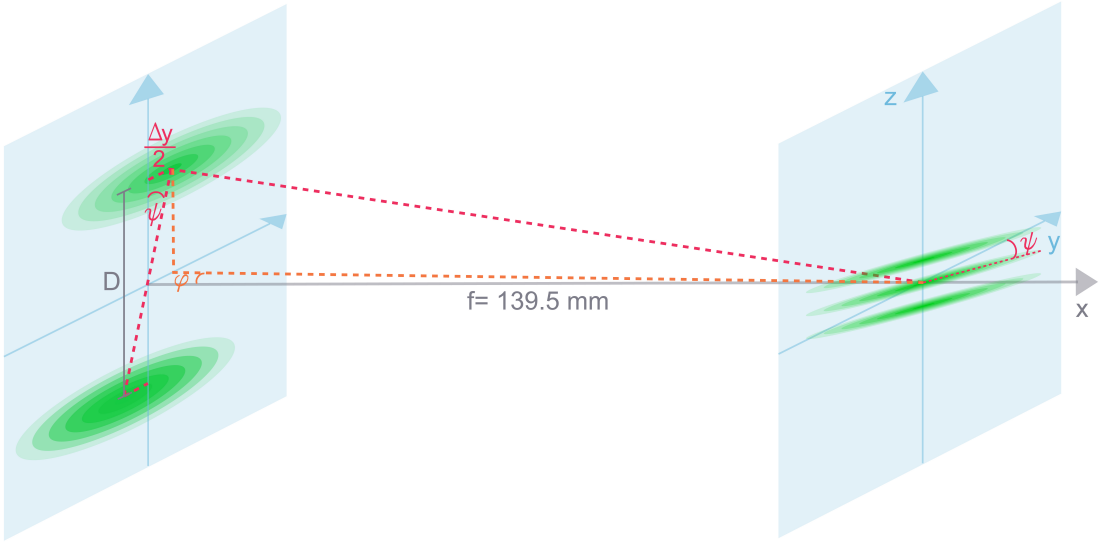

Figure 5.23: *Rotation of the interference pattern around the x-axis by ψ caused by an horizontal shift of the beams Δy.*

the lower beam, and then readjusting the upper beam accordingly.

As mentioned before, a bending of the fringes could be observed previous to the final alignment procedure. The shape of the bent fringes could be fitted with a quadratic function and analyzed similarly to the case of the linear fringe. Figure 5.25 shows an example of the reconstruction of the fringes and the cor-

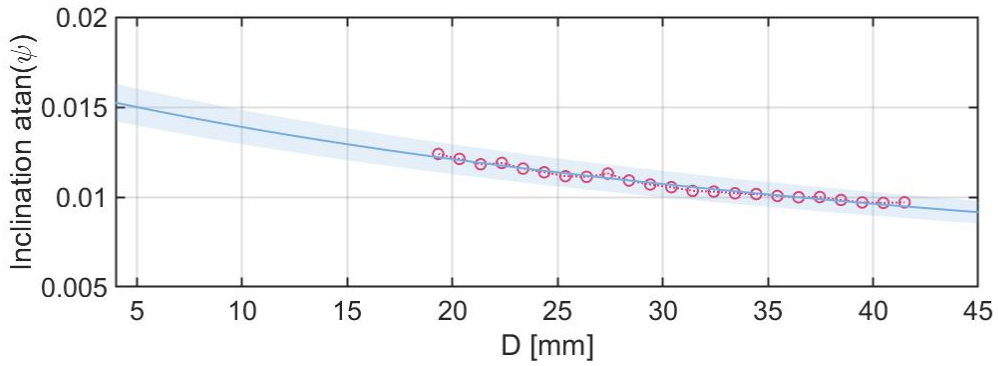

Figure 5.24: *Inclination of the lattice for different beam separation. A fitting on the measured orientation yields* $\Delta y = 0.93(6)$ mm.

responding quadratic fits. The unexpected bending of the interference pattern

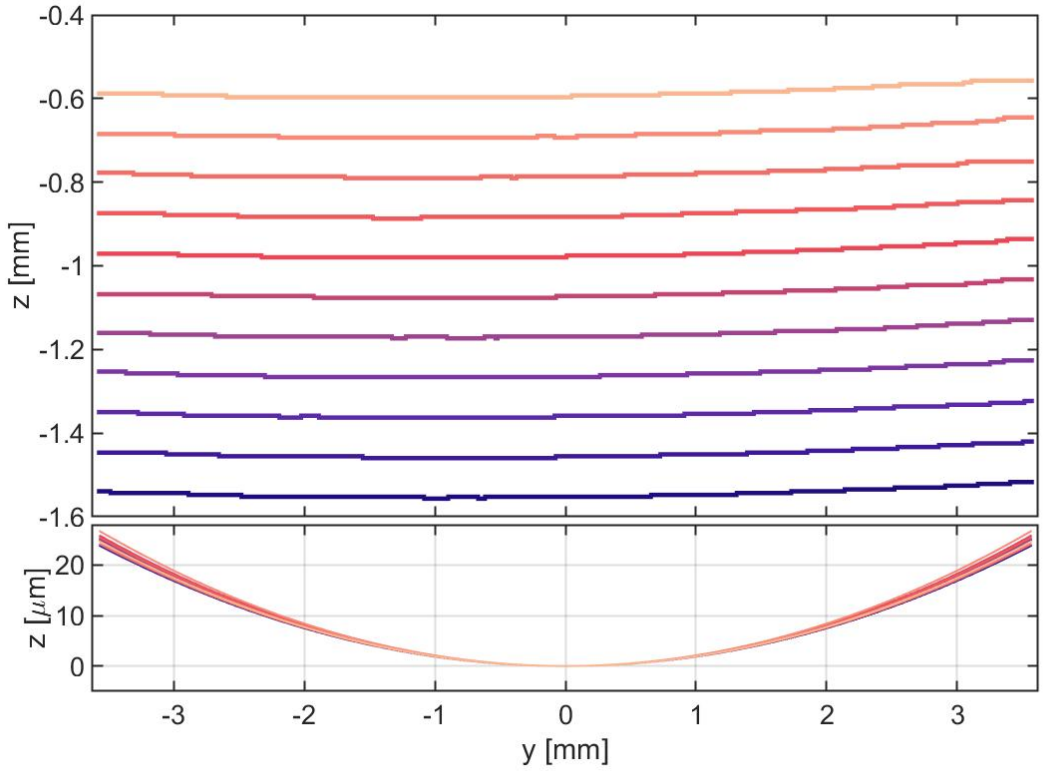

Figure 5.25: *Bending of the lattice fringes before alignment.* ***top:*** *A reconstruction of the fringes allows to observe a slight bending in the upwards direction. Data points in the same color correspond to the same fringe.* ***bottom:*** *Quadratic fits corresponding to the individual fringes above. The final fit parameters for an interference pattern are given by the mean of the parameters for all quadratic fit functions.*

is most certainly caused by a misalignment relative to the aspherical lens. This assumption is derived from the fact that the bending vanishes once a precise

alignment of the lens is achieved. A possible explanation would be that the spherical aberration curves the pattern when the beams are not centered properly. According to simulations, another probable cause for the bending is the path difference itself. Additional measurements of this effect could provide a more certain explanation and possibly allow for its simulation.

Phase measurements

To determine the trapping frequency inside the central fringe of the optical accordion, it was assumed during simulations that the central fringe was located at the center of the Gaussian packet. This corresponds to a deeper trap on the center than on any side fringes. Nevertheless, phase shifts $\Delta\delta \neq 0$ cause a displacement of the fringes within the Gaussian packet. The maximal effect of a phase shift is found at $\Delta\delta = \pi(\mod 2\pi)$, where the fringe pattern is symmetrical around the Gaussian center, causing the two fringes closest to this position to have the same intensity.

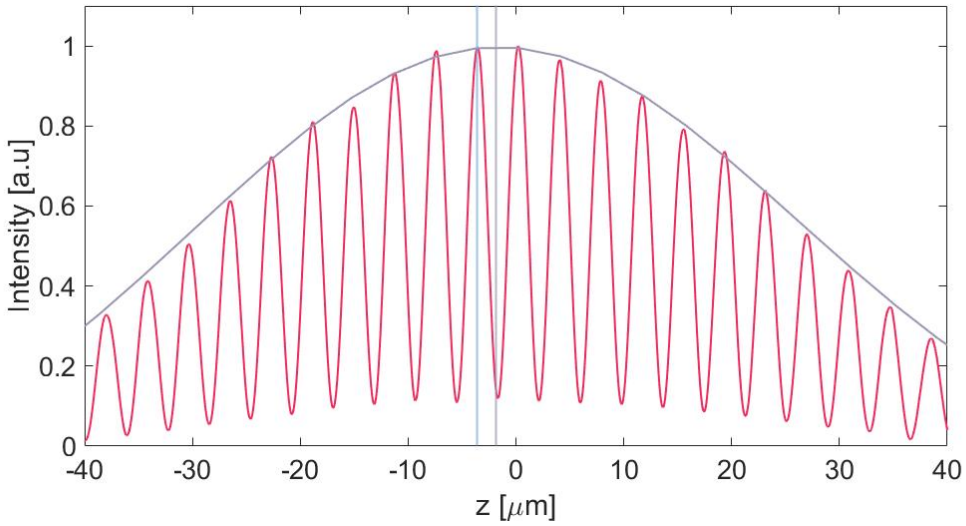

Figure 5.26: *Example of a large phase shift. The measured phase shift of $0.45x2\pi$ for $D = 19.33$ mm is very close to the maximal possible phase shift π. This means that the central fringe (light blue) is almost a half-period away from the Gaussian center (gray). The large phase creates an almost symmetric interference pattern around the Gaussian center. The symmetry of the pattern makes it more difficult to identify the real central fringe.*

An example of a large phase was found at 19.33 mm, which, as mentioned before, made the identification of the real central fringe more difficult. The phase was determined by calculating the distance between the Gaussian cen-

ter and the closest fringe, and dividing it by the periodicity d (see figure 5.26. For 19.33 mm the calculation yields 0.45 in terms of 2π.

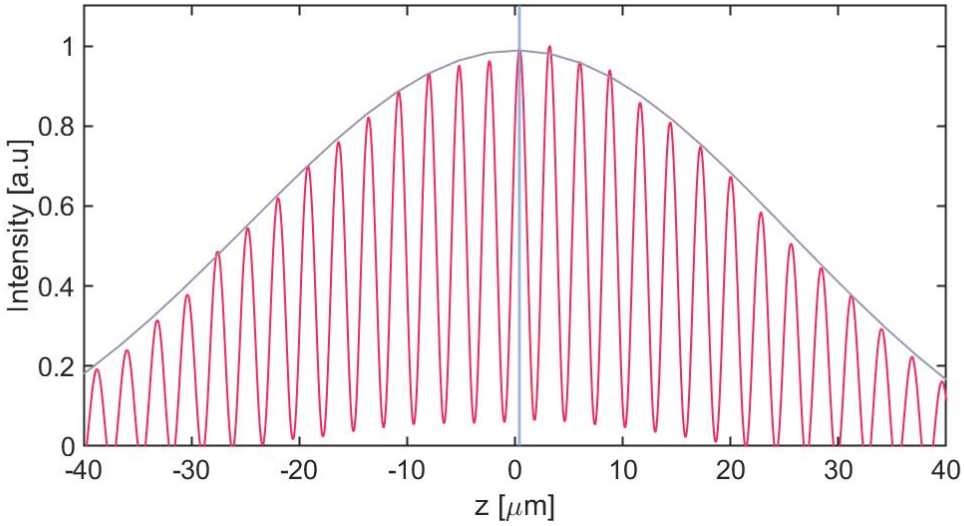

Figure 5.27: *Example of a small phase shift. The measured phase shift is 0.008x2π for $D = 26.39$ mm, which means that the central fringe (light blue) is positioned almost at the Gaussian center (light gray).*

In contrast to the last example, figure 5.27 depicts the interference pattern for D =26.39 mm, with its central fringe very closely positioned to the Gaussian center, and therefore a very small phase shift ($0.008 \times 2\pi$). The computed phases for all beam separations are plotted in figure 5.28.

Considering the relation

$$\Delta\varphi = \frac{2\pi\Delta L}{\lambda}, \tag{5.3}$$

the two main causes for the phase shift are variations of the optical path ΔL in the order of nanometers and variations of the wavelength λ. Assuming a stable wavelength during one measurement, we can trace the phase back to an optical path difference between the beams.

Adding a phase $\Delta\varphi$ and a tilt term to our simulations, we can accurately replicate the experimental measurements. An example for 19.33 mm is depicted in figure 5.29.

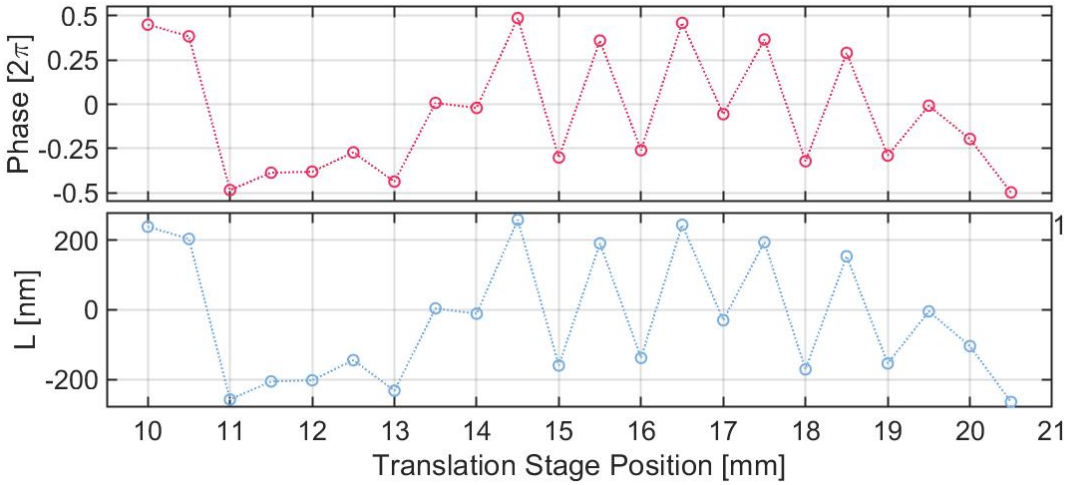

Figure 5.28: *Overview of phase and path difference measurements for different beam separations.* ***top:*** *Phase in terms of 2π as a function of the translation stage position.* ***bottom:*** *Path length difference calculated from the phase measurement above.*

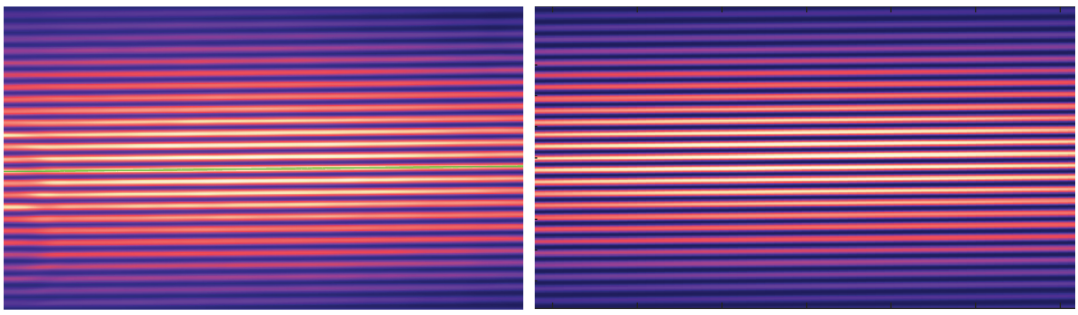

Figure 5.29: *Measured accordion vs simulated accordion.* ***left:*** *Measured accordion for a* 19.33 mm *beam separation, 0.0124(6) rad inclination and phase* $0.45 \times 2\pi$. ***right:*** *Simulation for* 19.33 mm *beam separation, replicating the experimentally observed tilt and phase.*

In general, we expect that the implementation of a piezo ring behind the back-mirror will allow for precise control of the path's difference, and therefore for a significant reduction of the phase difference. Additionally, measurements of the phase in time will provide more information about the stability of the accordion. Temperature fluctuations and mechanical noise caused by the piezo and the linear stage during the compression of the lattice will have to be considered for such measurements.

Contrast

The last property of each interference pattern that was analyzed was the contrast. We define the contrast as

$$Contrast = \frac{A_{max} - A_{min}}{A_{max}}. \tag{5.4}$$

where A_{max} is the amplitude of the fitted Gaussian packet defined by the max-

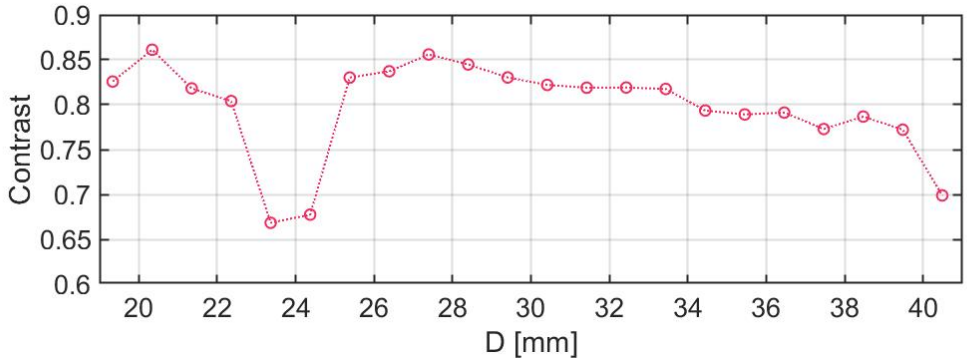

Figure 5.30: *Contrast for different beam separation.*

ima of the fringes. Similarly, A_{min} results from the amplitude of a Gaussian curve fitted on the minima of the pattern. The contrast is calculated for all beam separations D and the results are plotted in figure 5.30.

The causes of contrast loss are broad and varied. On the one hand, when the beams are not overlapping perfectly we observe a decrease in the maximal intensity of the middle fringe, while the values of the minima seem to increase. Figure 5.31 demonstrates the change of the intensity profile along z for the case of ideal overlapping and for a slight shift of the beams' positions with respect to each other.

On the other hand, power imbalance between the beams can strongly affect the final contrast. Figure 5.32 depicts the contrast loss caused by a power ratio $P_\theta : P_{-\theta} = 2 : 1$. In this case, the shift of the minima follows a Gaussian curve instead of two individual peaks, as in the case before.

Additionally, contrast loss can be expected due to the phase- and polarization discrepancies between the beams. Once the control mechanisms for the phase and the polarization are in place, their effect on the pattern contrast can

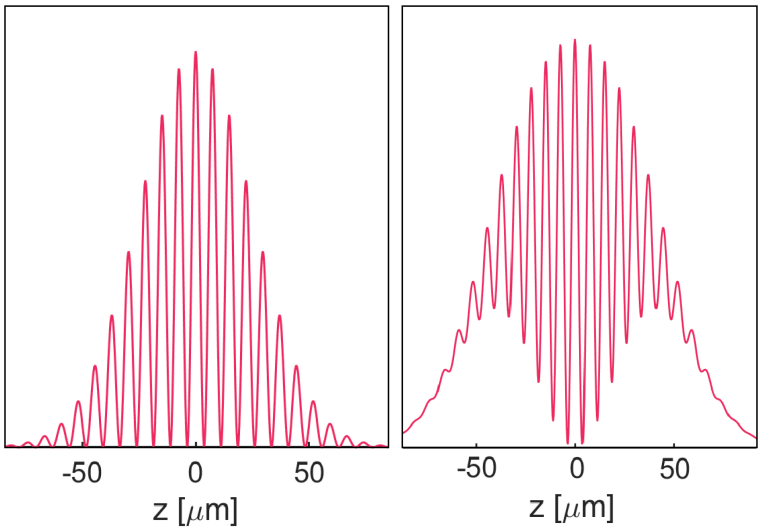

Figure 5.31: *Simulation of contrast loss of the interference pattern caused by imperfect overlapping of the beams.*

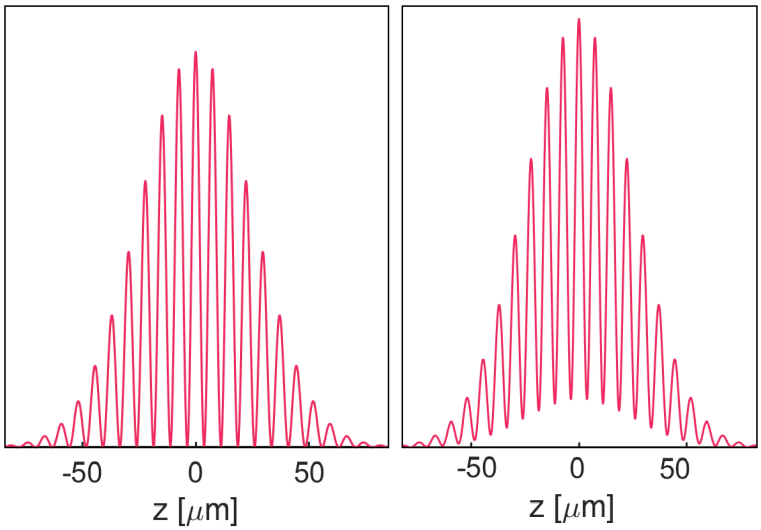

Figure 5.32: *Simulation of contrast loss of the interference pattern caused by power imbalance of the incoming beams.*

be tested in detail.

Chapter 6

Summary and Outlook

The main goal of this thesis has been to follow the design process of an accordion lattice for the bosonic isotope ^{164}Dy from the conceptual considerations up to the experimental characterization of a first test setup. First of all, we consider the interest in the new phenomena exhibited by ultracold dipolar quantum gases, especially their behavior in 2 dimensions described by the BKT transition. Initially, a numerical simulation of the interference pattern has yielded the necessary laser wavelength, power, and beam geometry to realize an optical accordion that confines dysprosium atoms tightly enough to enter the 2D regime. Assuming an atom cloud at 50 nK, we aim to achieve a trapping frequency along gravity of at least 15 kHz that fulfills the 2D trapping condition. According to calculations, for a maximal interference angle $\theta = 8.9°$, which is limited by the dimensions of the science chamber, and a laser with $\lambda = 532$nm, $P = 10$W, $w_y = 250$µm and $w_z = 50$µm, a maximal trapping frequency $\nu_z = 25$kHz can be reached. The chosen beam geometry produces a nearly-symmetrical trapping geometry in the residual plane, which is of interest for our future experimental applications. Furthermore, at a minimal half-angle $\theta = 0.76°$ a maximal fringe size $d = 20$µm, which is comparable to the atomic cloud's dimension, will allow for efficient loading of a single fringe from the crossed optical dipole trap.

Motivated by the large range of applications of accordion lattices for ultracold quantum gases that have proceeded this work, we have aimed to optimize the performance of the optical- as well as of the opto-mechanical design for our setup. Accordingly, many optical elements have been custom ordered, including a high-quality aspherical lens, and high-quality custom-sized polarizing beam splitters, right-angle mirrors, and wave plates. The engineering solutions to implement the customized optics guaranteeing stability and practicality have led to the design of a robust vertical structure called the tower mount.

For the first part of the test measurements, we have characterized the beam shaping and the general observation of an accordion lattice. During the test measurements we have noticed the sensitivity of the lattice's stability and performance to the proper alignment of the optics, especially of the aspherical lens. We propose three different methods for the alignment procedure that are expected to yield best results.

After the alignment, we have probed the realization of the minimal and maximal beam separation. Unfortunately, due to the use of test elements that differ from the custom ones, the minimal beam separation achieved is 19.33 mm, which represents an interference angle $\theta = 3.96^\circ$ and a fringe size $d = 3.85\mu$m. The instability of the accordion after the alignment procedures has been characterized by analyzing the vertical and horizontal displacement of the individual beams at the estimated focus. The shift in both directions is in the order of a couple of micrometers ($\approx 20\mu$m), indicating the need to refine the alignment in the future. The instability observed for the individual measurements is reflected in the test measurements of the fringe pattern, especially of the interference point of the beams. Altogether, we have been able to quantify and trace back different effects, such as the inclination of the accordion lattice, the shift of the middle fringe, and the loss of contrast. Overall, we conclude that a more detailed alignment procedure will significantly reduce these effects. In the near future, we expect to implement two tools that will help further stabilize the accordion: a piezo ring attached to the back mirror to control the phase, and two additional half-wave plates after the tower mount to correct the polarization. Additionally, once the custom lens arrives, its performance can be probed. Due to the simulated wavefront error of our lens in comparison to the wavefront error of the test lens, we expect a smaller shift of the beams' interference point for different beam separations, as we assumed that the main factor of the large shift, besides the alignment, is the spherical aberration.

Soon the mechanism for the compression, meaning a motorized linear stage, will be implemented as well. Once the motorized compression has been characterized and the accordion's setup refined, we will be able to mount everything in the main setup and apply the trap to the atoms. From there, the possibilities are endless...

List of Tables

List of Figures

Nomenclature

ϵ_0	Electric constant	$8.854\,187\,817 \times 10^{-12}\,\mathrm{F\,m^{-1}}$
μ_B	Bohr magneton	$5.788\,381\,801\,2(26) \times 10^{-5}\,\mathrm{eV\,T^{-1}}$
c	Speed of light in a vacuum inertial system	$299\,792\,458\,\mathrm{m\,s^{-1}}$
h	Planck Constant	$4.135\,667\,662(25) \times 10^{-15}\,\mathrm{eV\,s}$

Bibliography

[1] M. Lewenstein, A. Sanpera, V. Ahufinger, B. Damski, A. Sen(De), and U. Sen, "Ultracold atomic gases in optical lattices: mimicking condensed matter physics and beyond," *Advances in Physics*, vol. 56, no. 2, pp. 243–379, 2007.

[2] I. Bloch, J. Dalibard, and W. Zwerger, "Many-body physics with ultracold gases," *Rev. Mod. Phys.*, vol. 80, pp. 885–964, Jul 2008.

[3] A. L. Fetter and C. J. Foot, "Bose gas: Theory and experiment," 2012.

[4] C. Chin, R. Grimm, P. Julienne, and E. Tiesinga, "Feshbach resonances in ultracold gases," *Reviews of Modern Physics*, vol. 82, pp. 1225–1286, apr 2010.

[5] Y. Tang, A. Sykes, N. Q. Burdick, J. L. Bohn, and B. L. Lev *Physical Review A*, vol. 92, aug 2015.

[6] L. Chomaz, I. Ferrier-Barbut, F. Ferlaino, B. Laburthe-Tolra, B. L. Lev, and T. Pfau, "Dipolar physics: a review of experiments with magnetic quantum gases," *Reports on Progress in Physics*, vol. 86, p. 026401, dec 2022.

[7] T. Maier, H. Kadau, M. Schmitt, M. Wenzel, I. Ferrier-Barbut, T. Pfau, A. Frisch, S. Baier, K. Aikawa, L. Chomaz, M. J. Mark, F. Ferlaino, C. Makrides, E. Tiesinga, A. Petrov, and S. Kotochigova, "Emergence of chaotic scattering in ultracold er and dy," *Phys. Rev. X*, vol. 5, p. 041029, Nov 2015.

[8] G. Durastante, C. Politi, M. Sohmen, P. Ilzhöfer, M. J. Mark, M. A. Norcia, and F. Ferlaino, "Feshbach resonances in an erbium-dysprosium dipolar mixture," *Physical Review A*, vol. 102, sep 2020.

[9] T. Maier, I. Ferrier-Barbut, H. Kadau, M. Schmitt, M. Wenzel, C. Wink, T. Pfau, K. Jachymski, and P. S. Julienne, "Broad universal feshbach res-

onances in the chaotic spectrum of dysprosium atoms," *Physical Review A*, vol. 92, dec 2015.

[10] E. Britannica, "Dysprosium."

[11] Z. Hadzibabic, P. Krüger, M. Cheneau, S. P. Rath, and J. Dalibard, "The trapped two-dimensional bose gas: from bose–einstein condensation to berezinskii–kosterlitz–thouless physics," *New Journal of Physics*, vol. 10, p. 045006, apr 2008.

[12] C. Gölzhäuser, "Building a new dy quantum gas experiment," 2021.

[13] J. Gao, "A first two-dimensional magneto-optical trap for dysprosium," 2022.

[14] J. Schöner, "Magnetic-field setup for magneto-optical-trapping and interaction-tunin in novel dysprosium quantum gas experiment," 2022.

[15] L. Hoenen, "Fast, high precision low noise bipolar power supply for magnetic field coils in ultra-cold dysprosium experiment," 2022.

[16] P. Holzenkamp, "An optical dipole trap with tunable geometry for dysprosium," 2022.

[17] R. Grimm, M. Weidemüller, and Y. B. Ovchinnikov, "Optical dipole traps for neutral atoms," 1999.

[18] Li, Wyart, Dulieu, Nascimbene, and Lepers, "Optical trapping of ultracold dysprosium atoms: transition probabilities, dynamic dipole polarizabilities and van der waals c6 coefficients," *J. Phys. B*, vol. 50, p. 50, 2017.

[19] H. Li, J.-F. m. c. Wyart, O. Dulieu, and M. Lepers, "Anisotropic optical trapping as a manifestation of the complex electronic structure of ultracold lanthanide atoms: The example of holmium," *Phys. Rev. A*, vol. 95, p. 062508, Jun 2017.

[20] T. C. Li, H. Kelkar, D. Medellin, and M. G. Raizen, "Real-time control of the periodicity of a standing wave: an optical accordion," *Opt. Express*, vol. 16, pp. 5465–5470, Apr 2008.

[21] D. Mitra, P. T. Brown, P. Schauß, S. S. Kondov, and W. S. Bakr, "Phase separation and pair condensation in a spin-imbalanced 2d fermi gas," *Phys. Rev. Lett.*, vol. 117, p. 093601, Aug 2016.

[22] R. Saint-Jalm, *Development of a dynamically tunable,bidimensionally confining optical trap for ultracoldrubidium atoms*. PhD thesis, Université Paris sciences et lettres, 2015.

[23] A. Hebert, *A dipolar quantum gas microscope*. PhD thesis, Harvard, 2021.

[24] A. Kerkmann, *A novel Apparatus for Quantum Gas Microscopy of Lithium Atoms*. PhD thesis, Harvard, 2021.

[25] R.-J. Petzold, "Few ultracold fermions in a two-dimensional trap," 2020.

[26] R. A. Williams, J. D. Pillet, S. Al-Assam, B. Fletcher, M. Shotter, and C. J. Foot, "Dynamic optical lattices: two-dimensional rotating and accordion lattices for ultracold atoms," *Opt. Express*, vol. 16, pp. 16977–16983, Oct 2008.

[27] S. Brandstetter, "Towards the creation of vorticesin a dipolar bose-einsteincondensate," 2020.

[28] E. Magnan, J. Maslek, C. Bracamontes, A. Restelli, T. Boulier, and J. V. Porto, "A low-steering piezo-driven mirror," *Review of Scientific Instruments*, vol. 89, p. 073110, jul 2018.

Erklärung

Ich versichere, dass ich diese Arbeit selbstständig verfasst habe und keine anderen als die angegebenen Quellen und Hilfsmittel benutzt habe.

Heidelberg, den 1. März 2023

Valentina Salazar Silva